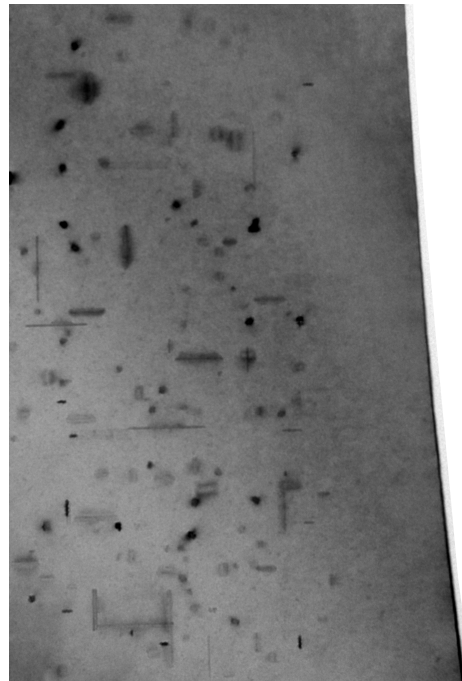Håkon Longva Korsvold

Investigating the precipitates in the heat affected zone of a HYB welded Al-Mg-Si-Cu alloy using transmission electron microscopy

Master's thesis in Nanoteknologi
Supervisor: Randi Holmestad
Co-supervisor: Jørgen A. Sørhaug
June 2023

NTNU
Norwegian University of
Science and Technology

Håkon Longva Korsvold

Investigating the precipitates in the heat affected zone of a HYB welded Al-Mg-Si-Cu alloy using transmission electron microscopy

NTNU
Norwegian University of
Science and Technology

ABSTRACT

The ongoing climate change due to man-made emissions necessitates the development of more energy efficient solutions across all aspects of society. One of the main sources of emissions is transportation, which necessitates the development of more energy efficient vehicles. One method of increasing a vehicles energy efficiency is to reduce its weight, as such there is great interest in developing ways to use more light materials like aluminium. This requires good methods to joining aluminium whit other metals. Traditional joining methods like fusion welding does however greatly impact the mechanical properties of aluminium, especially the heat-treatable alloy series 2xxx, 6xxx and 7xxx. These alloys gain their strength from a large number of precipitate particles embedded in the aluminium matrix, which may dissolve or undergo phase transition when subjected to high temperatures. As such efforts to develop solid state welding techniques that operate at lower temperatures have been made, one such technique is the hybrid metal extrusion and bonding (HYB) technique developed at NTNU and patented by Hybond.

Most solid state technique still results in high temperatures, which creates heat affected zones (HAZ) with reduced mechanical properties. In this thesis the HAZ on the advancing side of a HYB-weld between two similar Al-Mg-Si-Cu plates was studied. Cu additions to Al-Mg-Si alloys have been found to cause a change in the precipitate phases that form in the matrix. One of these phases, the L-phase, has in previous studies been linked to an increase in thermal stability.

The HAZ was studied with transmission electron microscopy (TEM) and scanning precession electron diffraction (SPED). The results of these studies were then discussed in relation to provided hardness measurements and a temperature simulation. Electropolished TEM samples were extracted from regions in the HAZ corresponding to 1, 2, 3 and 4 mm distance from the extrusion zone(EZ)//HAZ interface, in addition to a reference region from the base material.

Through TEM imaging it was found that the base material contained a large number of small precipitates, with an average length of around 6 nm. Samples extracted from the HAZ showed a decrease in density of precipitates, with the reduction in precipitates being greatest in regions close to the EZ/HAZ interface, at 1 mm distance very few precipitates were observed. The length of the precipitates increased in regions closer to the EZ/HAZ interface.

Through SPED it was found that the primary phase present in the base material was β'', with a smaller amount of L-phase being present. At regions closer to the EZ/HAZ interface it was found that partial phase transitions to β' and Q' phases had occurred, furthermore it was found that the L-phase to a greater

extent than β'' survived the temperature increase during welding.

The main cause of loss of hardness was found to be dissolution of β'' precipitates, driven by an increase in surface concentration at these precipitates and an increase in the diffusion constant of Mg and Si solutes in regions close to the EZ/HAZ interface.

SAMMENDRAG

Klimaendringer grunnet menneskeskapte klimagassutslipp har gjort det nødvendig å utvikle mer energieffektive løsninger i alle deler av sammfunnet. En av de største utslippskildene er transport av mennesker og varer, som gjør det nødvendig å utvikle mer energieffektive biler, skip, fly og lastebiler. En måte å gjøre dette på er å redusere vekten på transportmidlene, som et resultat av dette er det interesse for å utvikle metoder for å erstatte tradisjonelle metaller som stål med lettere alternativer som aluminium. Til dette trengs det metoder for sveise sammen ulike metaller på en god måte. Tradisjonell smeltesveising fører derimot til et stort tap av mekaniske egenskaper i aluminium, spesielt de varmeherdede legeringene i 2xxx, 6xxx og 7xxx seriene. Disse legeringene får mye av styrken sin fra et stort antall av nanopartikler, kalt presipitater, som dannes inne i aluminiumskrystallstrukturen. Disse presipitatene kan oppløses eller gå igjennom fasetransformasjoner dersom de utsettes for høy varme. Det er derfor ønskelig å utvikle gode faststoff-sveiseteknikker som kan operere på en lavere temperatur. En slik teknikk er hybrid ekstrusjon og binding (HYB), en teknikk utviklet på NTNU og patentert av Hybond.

De fleste faststoff-sveiseteknikker fører likevel til at høye temperaturer utvikles, som skaper varmepåvirkede soner (HAZ) med svekkede mekaniske egenskaper. I denne oppgaven har den varmepåvirkede sonen på en side av en HYB-sveis mellom to like plater av en Al-Mg-Si-Cu legering blitt undersøkt. Tilsetting av Cu i Al-Mg-Si legeringer har tidligere blitt vist at fører til en endring i presipitatfasene som dannes. En av disse fasene, L-fasen, har i tidligere studier blitt knyttet til en økning i termisk stabilitet.

Den varmepåvirkede sonen ble undersøkt med transmisjons elektronmikroskopi (TEM) og sveipe presesjon-elektrondiffraksjon (SPED). Resultatet av disse undersøkelsene ble diskutert i forhold til gitte hardhetsmålinger og temperatur simuleringer. Elektropolerte TEM prøver ble hentet ut fra regioner i HAZ som tilsvarte avstander på 1, 2, 3 og 4 mm fra grenseflaten mellom ekstrusjonssonen (EZ) og HAZ. Referanseprøver fra basematerialet ble også laget.

Gjennom TEM avbilding ble det funnet ut at basematerialet inneholdt et stort antall av små presipitater med en gjennomsnittelig lengde på rundt 6 nm. Prøver fra HAZ viste at tettheten av presipitater sank seg betraktelig i regioner nærme EZ/HAZ grenseflaten. Ved 1 mm distanse ble det observert svært få presipitater. Gjennomsnittelig lengde på presipitatene økte in regioner nærme EZ/HAZ grenseflaten.

Gjennom SPED ble det funnet ut at den presipitatene i basematerialet primært var av β'' fasen, med et mindre antall av L-fase presipitater. I regioner nærmere

EZ/HAZble det observert tegn på delvise fasetransformasjoner til β' og Q' presipitater. Det ble også observert at L-fasen i større grad enn β'' overlevde temperaturøkningen fra sveisingen.

Hovedmekansimen bak tapet av hardhet ble funnet til å være oppløsning av β'' presipitater, drevet av en sterk økning av overflatekonsentrasjon på disse presipitatene og en kraftig økning av diffusjonskonstanten til oppløst Mg og Si i regioner nærme EZ/HAZ grenseflaten.

PREFACE

This thesis presents the work of conducted during my final year of the five year nanotechnolgy engineering program at NTNU. The work was conducted at the department of physics, at the TEM Gemini centre, and as a part of the IN-SANE project.

ACKNOWLEDGEMENTS

CONTENTS

ABBREVIATIONS

List of all abbreviations:

- **TEM** Transmission electron microscopy

- **HYB** Hybrid metal extrusion and bonding

- **HAZ** Heat affected zone

- **CBED** Convergent beam electron diffraction

- **SAED** Selected area electron diffraction

- **BF** Bright field

- **DF** Dark field

- **SPED** Scanning precession electron diffraction

- **AS** Advancing side

- **RS** Retreating side

- **NMF** Non-negative matrix factorisation

- **EZ** Extrusion zone

- **RPM** Rounds per minute

- **FSW** Friction stir welding

- **GMA** Gas metal arc

- **TIG** Tungsten inert gas

INTRODUCTION

Climate change due to greenhouse gas emissions is one of the main challenges of our time, and solutions to reduce emissions is therefore an important topic across many scientific field. Transportation related emissions account for almost 25% of the worlds total greenhouse gas emissions, which needs to be reduced drastically if the world is to reach net zero emissions by 2050. Reducing the weight of vehicles and airplanes would cause them to be more energy efficient, and therefore lower their greenhouse impact. As such there are ongoing efforts to replace traditional metals like steel with lighter metals. Since it is often not possible to replace all part of a vehicle with lighter metals, there is also a need to develop methods in which light metals can be used in conjunction with traditional metals. To achieve this it is necessary to develop good techniques of joining different metals together.

One metal that is often used in lightweight applications is aluminium, which when alloyed with other elements has an excellent strength to weight ratio. The 2xxx, 6xxx and 7xxx series of aluminium alloys contain the strongest alloys of aluminium that are known, and owe their high strength to an age hardening process. During age hardening the metal is held at an elevated temperature, usually in the range 150-200°C, until peak strength is achieved. Age hardening causes a large amount of small evenly distributed metastable particles, referred to as precipitates, to form within the aluminium matrix. The mechanical properties of the alloy will be influenced by the density and size of these precipitates, as well as their crystal structure and chemical composition, referred to as phase. Any additional heat treatment after peak strength is reached will cause further changes in the microstructure, and the alloy will lose some of its strength.

Due to this temperature sensitivity of high strength alloys any exposure to high temperatures are usually to be avoided if possible. This makes the process of joining aluminium to other metals complicated, as traditional fusion welding techniques causes the temperature in the alloy to rise significantly, and results in a loss of strength in the joint and the area surrounding it.

This has resulted in efforts to develop solid-state welding techniques that allows for bonding of aluminium without raising the temperature to the melting point. One such technique is hybrid metal extrusion and bonding (HYB), developed and patented by Hybond, which utilizes the extrusion of an aluminium filler wire into a grove between the metal pieces to achieve a bond. The technique can be used to create Al-Al joints, in addition to joining aluminium with other metals such as

steel and copper. The mechanical work preformed during extrusion still generates a lot of heat and raises the temperature significantly, resulting in heat affected zones (HAZ) close to the weld, with reduced hardness and strength.

The addition of Cu to the 6xxx series of Al-Mg-Si alloys leads to the L-phase precipitate to be present in the aluminium matrix [1]. This phase has been linked to a high thermal stability [2], and may as such have higher stability during HYB-welding compared to other phases.

In order to better understand how the heat output from HYB-welding affects the mechanical properties, it is necessary to understand the changes that occur in the aluminium microstructure during bonding. Transmission electron microscopy (TEM) is a powerful tool that can be utilized to characterize materials down to the nano- and atomic-scale through imaging and diffraction experiments [3, 4]. In this master thesis the HAZ on the ascending side of a HYB-joint between two plates of a Al-Mg-Si-Cu alloy will be inspected using TEM. Conventional bright field and dark field TEM will be used to image the precipitate microstructure, in order to get a quantitative basis for the changes in the microstructure through the HAZ. Additionally scanning precession electron diffraction (SPED) will be used to determine the phases present at different regions in the HAZ.

THEORY

This chapter covers the theoretical background for the work presented in this thesis

2.1 Crystallography

A material is considered crystalline if its structure consists of a continuous and highly ordered sequence of identical building blocks, or unit cells as they are commonly called. In mathematical terms we can say that two points $\vec{r_i}$ and $\vec{r_j}$ in an infinitely large and perfect crystal will look identical for all integer combinations of hkl if [5]:

$$\vec{r_j} = \vec{r_i} + h\vec{a} + k\vec{b} + l\vec{c} \tag{2.1}$$

where $\vec{a}$, $\vec{b}$ and $\vec{c}$ are lattice vectors defined by the unit cell parameters. Variations in the relative length between a, b and c, and the angles between them α, β and γ, give rise to 7 unique crystal systems that can be infinitely stacked[6]. Additionally each unit cell may have more than lattice point within itself, which increases the different types of cells that are possible. All unit cells have a lattice point at the (0, 0, 0), if this is the only lattice point the lattice is said to be primitive (P), body centered lattices (I) have an additional lattice point located at (1/2, 1/2, 1/2). Base centered lattices (C) have an additional point at either (1/2 ,1/2 ,0), (1/2, 0, 1/2) or (0, 1/2, 1/2), while face centered lattices have lattice points at all three locations. Accounting for the different lattice systems possible for each crystal system yields a total of 14 different Bravais lattices that are possible[6]. An overview of the different crystal systems and their possible Bravais lattices are given in Table 2.1.

Directions and planes within a crystal structure are commonly defined in relation to its lattice vectors. A direction is denoted with square brackets $[h\,k\,l]$, where hkl are integers describing a linear combination of the lattice vectors $\vec{a}$, $\vec{b}$ and $\vec{c}$. Due to symmetry there are often several equivalent directions within a crystal, a set of equivalent directions are denoted $\langle h\,k\,l \rangle$. Planes denoted $(h\,k\,l)$ are defined by the reciprocal of their intersection with the lattice vectors, such that a plane $(h\,k\,l)$ will intersect at $\frac{\vec{a}}{h}$, $\frac{\vec{b}}{k}$ and $\frac{\vec{c}}{l}$, a set of equivalent planes are denoted $\{h\,k\,l\}$. For cubic systems the direction $[h\,k\,l]$ is always perpendicular to the plane $(h\,k\,l)$, but this is not true for any other crystal system. This will be useful later as it

Table 2.1: Overview of the different crystal systems along with their defining geometry and their possible cell types which toghether form the 14 Bravais possible lattices. [6]

Crystal System	Cell type	Unit cell parameters
Triclinic	P	$a \neq b \neq c$ $\alpha \neq \beta \neq \gamma$
Monoclinic	P, C	$a \neq b \neq c$ $\alpha = \beta \neq \gamma$
Orthorombic	P, I, F, C	$a \neq b \neq c$ $\alpha = \beta = \gamma = 90°$
Tetragonal	P, I	$a = b \neq c$ $\alpha = \beta = \gamma = 90°$
Cubic	P, I, F	$a = b = c$ $\alpha = \beta = \gamma = 90°$
Trigonal	P	$a = b = c$ $\alpha = \beta = \gamma < 120°, \neq 90°$
Hexagonal	P	$a = b \neq c$ $\alpha = \beta = 90°$ $\gamma = 120°$

allows for imaging of in-axis and in-plane features of the same region from a single angle.

When doing diffraction experiments, the result will depend on the Fourier space associated with a given lattice, as such it is beneficial to define the reciprocal lattice $\mathbf{G}$ that defines this space, which can be found by [5]:

$$\mathbf{b_1} = 2\pi \frac{\mathbf{a_2} \times \mathbf{a_3}}{\mathbf{a_1} * \mathbf{a_2} \times \mathbf{a_3}}; \mathbf{b_2} = 2\pi \frac{\mathbf{a_3} \times \mathbf{a_1}}{\mathbf{a_1} * \mathbf{a_2} \times \mathbf{a_3}}; \mathbf{b_3} = 2\pi \frac{\mathbf{a_1} \times \mathbf{a_2}}{\mathbf{a_1} * \mathbf{a_2} \times \mathbf{a_3}} \quad (2.2)$$

where $\mathbf{a_1}, \mathbf{a_2}, \mathbf{a_3}$ are the primitive vectors of the crystal lattice, i.e the smallest possible vectors that describe the lattice, and $\mathbf{G} = u\mathbf{b_1} + v\mathbf{b_1} + w\mathbf{b_1}$ provides a basis for the Fourier space.

In reality crystals are not 100% perfect, but have defects such as vacancies and dislocations. These imperfections are essential for the formation of precipitate phases, as they allow easier movement and clustering of solutes within the lattice through diffusion. The equilibrium number fraction of vacancies in a crystal(N_v/N) is given by [7]:

$$\frac{N_v}{N} = e^{\frac{-\Delta G_v}{(k_b T)}} \quad (2.3)$$

where ΔG_v is the energy required to create a vacancy in a given crystal, k_b is the Boltzmann constant and T the absolute temperature.
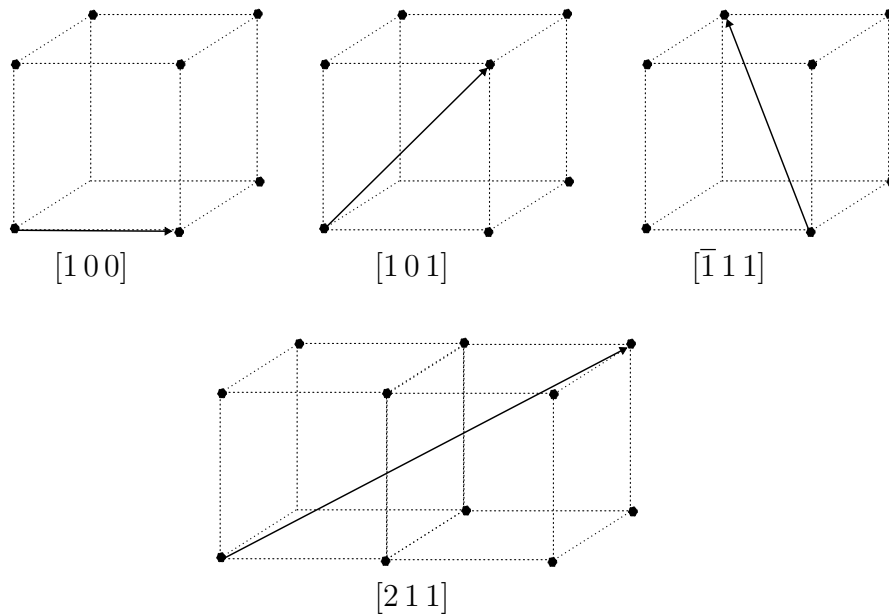
Figure 2.1: Selected crystallographic directions shown in a cubic lattice system
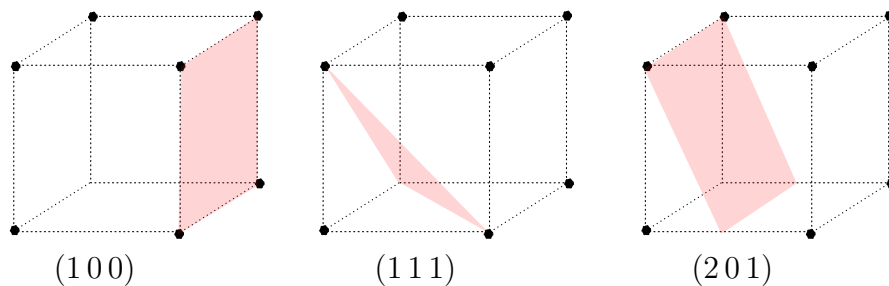

Figure 2.2: Illustration of selected crystal planes in a cubic crystal system.

2.2 Aluminium

Aluminium is a versatile material that has a broad range of applications. As a structural material it is the second most commonly used metal after steel. While chemically pure aluminium is a relatively soft material, with a yield strength < 50 MPa, aluminium alloyed with a small amount of other elements can have a yield strength many times higher than this, with yield strengths above 500 MPa being possible for the strongest alloys. High strength steels can achieve yield strengths significantly higher than this. Aluminium does however have an advantage in weight, with a specific weight of just 2.7 kg/dm^3, compared to around 7.9 kg/dm^3 for steel [8]. Aluminium is therefore used in many applications where weight is an important factor. Aerospace, automotive and maritime industries are among the examples where light weight materials are are important [9]. Table 2.2 shows an overview of the different alloy classifications, along with some of its common applications.

The 6xxx series of aluminium alloys covers the wrought aluminium alloys where Mg and Si are the principal alloying elements. In general these alloys exhibit good formability, corrosion resistance and medium strength [9]. The proportion between Mg and Si is such that metastable particles of magnesium and silicon can be formed, which is why Mg and Si behave differently in 6xxx alloys compared

Table 2.2: An overview of the different alloy series of wrought aluminium, as designated by the Aluminium Association, and some of their most common applications [9].

Series	Alloying element	Applications
1xxx	none	Chemical industry and electrical applications
2xxx	Cu	Aerospace and other high strength applications
3xxx	Mn	Architectural applications and general purpose
4xxx	Si	Brazing sheets and welding rods
5xxx	Mg	Marine environments
6xxx	Mg, Si	extruded structures and automotive industry
7xxx	Zn	Aerospace and other high strength applications
8xxx	Miscellaneous	Miscellaneous

to 4xxx and 5xxx alloys. The most notable difference is that 6xxx alloys, unlike 4xxx and 5xxx, are heat treatable as the Mg-Si particles require ageing at elevated temperatures to precipitate out of the solid-solution into larger particles, these particles will henceforth be referred to as precipitates. The properties of alloys in this series will be dependent on the amount of Mg and Si added, as well as any other alloying elements and the heat treatment it is subjected to, as this will determine the nature of the precipitates that form. The conditions for forming a precipitate is similar to that of forming any particle in a medium, and is governed by [10]:

$$\Delta G_{total} = -V\Delta G_{bulk} + A_{surf}\gamma \tag{2.4}$$

where ΔG_{total} is the free energy associated with the formation of a given particle. A_{surf} is the surface area of the particle and γ is the interface energy between the particle and the surrounding medium. V is the volume occupied by the particle and ΔG is the volume free energy associated with expanding the volume of the particle, which generally can be expressed as [10]:

$$\Delta G_{bulk} = \Delta H - T\Delta S \tag{2.5}$$

Where ΔH is the change in enthalpy and ΔS is the change in entropy, which will always be negative. ΔG_{total} will therefore decrease with temperature, and allow for dissolution of the precipitates if the temperature is too high.

Dislocations in crystalline structures tend to occur along the slip systems of the crystal, i.e the planes adn directions with the least resistance to displacements of atoms. Defects in the matrix, such as solutes, precipitates and dislocations, tend to strengthen the material as they interrupt the perfectly ordered crystal planes, and create barriers that must be overcome for the propagation of dislocations. The misfit of a solute atom in the matrix creates a local stress on the matrix, which creates an additional force the dislocation must overcome [11]. When dislocations encounter a precipitate, there are two interactions that can occur. Either the dislocation shears through the precipitate, which usually happens with small precipitates that are coherent with the matrix. Or the dislocation bypasses the precipitate, which usually happens with larger and incoherent precipitates [12]. When a dislocation has propagated along a slip plane, the positions of the atoms

along the slip plane will deviate from the idealized crystal structure. This causes an obstacle for any other slip planes that crosses it, and as such the presence of dislocations hinders the formation of additional dislocations, this is usually referred to as work hardening. The strength contributions from the different defects are usually added linearly [13].

$$\sigma_y = \sigma_p + \sigma_{ss} + \sigma_{disl} + \sigma_i \tag{2.6}$$

where σ_p, σ_{ss} and σ_i are the tensile strength contributions from precipitate strengthening, solute solution strengthening and the intrinsic strength of aluminium. In age hardened alloys, the greatest contribution will be from σ_p.

Tensile strength measurements are not perfromed in this project, instead the change in mechanical properties are measured through the change in hardness. The conversion from tensile strength to hardness does not follow any general formula, as the relation between the measurements vary depending on the material. It is however possible to find empirical models that convert tensile strength to hardness for a given material system, for Al-Mg-Si alloys the conversion has been found to be [13]:

$$\sigma_y = \frac{HV - 16}{0.33} \tag{2.7}$$

where HV is the hardness measured in Vickers hardness, and σ_y is the tensile strength measured in MPa.

2.2.1 Heat treatment and thermal effects on structure in 6xxx alloys

Equation 2.3 shows that as temperature increases, the number of vacancies increases as well, additionally the stability of any precipitates will decrease as ΔG_{bulk} in Equation 2.4 decreases as T increases. This in turn increases the solubility of solutes in the matrix, as the solutes are able to diffuse into the newly vacant positions, since the additional thermal energy will make it more likely for an atom to overcome any energy-barrier associated with a displacement from site A to B. The rate of diffusion of solutes is governed by Fick's second law of diffusion, given by [14]:

$$\frac{\partial \phi}{\partial t} = D\nabla^2 \phi \tag{2.8}$$

where ϕ is the concentration of the solute and D is the diffusion constant for the solute within the medium. The temperature dependence on diffusion comes from a variation in D, which in many cases are found to follow the Arrhenius formula [15]

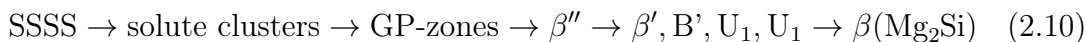$$D = D^0 \exp\left\{\frac{-\Delta H}{k_B T}\right\} \tag{2.9}$$

where D^0 is the pre-exponential factor and ΔH is the activation energy of diffusion.

If the temperature of the metal drops rapidly, which can be achieved by quenching, the number of vacancies are frozen in. The high number of vacancies allow

for diffusion of the solutes through the matrix, and inevitably these solutes will cluster together and nucleate into GP-zones. In order for nucleation to occur the energy barrier associated with creating an interface, as given by Equation 2.4, must be overcome. Mg_2Si has an antifluorite structure, which like the aluminium matrix is an fcc structure, with a unit cell length of $a = 6.37$Å[16] compared to $a = 4.04$Å for aluminium. The discrepancy between Mg_2Si and aluminium results in an incoherent interface in all directions [1], and subsequently a high value for γ. Due to this large γ Mg_2Si-precipitates are unstable for small sizes, in fact the high energy barrier for nucleation prevents any Mg_2Si particles from nucleating at all. Instead a series of meta-stable phases are formed, starting with the nucleation of small GP-zones, which are small particles embedded in the matrix, usually no more than a couple of unit-cells in size. When the alloy is subjected to heat treatment the GP-zones grow to complete precipitates of the β'' phase. This phases has a high coherency with aluminium along in the $\langle 1\,0\,0 \rangle$ direction [17], resulting in a low γ for the interface parallel to this direction. The low interface energy results in a growth that is heavily favored in this direction, and the precipitates take the shape of needles in the $\langle 1\,0\,0 \rangle$ directions of aluminium. In Al-Mg-Si alloys, all other precipitate phases are similarly oriented in these directions, as they develop from the β''-phase [18].
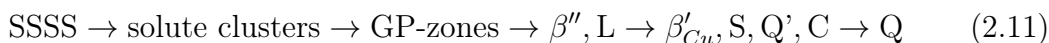
When heat-treatable aluminium alloys are subjected to high temperatures, the solubility of the solutes will again increase and the precipitates may dissolve. Alternatively, if the temperature is high, but not high enough to dissolve the existing precipitates, then the alloy will be subjected to artificial ageing where the conditions are favorable for further precipitate growth. After a certain amount of time, peak hardness is reached, this condition of the alloy is referred to as T6. Further heat treatment past the T6 condition will reduce the strength of the alloy, this is referred to as an overaged condition. In a study by Sunde et.al [19] it was shown how the precipitate structure in an Al-Mg-Si(-Cu) alloy, very similar to the alloy used in this project, evolve during in-situ heat treatment. Figure 2.3 is taken from [19] and shows bright field TEM images of the same area after exposed to high temperatures after different amounts of time.

The precipitate sequence for Al-Mg-Si system has been found to be [20][1]:

$$SSSS \rightarrow \text{solute clusters} \rightarrow \text{GP-zones} \rightarrow \beta'' \rightarrow \beta', \text{B'}, U_1, U_1 \rightarrow \beta(Mg_2Si) \quad (2.10)$$

Where especially the β'' phase contributes to strengthening of the alloy, due to its high coherency with the aluminium matrix. Table 2.3 shows an overview of the different phases in Al-Mg-Si alloys, along with any known coherency directions.

The addition of Cu to the system further complicates the precipitate sequence, which can be expressed as [22, 21]:

$$SSSS \rightarrow \text{solute clusters} \rightarrow \text{GP-zones} \rightarrow \beta'', \text{L} \rightarrow \beta'_{Cu}, \text{S}, \text{Q'}, \text{C} \rightarrow \text{Q} \quad (2.11)$$

The Cu containing phases all take the shape of needles or laths extending in the $\langle 1\,0\,0 \rangle$ aluminium direction due to coherency in this direction. Additionally they also have a common network of Si columns in a hexagonal network. With the different phases having different arrangements of Al, Mg and Cu columns between the Si columns [2, 23]. The L phase has been linked to good thermal stability [2].
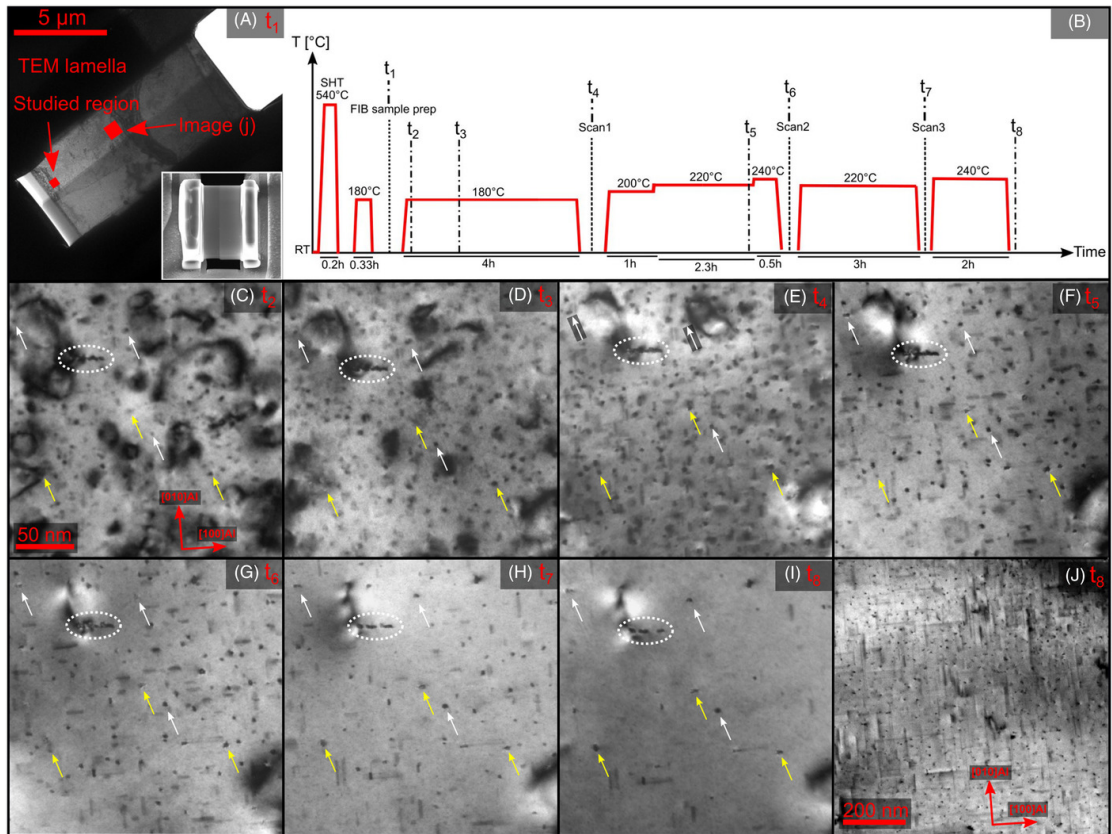
Figure 2.3: Evolution of precipitates in an Al-Mg-Si(-Cu) alloy when subjected to high temperatures, given by the heat profile in (B). (C-I) shows the precipitate structure at different stages of the temperature program, showing that the precipitates dissolve during heat treatment. The white and yellow arrows indicate L and β''/β'_{Cu}/Q phases that remained after heat treatment. Image acquired from [19]

For practical purposes it can be beneficial to define a maximum mechanical temperature (T_{MM}) for an alloy, above which significant changes in the mechanical properties of the material can be expected. This value is not an objective limit, but determined by the practical applications the material will be used in. T_{MM} will therefore vary depending on the timescale of high temperature, and by what is determined as an acceptable threshold for loss of mechanical properties. For alloys in the T6 condition, a decent estimate for T_{MM} is around the temperature artificial ageing is performed, as prolonged exposure to these temperatures are known to cause changes in the precipitate structure. A study by Maisonnette et. al. [24] investigated the effect of different short heat treatments had on a 6061-T6 alloy, some of the findings is presented in Figure 2.4. This study found that a short increase in T up to 200°Chad no noticeable effect on yield strength, while heating to temperatures above this resulteted in lowered yield strength. 200°Cis on the higher end of typical ageing temperatures for 6061 alloys, confirming that ageing temperature can give a decent estimate of T_{MM}. The study also showed that increasing time spent at high temperatures, controlled by the temperature rate, also decreased the yield strength.

Table 2.3: Known precipitate phases in Al-Mg-Si alloys and their coherent directions with the aluminium matrix. [21, 22]

Phase	Composition	Coherency with Al	Space group
β''	Mg_5Si_6	$\langle 0\,0\,1\rangle$, $\langle 2\,3\,0\rangle$, $\langle 1\,3\,0\rangle$	C2/m
β'	Mg_9Si_5	$\langle 0\,0\,1\rangle$, $\langle 1\,3\,0\rangle$	P6$_3$
U1	$MgAl_2Si_2$	$\langle 0\,0\,1\rangle$, $\langle 3\,\bar{1}\,0\rangle$	P-31m
U2	$Mg_2Al_2Si_2$	$\langle 0\,0\,1\rangle$, $\langle 1\,3\,0\rangle$	Pnma
B'	$Mg_9Al_3Si_7$	$\langle 0\,0\,1\rangle$, $\langle 1\,5\,0\rangle$	P-6
β	Mg_2Si	incoherent	Fm-3m

Table 2.4: Known precipitate phases in Al-Mg-Si-Cu alloys and their coherency with the aluminium matrix. [21, 22]

Phase	Composition	Coherency with Al	Space group
L	Varies	$\langle 1\,0\,0\rangle$	-
β'_{Cu}	$Al_3Mg_3Si_2Cu$	$\langle 0\,0\,1\rangle$, $\langle 1\,3\,0\rangle$	P-62m
S	varies	$\langle 0\,0\,1\rangle$, $\langle 3\,\bar{1}\,0\rangle$	-
Q'	$Al_xMg_{12-x}Si_7Cu_2$	$\langle 0\,0\,1\rangle$, $\langle 1\,5\,0\rangle$	P-6
C	$AlMg_4Si_3Cu$	$\langle 0\,0\,1\rangle$, $\langle 0\,1\,0\rangle$	P2$-$1
Q	$Al_xMg_{12-x}Si_7Cu_2$	incoherent	P-6

(a)   (b)
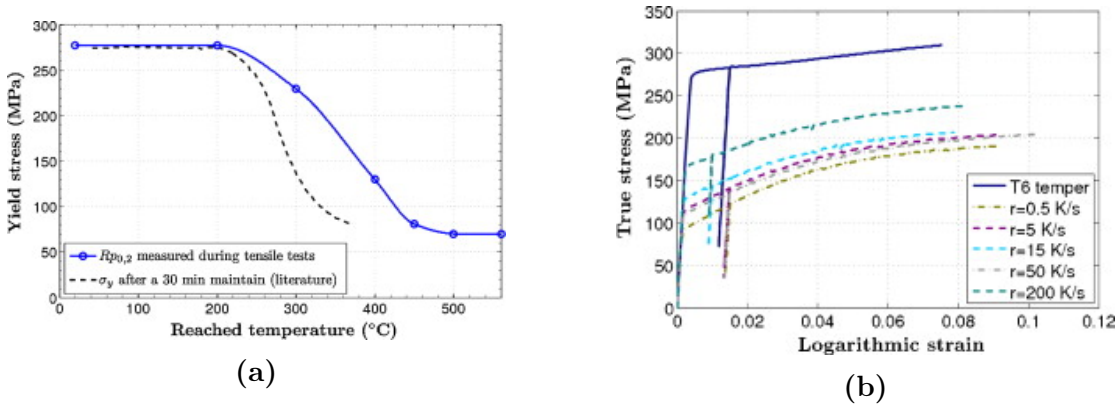
Figure 2.4: Plots taken from [24], showing the effect of different short heat treatments on 6061-T6 aluminium. All measurements were performed by applying a constant temperature increase until reaching the target temperature, and then allowing the sample to cool down. Plot (a) Shows yield strength based on max temperature reached by increasing at a constant rate of 15 K/s, the dotted line represents literature values of where target temperature is held for 30 minutes. Noticeable changes in yields strength only occurs above 200°C. Plot (b) Shows stress curves for samples heated to 400°C at different rates, which varies the time spent at high temperatures. The stress curves shows increasing strength for increased temperature rates when comparing 0.5 K/s, 5 K/s and 15 K/s. The 50 K/s and 200 K/s tests overshot and undershot the temperature target respectively, making them not comparable to the lower rates.

2.3 HYB-welding

As the properties of age-hardened aluminium alloys are dependent on what heat treatment is performed, heat exposure after age-hardening to T6 may have negative effects on the mechanical properties of the alloy. Prolonged exposure to temperatures above the artificial ageing temperature (150-200°C) are known to cause an over-aged state, while prolonged temperatures at even higher temperatures may cause dissolution of precipitates and returning the alloy to a state of solid solution. This temperature sensitivity makes welding of aluminium complicated compared to other metals, such as steel. In traditional fusion welding techniques the chemical bond is established in the molten phase, requiring temperatures above the melting point of the metal [25]. These techniques will naturally generate a lot of heat in the weld, which will propagate to the volumes adjacent to the fusion zone (FZ) and create heat affected zones (HAZ). In the HAZ, the elevated temperature allows for changes in the microstructure which will affect the mechanical properties of the metal. In steel it is possible to maintain a mechanical strength with fusion welding that is comparable to the base material if the process parameters are optimal [26]. In aluminium the HAZ will have a significant reduction in strength and hardness, especially in precipitate hardened alloys in the 2xxx, 6xxx and 7xxx series, as the temperature will approach the melting point in the most affected areas [27]. At these temperatures the precipitates may undergo phase transitions, growth and dissolution, essentially cancelling out the effect of age-hardening and typically causing a reduction in strength [27]. Figure 2.5 shows how a typical hardness profile may look through a fusion weld in aluminium. The reduced strength and wide HAZ associated with fusion welded aluminium have resulted in efforts to develop solid state welding techniques that operate at temperatures lower than the solidus temperate, such as cold pressure welding [28], friction stir welding (FSW) [25] and hybrid metal extrusion and bonding (HYB) [29].
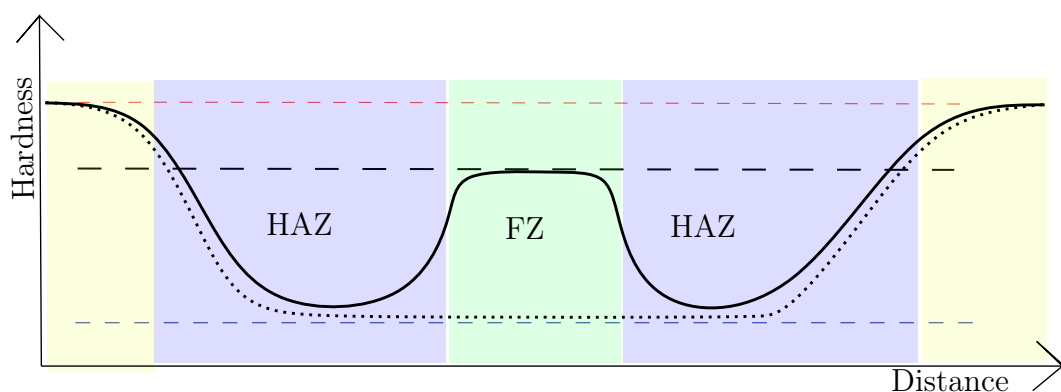

Figure 2.5: Illustration of a typical hardness profile of a fusion weld between aluminium. The dotted line represents hardness imediatly after welding, and the solid line after natural ageing. The hardness drops significantly in the HAZs next to the weld, as the microstructure reaches an overaged condition. The FZ will be in a SSSS state after welding, and will regain some of the hardness over time due to natural ageing. Post weld artificial ageing can restore some of the reduced strength in the HAZ, but is not always feasible.

In a study by Jannet et. al the effect on tensile strength of a AA6061-T6 and 5083-O weld using different welding techniques were investigated [30]. This study shows how fusion welding techniques, in this case Tungsten inert gas welding (TIG), results in a lower yield and tensile strength compared to solid-state techniques, in this case FSW. It was further shown that post weld artificial ageing can improve the mechanical properties of fusion welds, with the effect varying between the different fusion weld techniques. In this case post age strength of the strongest fusion weld was still slightly lower than that of non-aged FSW. The FSW also increased in strength with post weld ageing. The need for post weld ageing presents a major disadvantage for fusion welds, as this process can be time consuming and costly, as well as being impractical for certain applications. Techniques that do not require post weld treatment would therefore have more flexibility in its applications.

HYB is a solid state joining method that utilizes continuous extrusion of a aluminium filler material into a groove between two metal plates [29] to achieve a bond. A pinpoint extruder moves along the groove at a constant speed, with a rotating pin with dies extending into the groove. The filler wire is drawn into the inner extrusion chamber of the head by by the constant rotation of the rotating pin, where the wire will flow into the abutment blocking the extrusion chamber. The build up of pressure will force extrusion of the wire through the moving dies of the pin and into the groove. An illustration of the HYB pinpoint extruder is shown in Figure 2.6
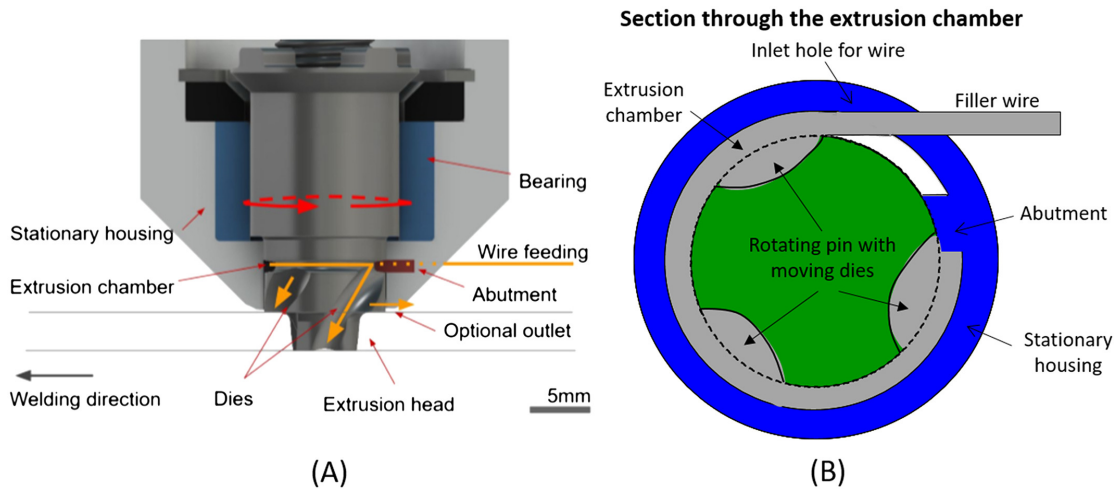

Figure 2.6: Overview of the HYB pinpoint extruder. Illustration from [29]

While high temperatures are not needed for the extrusion work that bonds the materials, the process generates a lot of frictional work, which will be converted into heat. The amount of power generated in the process will be dependent on the drive spindle torque (M_t) and the rotational speed (usually given in RPM) of the pin (N_s). The total power output of the extrusion process is given by [29]

$$W_t = \frac{2\pi}{60} M_t N_s \qquad (2.12)$$

To reduce the heat input to the metal, a CO_2 coolant is used, absorbing heat from the system at a rate W_c, and reducing the amount of heat that is transferred to the base material. The gross heat input to the metal then becomes [29]:
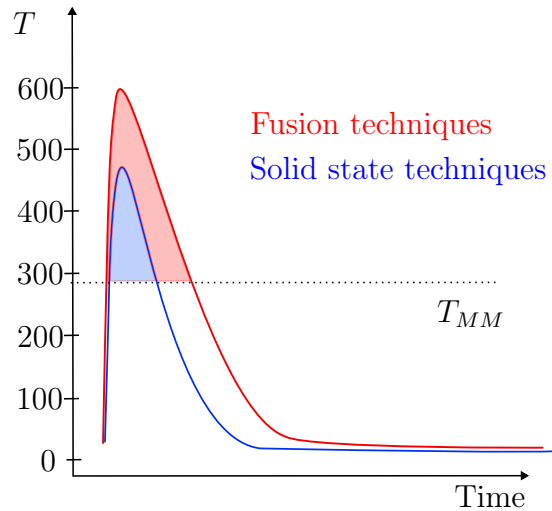
Figure 2.7: Schematic drawing of typical heat profiles for fusion and solid state welding techniques. The dotted line represents an estimate for T_{MM}, above which significant changes in microstructure and mechanical properties are expected to occur during the short time frame.

$$E = \frac{W_t - W_c}{1000v} \qquad (2.13)$$

where E is the heat input per mm of the weld measured in (kJ/mm), and v is the speed of the pinpoint extruder. While the heat generated by the process still causes a significant increase in temperature, the temperature is below what is seen in fusion welding techniques. Temperatures in the HAZ of fusion welds approach the melting temperature above 600°C, while the maximum temperature in solid state techniques can be in the range 300-500°C. With a reduction in temperature, the time spent above T_{MM} also decreases, further reducing the weakening in the HAZ. Typical temperature curves for fusion welds and solid state welds are shown in Figure 2.7.

The HYB-process creates an asymmetrical weld based on the rotation direction of the pin, with an advancing side (AS), where the movement of the pin is the same as the welding direction, and a retreating side (RS), where the movement of the pin opposes the welding direction. Typically the process results in the removal of the surface oxide layer on the base material on the AS, while the base material in the RS is deformed into the groove together with the filler wire. The heavily deformed region of mixed RS base material and filler wire is referred to as the extrusion zone (EZ). The changes in the HAZ is a result both thermal and mechanical processes on the RS, while the AS will primarily be affected by thermal effects. As such the advancing side will be studied to evaluate the changes caused by the increased temperature in the HAZ.

It has been shown that HYB-welded AA6082 alloys have comparable yield strength to FSW-welds of AA6082, and higher yield strength than welds performed by gas metal arc (GMA) [31]. Another study [32] showed that HYB-butt welds in AA6060 alloys showed improved fatigue properties compared to GMA welds and comparable properties to FSW and laser beam welding, and that improvements in the technique could yield superior fatigue properties.

2.4   Diffraction

The theory in this section is primarily taken from Williams and Carter [3], unless anything else is specified.

Diffraction is defined as the interaction between a wave and an object. This interaction will cause a change in the wave vector, the difference between the incoming and outgoing wave-vector is defined as the scattering vector $\Delta\mathbf{k}$. If a wave is elastically scattered by two parallel planes separated by a distance d, then the outgoing wave will be subjected to constructive interference if the Bragg condition

$$2d\sin(\theta) = n\lambda \tag{2.14}$$

is satisfied, where θ is the scattering angle, λ is the wavelength and n is an integer. For a crystal, d is given by the spacing between equivalent crystallographic planes, and for a plane $(h\,k\,l)$ in a cubic system is given by:

$$d_{hkl} = \frac{a}{\sqrt{h^2 + k^2 + l^2}} \tag{2.15}$$

n in Equation 2.14 is usually incorporated into hkl when describing diffraction between crystal planes. Equation 2.14 describes the condition for constructive interference between two planes, but in a crystal scattering happens at individual atoms in a lattice, not ideal planes. A wave scattered from a lattice ($\phi(\Delta\mathbf{k})$ can be calculated as[4].

$$\psi(\Delta\mathbf{k}) = \sum_{\mathbf{r_g}}\sum_{\mathbf{r_k}} f_{at}(\mathbf{r_g} + \mathbf{r_k})e^{-2\pi\Delta\mathbf{k}(\mathbf{r_g}+\mathbf{r_k})} \tag{2.16}$$

where $\mathbf{r_g}$ are the different lattice points, $\mathbf{r_k}$ are the atoms in the basis and $f_{at}(\mathbf{r_g} + \mathbf{r_k})$ is the scattering factor of the indicated atom. Since all unit cells have the same atoms, $f_{at}(\mathbf{r_g} + \mathbf{r_k})$ will not depend on $\mathbf{r_g}$ and Equation 2.16 can be expressed as:

$$\psi(\Delta\mathbf{k}) = \sum_{\mathbf{r_g}} e^{-2\pi\Delta\mathbf{kr_g}} \sum_{\mathbf{r_k}} f_{at}(\mathbf{r_k})e^{-2\pi\Delta\mathbf{kr_k}} \tag{2.17}$$

$$= \mathcal{S}(\Delta\mathbf{k})\mathcal{F}(\Delta\mathbf{k}) \tag{2.18}$$

Where $\mathcal{S}(\Delta\mathbf{k})$ is the shape factor defined by the crystal system and $\mathcal{F}(\Delta\mathbf{k})$ is the structure factor dependent on the basis, if the basis consists of a single atom then $\mathcal{F}(\Delta\mathbf{k}) = f_{at}$. For a crystal, diffraction occurs when the Laue condition is satisfied, which states that the diffraction vector $\Delta\mathbf{k}$ must be a vector in the reciprocal lattice[4].

$$\Delta\mathbf{k} = \mathbf{g} \tag{2.19}$$

where $\mathbf{g} = h\mathbf{a_1}* + k\mathbf{a_2}* + l\mathbf{a_3}*$, the reciprocal lattice of the crystal. If this condition is inserted into Equation 2.18 for a structure with mono-atomic basis, then $\mathcal{S}(\Delta\mathbf{k})$ must be non-zero for all values of hkl. Using this the diffraction condition for more complex structures can be found by first finding diffraction condition of a simpler structure with the same shape, and then expanding to

a multi-atomic basis and finding any further restrictions given by the structure factor

$$\mathcal{F}_{hkl} = \sum_i f_i e^{2\pi i(hx_i + ky_i + lz_i)} \tag{2.20}$$

where the contribution from every atom in the basis is summed together. The diffraction condition of an fcc structure can therefore be found by first finding the condition for that of a simple cubic structure, which is $\Delta \mathbf{k} = \mathbf{g} = h\mathbf{a_1}* + k\mathbf{a_2}* + l\mathbf{a_3}*$ for any integer combination hkl, and then finding the structure factor given by the 4 atoms at positions (0, 0, 0), (1/2, 1/2, 0), (1/2, 0, 1/2) and (0, 1/2, 1/2), which is:

$$\begin{aligned}\mathcal{F}_{fcc} &= f_{at}(1 + e^{\pi i(k+l)} + e^{\pi i(h+l)} + e^{\pi i(h+k)}) \\ &= \begin{cases} 4f_{at}, & \text{if } h, k, l \text{ all even or all odd.} \\ 0, & \text{otherwise} \end{cases}\end{aligned} \tag{2.21}$$

resulting in kinematic extinction of diffraction spots where hkl are not all even or all odd integers.

In this thesis, the diffraction patterns produced by precipitates within aluminium will be used to determine the phase of different precipitates. All diffraction patterns will be recorded in the $(1\,0\,0)$-direction of aluminium, and since the structure of the precipitates are coherent with the matrix it is possible to predict the diffraction patterns that will be observed. Figure 2.8 shows the all the expected diffraction patterns from the β'' phase, as calculated by Yang et. al [33].

The patterns from the post-β'' phases β' and Q' oriented along the zone axis are shown in Figure 2.9, similar patterns that arises due to symmetry in the aluminium matrix are not shown. Since the L-phase contains fragments of different phases with different space groups, it is not easy to calculate an expected diffraction pattern. However a recognisable pattern has been found using Fourier transformation of high resolution TEM images of the phase[34]. Figure 2.10 Shows the Fourier transform of an image of an L-precipitate, as well as a diffraction pattern captured using precession electron diffraction. The recognisable pattern stems from the hexagonal Si columns that are oriented along a secondary $\langle 1\,0\,0 \rangle$ direction in the aluminium matrix.
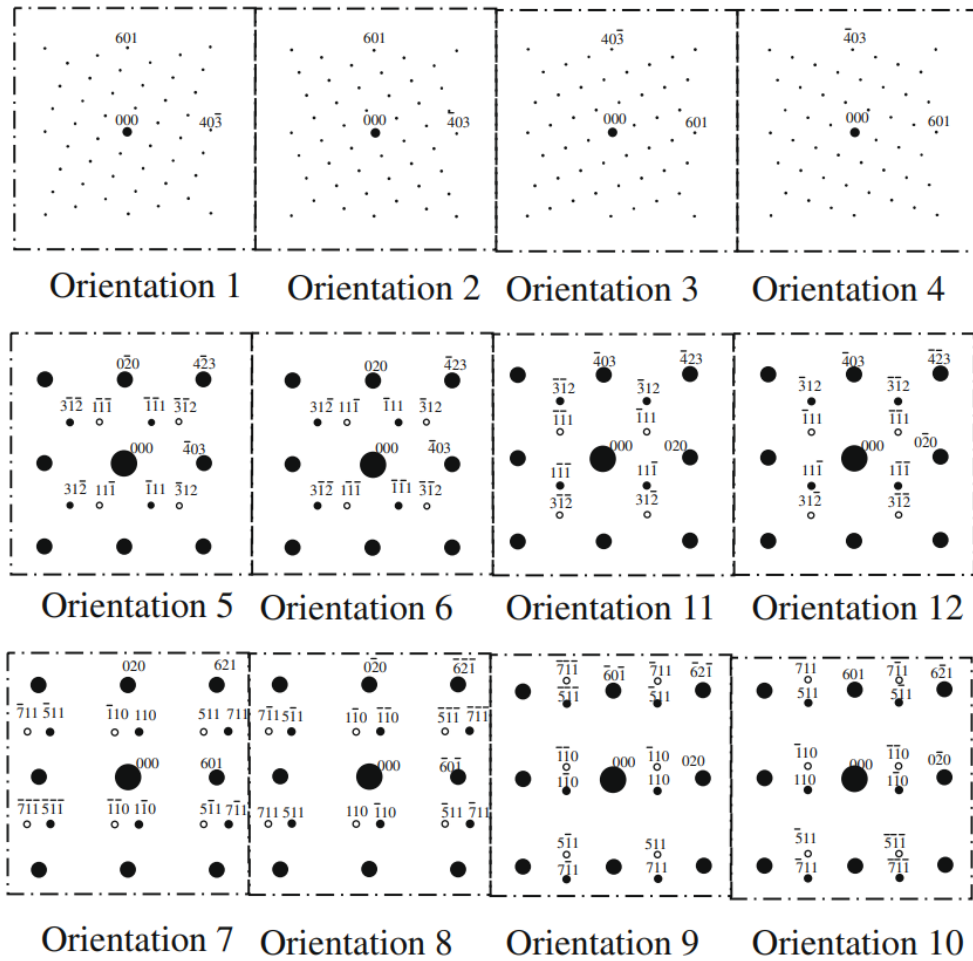
Figure 2.8: Overview of the the 12 possible diffraction patterns from β'' when the sample is oriented along the $[1\,0\,0]$ zone axis of aluminium, patterns 1-4 correspond to precipitates extending along the zone axis, while patterns 5-12 are from precipitates in the plane perpendicular to the zone axis. Taken from [33]
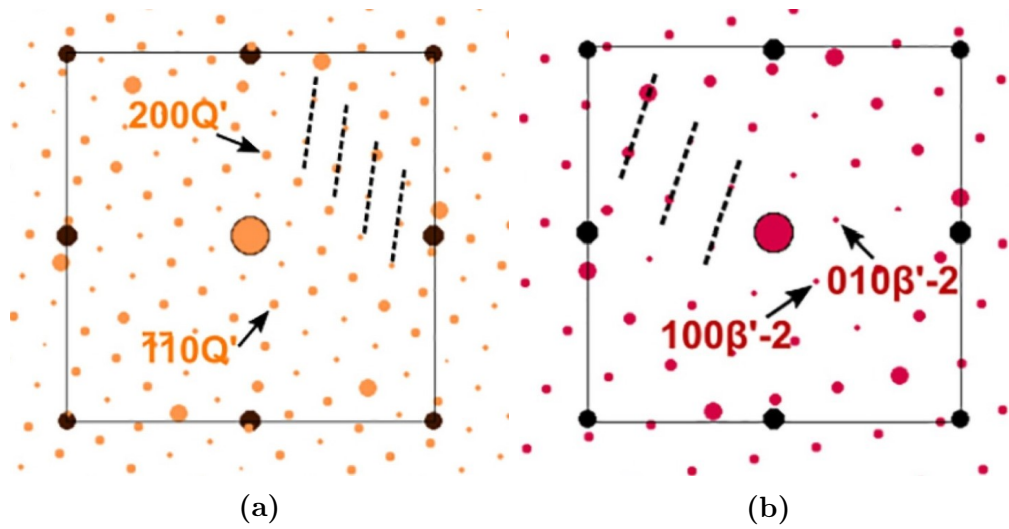
Figure 2.9: Diffraction patterns of Q' (a) and β' (b), showing the hexagonal pattern in relation to the Aluminium reflections. Both patterns may appear with a 90° rotation and/or as a mirror image. Illustration taken from [35].
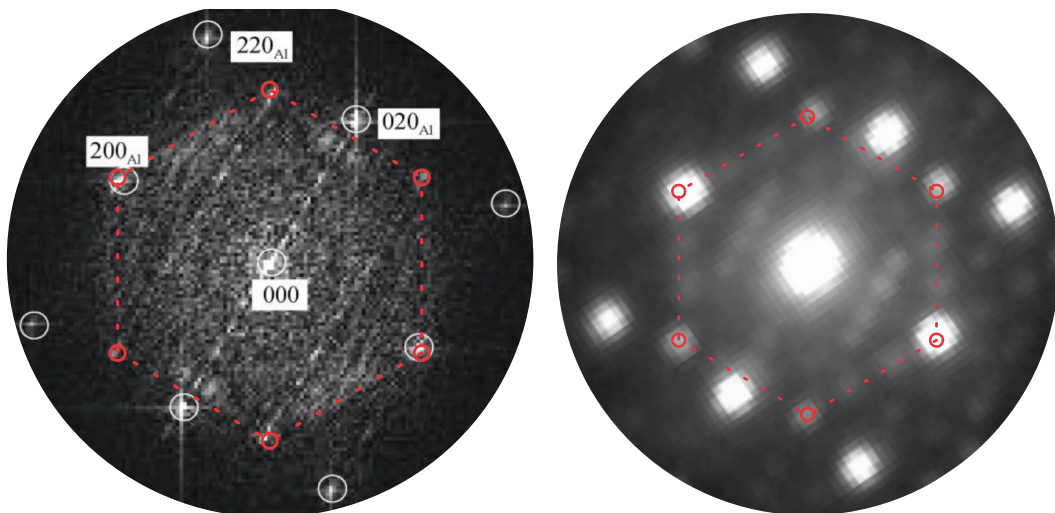
Figure 2.10: Reciprocal space of a L-phase precipitate shown as Fourier transformation of a high resolution TEM image (left) (image from [34]) and a precession electron diffraction image(right) (image from [36]). The hexagonal pattern from the Si column network is highlighted in red.

2.5   Transmission electron microscopy

Much of the information regarding transmission electron microscopy (TEM) is provided by [4] and [3] unless anything else is specified.

Since its invention in 1931, the transmission electron microscope has become arguably the most important tool for characterization of materials at the micro and nano scale as it is able to image the material down to the atomic scale, as well as performing diffraction and spectroscopy experiments from the same miniscule area. The many different modes of a TEM makes it a quite versatile tool, where many of the techniques are fields of study in their own right. A complete description of all the techniques and the theory behind them extends far beyond the scope of this report, as such only a description of the fundamentals and the techniques used in this report will be covered in this section. A general illustration of the optics of a TEM is given in Figure 2.11.
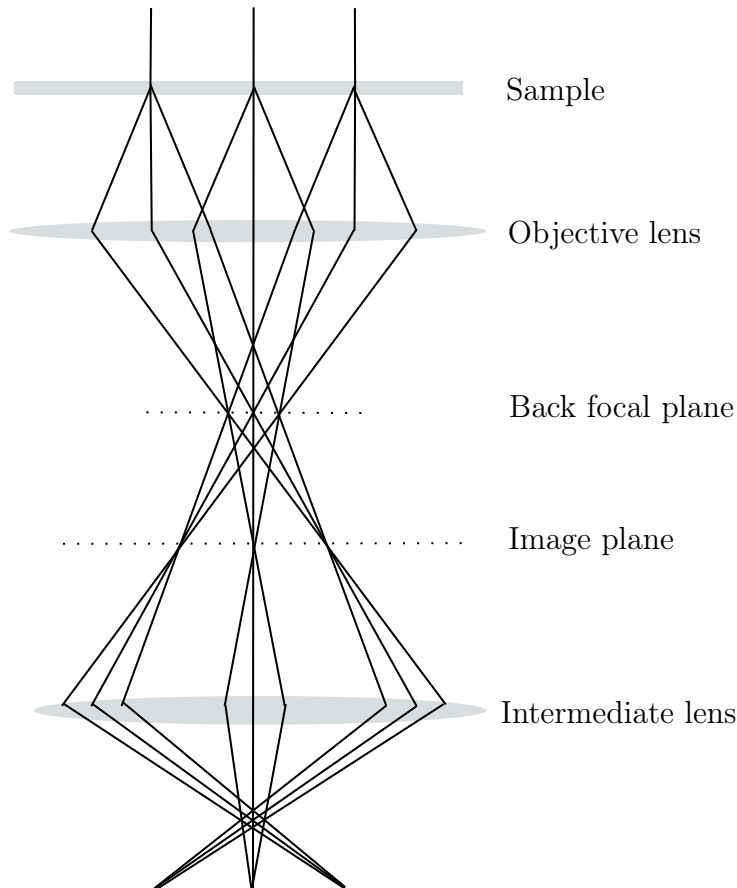

Figure 2.11: Schematic illustration of the optics in a TEM, showing how electrons are scattered by the sample and then focused to form an image. Apertures can be inserted into the different planes to change the image mode of the TEM.

Microscopes are limited in resolution by the Rayleigh criterion which states that two objects are resolved when the center of diffraction of the first object is located in the first minima of the diffraction pattern of the neighbouring object. For visible light microscopes, this criterion can be approximated with a resolution δ given by:

$$\delta = \frac{0.61\lambda}{\mu \sin \beta} \tag{2.22}$$

where λ is the wavelength of the light used, μ is the refractive index of the lens and β is the semi-angle of collection for the lens. Using visible light, the lowest resolution possible is limited to around 300 nm, which is too high for imaging the smallest structures present in materials.

In 1924, Louis de Broglie proposed that electrons, and all other particles, have wave properties, and that the wavelength of an electron is given by:

$$\lambda = \frac{h}{p} \tag{2.23}$$

where λ is the wavelength in nm, h is the Planck constant and p is the momentum of the particle, which is $p = \sqrt{(2m_e E)}$ for an electron with energy $E = eU$. Equation 2.23 for an electron accelerated by a potential U can then be expressed as:

$$\lambda = \frac{h}{\sqrt{2m_e eU}} \tag{2.24}$$

Inserting a high potential U in Equation 2.24 yields a wavelength for the electron that is significantly shorter than that of visible light, allowing smaller features to be imaged. At high values of U the velocity of the electron will be high enough for relativistic effects to be significant, and since a TEM is usually operated at potentials above 100 kV, these relativistic effects must be taken into account. Taking relativistic effects into account, Equation 2.24 becomes:

$$\lambda = \frac{h}{\sqrt{2m_e U(1 + \frac{eU}{2m_e c^2})}} \tag{2.25}$$

where c is the speed of light in vacuum. Inserting an accelerating voltage of 200kV yields a wavelength of around 2.5 pm, significantly lower than that of visible light. Using the same Rayleigh approximation for the resolution as with visible light microscopes, Equation 2.22, we find a much smaller δ for TEM. This approximation is however not valid for electron microscopes. Instead, the diffraction limited resolution, which is the theoretical resolution for a given lens of a TEM, may be approximated by:

$$r_{th} = \frac{1.22\lambda}{\beta} \tag{2.26}$$

where r_{th} is the radius of the airy disc formed by the diffraction pattern. The resolution is however further reduced by spherical and chromatic aberrations. Spherical aberrations arise as electrons further off from the optical axis are bent more strongly towards the axis than those closer to the axis, as a result the electron rays do not converge to a single point in the Gaussian image plane, but a disc surrounded by halos of decreasing intensity. The radius of this disc is given by

$$r_{sph} = C_s \beta^3 \tag{2.27}$$

where C_s is a constant dependent on the lens, approximately equal to the focal length, usually around 1-3 mm. Many modern TEMs can correct for these aberrations, the JEOL-2100 used in this experiment does however not have this feature. The other type of aberration, chromatic aberrations arise from variations in the wavelength(and therefore energy and velocity) of the electrons, as the effect the magnetic lenses has on the electrons will be dependent on the velocity of the electrons. These variations come from two sources, the first is variations in λ in the electrons emerging from the source, which is usually less than 1 eV and negligible. The other source is interactions between the sample and the electrons, which can be significantly larger at around 20 eV. Once again the electrons will form a disc in the Gaussian Image plane with a radius given by:

$$r_{chr} = C_c \frac{\Delta E}{E} \beta \tag{2.28}$$

Where $\Delta E/E$ is the relative loss in energy of the electrons. The amount of electrons that will interact with the sample and lose energy will increase as the thickness of the sample increases, resulting in the effect of chromatic aberrations being greater for thicker samples.

2.5.1   Convergent electron beam diffraction(CBED)

CBED utilizes, as the name suggests, a convergent electron beam focused on a sample to produce a diffraction pattern. Since the electron beam is focused onto a single spot, there is no need to insert an aperture, the resulting diffraction pattern will also originate from this single spot, which allows for analysis of much smaller areas than what is achievable through SAED. Another advantage of CBED is that the diffraction pattern contains very visible Kikuchi lines, which allows for easy navigation in relation to crystallographic directions when tilting the sample.

In a 1975 paper by Kelly et. al[37], a method of measuring film thickness using CBED is described. In this approach a film is tilted to a two beam condition, where only two reflections are excited, the center reflection and a diffracted reflection. In this condition the relative difference in distance between the reflections and the minima of the Kossel–Möllenstedt fringes will be determined by the thickness in the sample, through the relation

$$(s_i^2 + 1/\xi_g^2)t^2 = n_i^2 \tag{2.29}$$

where ξ_g is the extinction length given by g, the hkl plane responsible for the reflection, and n_i is an integer. s_i is the relative displacement of the ith minimum of the fringes, and can be calculated as

$$s_i = \frac{\lambda}{d^2}\left(\frac{\Delta\theta_i}{2\theta_d}\right) \tag{2.30}$$

where λ is the relativistically adjusted electron-wavelength, given by the accelerating voltage as shown in Equation 2.25, and d is the spacing between the reflections. All measurements done in this report will be performed on the $\langle 2\,2\,0\rangle$ reflection with a 200kV accelerating voltage, leaving only $\Delta\theta_i$ and $2\theta_d$ as variables, which can be found from the CBED image as shown in Figure 2.12. If Equation 2.29 is rearranged we get:
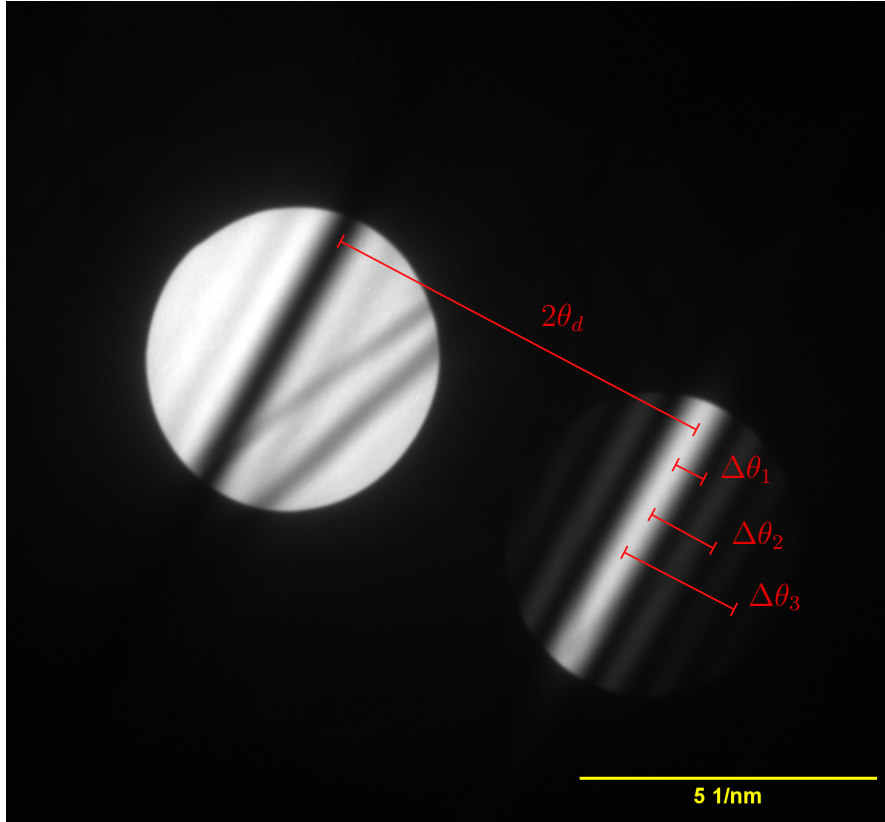
Figure 2.12: CBED image of aluminium tilted to the two-beam condition along the $(2\,2\,0)$ kikuchi lines. Showing the distances $2\theta_d$ and $\Delta\theta_i$ which can be used to calculate the thickness of the sample.

$$\frac{s_i^2}{n_i^2} = \frac{1}{t^2} - \frac{1}{\xi_g^2 n_i^2} \tag{2.31}$$

Plotting s_i^2/n_i^2 vs $1/n_i^2$ should yield a straight line where the slope of the line is given by $-1/\xi_g^2$ and the intercept with the s_i^2/n_i^2 axis corresponds to $1/t^2$. If ξ_g is known, then it is possible to find theoretical values for s_i^2/n_i^2 for a given thickness, which can be compared to the s_i^2/n_i^2 values found experimentally through Equation 2.30. A theoretical value for ξ_g is given by [38]:

$$\xi_g = \frac{\pi V_c \cos\theta_B}{\lambda \mathcal{F}_g} \tag{2.32}$$

where V_c is the unit cell volume, θ_B is the Bragg angle, λ is the electron wavelength and $\mathcal{F}_g$ is the structure factor for the g reflection. For the $\langle 2\,2\,0\rangle$ reflection of aluminium ξ_g becomes 145 nm.

2.5.2   Bright field and dark field

Bright field and and dark field TEM utilises the diffraction that occurs in the sample to achieve contrast between different features in the image. In Figure 2.11 the center spot and the diffracted spots are recombined to produce a single image, negating any difference that would have been observed due to scattering of

electrons at the different areas of the sample. By inserting an objective aperture in the back focal plane, it is possible to isolate a single spot, achieving a contrast based on diffraction. If the aperture is centered on the non-diffracted center spot, a bright field (BF) image is generated, where scattering features will have a lowered intensity. Similarly the aperture can be centered around a diffracted spot, creating a dark field (DF) image where scattering features will have a higher intensity. Figure 2.13 shows a schematic setup for DF and BF.
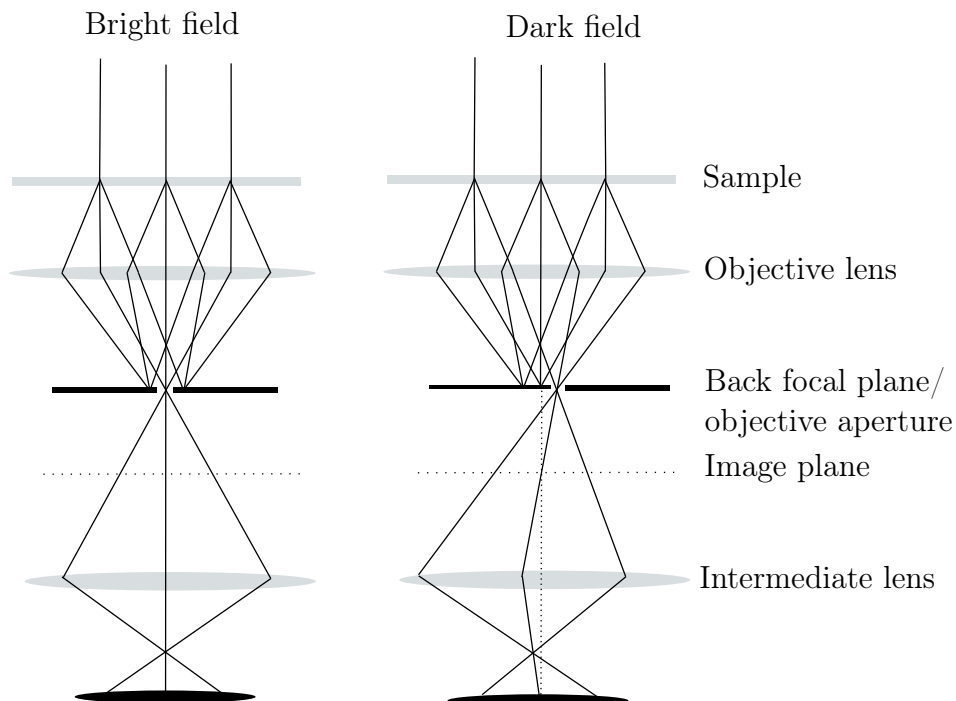
Figure 2.13: Schematic setup of bright field and dark field image modes, showing how the image is formed by inserting an objective aperture and isolating the center beam for bright field, and a diffracted beam for dark field.

For dark field the $[0\,1\,1]$ spot is suitable for investigations of precipitates, as scattering from pure Al will result in kinematic extinction of this spot (Equation 2.21), and result in zero intensity. Any intensity observed in the image will therefore be the result of scattering from precipitates.

In Al-Mg-Si alloys the previously discussed β'' precipitates tend to have strain contrast running parallel to the growth direction, which makes it possible to identify these precipitates. Other phases does not exhibit this strain contrast, which makes it possible to distinguish these phases from β'' in BF and DF TEM.

2.5.3   Scanning precession electron diffraction(SPED)

Precession electron diffraction (PED) is a technique that utilizes a focused electron probe that is rocked at a small angle (precession angle, ϕ) relative to the optical axis above the sample, creating a hollow cone of incident wave-vectors, and subsequently de-rocked below the sample. After de-rocking the beam is again parallel to the optical axis, and produces a conventional diffraction pattern similar to that produced by CBED with a small condenser aperture. The rocking and de-rocking, or precession, allows for a recording of the diffraction pattern from
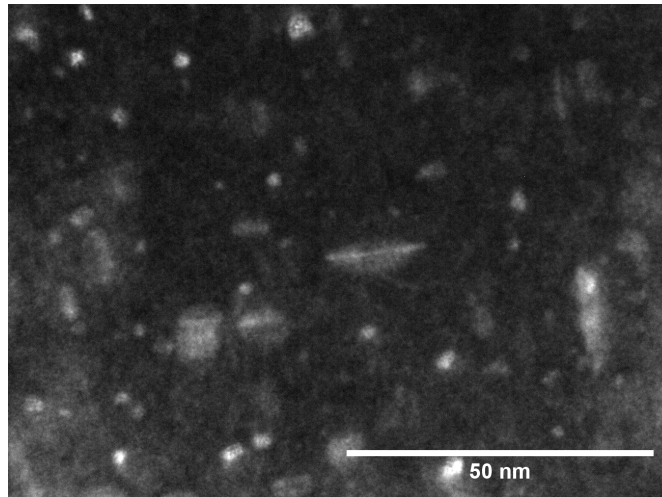
Figure 2.14: Dark field TEM image captured by inserting a small objective aperture centered at the $(0\,1\,1)$ reflection. Since the $(0\,1\,1)$ reflection is an extinct reflection i aluminium, any intensity observed is the result of scattering from some other feature than aluminium.

multiple incident wave-vectors. If the exposure time of a detector is set such that it corresponds to a whole number of rotations around the incident cone, then the recorded pattern corresponds to an integration of the patterns produced by all possible incident wave-vectors with an angle ϕ relative to the optical axis. By integrating over the entire set of incident wave-vectors, the dynamic effects present from any single wave-vector is suppressed, and the resulting diffraction pattern is more kinematic in nature.

By combining PED with the scanning capabilities of a STEM it is possible to record the PED-patterns at multiple points across a larger region of a sample, a technique referred to as scanning precession electron diffraction (SPED). SPED generates 4D data-sets, consisting of a 2D navigation space across real space, where each point has a corresponding diffraction pattern recorded from reciprocal space in a 2D-signal. The SPED datasets therefore contains useful information of the material at each point in the navigation space. From this data it is possible to construct orientation maps, phase maps in multi-phase materials, and much more. In this thesis SPED will be used to identify precipitate phases in the HAZ of the M-alloy.

2.5.3.1 SPED data analysis

The large 4D-data-sets generated by SPED contains a lot of useful information, however in order to fully realize the potential of the technique the data needs to be processed and analyzed.

A raw SPED data-set of size $n_x \times n_y$ in navigation space will contain $n_x \times n_y$ PED-patterns, however the number of unique patterns (if signal noise is ignored) is much lower. At a minimum, if the SPED scan is from a single perfect crystal, then all PED patterns should theoretically be the same, and the entire data-set can be reduced to a single unique pattern. For multi-phase materials the number of unique diffraction patterns will be greater than 1, but still much lower than $n_x \times n_y$. If the dataset is represented as a large 2D matrix $\boldsymbol{X}$ with dimensions
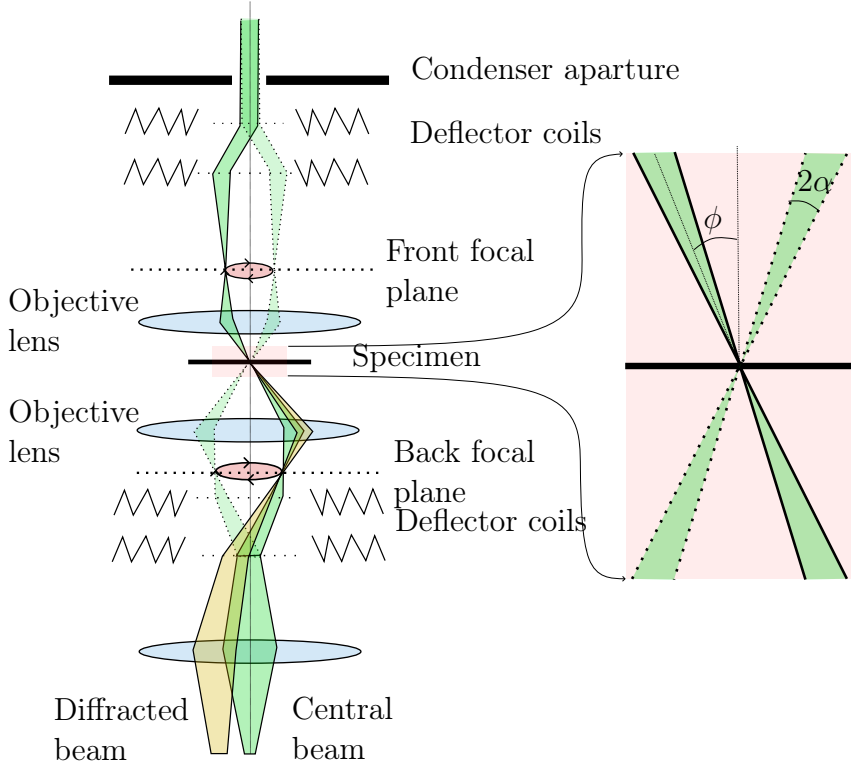
Figure 2.15: Illustration of the principle behind PED. The electron probe is converging on the sample with a convergence semi-angle α. The electron beam is tilted of the optical axis, such that the probe approaches the specimen at a precession angle ϕ. The probe is also precessed around the optical axis, such that all incident wave-vectors with an angle ϕ relative to the optical axis are recorded if the exposure time is set equal to an integer number of precession periods. The probe is then re-deflected to run parallell with the optical axis. The convergence semi-angle α and the precession angle ϕ is exaggerated for illustration purposes. Illustration drawn with inspiration from [22].

$n_x * n_y \times n_{sx} * n_{sy}$, where $n_{sx} \times n_{sy}$ is the dimensions of the signal space, then $\boldsymbol{X}$ can be written as;

$$\boldsymbol{X} = \boldsymbol{LF} \tag{2.33}$$

where $\boldsymbol{F}$ is the factor matrix with dimensions $K \times n_{sx} * n_{sy}$ that contains each unique signal in signal space, with K being the number of unique signals. And $\boldsymbol{L}$ is the loading matrix with dimensions $n_x * n_y \times K$, describing the loading of each factor in navigation space. For multi-phase materials K should in theory be equal to the number of phases present (multiplied by the number of allowed orientations for each phase), however in practice signal noise and defects in the crystal will significantly increase the number of unique signals. It is therefore more beneficial to set K to some expected value and find $\boldsymbol{F}$ and $\boldsymbol{L}$ such that the Frobenius norm $||\boldsymbol{X} - \boldsymbol{LF}||_F$ is at a minimum.

In many cases the best fit for $\boldsymbol{F}$ and $\boldsymbol{L}$ contains negative components, these negative values do however not have any meaningful physical interpretation. In signal space the minimum value recorded in any diffraction pattern is 0, decomposing the factors into negative values is therefore undesired. The PED signal observed

in a given point in navigation space is dependent on what phases are present at that point. Since a given phase is either present or not present, the corresponding factor to this phase must follow the same rule, in other words the contribution of this cannot be less than 0. Non-negative matrix factorisation (NMF) is a method that restricts the components in F and L to be strictly non-negative, which results in the loadings and factors having a clearer physical physical interpretation. Since components cant be subtracted in NMF the factors are more likely to separate in into separate parts.

2.6 Precipitate statistics

As earlier mentioned the mechanical properties of 6xxx aluminium alloys will depend on the precipitates present in the aluminium matrix. Phase, size and numerical density (ρ_i) are all factors that determine the final properties of the alloy, and can be determined through TEM. An estimate for ρ_i can be determined by counting precipitates in the $[1\,0\,0]$ direction through Equation 2.34.

$$\rho_i = \frac{3N_{100}}{A * t} \tag{2.34}$$

where A is the area imaged, t is the thickness of the sample and N_{100} number of precipitates oriented in the $[1\,0\,0]$ direction, a factor of 3 is included to account for precipitates in the $[0\,1\,0]$ and $[0\,0\,1]$ directions, as the amount of precipitates should be equal in all $\langle 1\,0\,0\rangle$ directions. The thickness can be determined through CBED diffraction as described earlier.

Some geometrical adjustments must be considered get an accurate value of ρ_i, as the precipitates could originally have extended beyond the thickness of the sample. For precipitates oriented in the $[1\,0\,0]$ direction, this adjustment is simple. By assuming that these precipitates will be visible as long as a small segment is within the sample, it becomes evident that any sample of length l will be visible not only when they are centered within the sample thickness, but also if it is centered $\pm l/2$ of the sample. When adjusting for this Equation 2.34 becomes:

$$\rho = \frac{3N}{A * (t + \langle l\rangle)} \tag{2.35}$$

As Equation 2.35 shows, it is not possible to find the number density of precipitates without first finding the length of the precipitates, which can be found from the in-plane $[0\,1\,0]$ and $[0\,0\,1]$ precipitates. The in-plane precipitates can also extend out of the surface, compensating for this is not as trivial as with $[1\,0\,0]$ oriented precipitates. Figure 2.16 shows how precipitates in tilted samples extend out of the sample, as the angle between the $(1\,0\,0)$ plane and sample surface (Φ) increases, an increasing number of the precipitates will extend out of the sample. For a given tilt in x and y direction, the total tilt is given by:

$$\Phi = \arccos\left(\cos\theta_x * \cos\theta_y\right) \tag{2.36}$$

The $[0\,1\,0]$ and $[0\,0\,1]$ directions will in most cases not align with the direction of highest tilt, but will be at some angle relative this. If θ is the angle between $[0\,1\,0]$ and the highest tilt direction, then the angle for $[0\,0\,1]$ will be $\pi/2 - \theta$. The

amount of precipitates that extend out of the sample will also be dependent on the measured length of the precipitates relative to the thickness of the sample. When adjusting for these factors the adjusted length of the precipitates becomes:

$$\langle l \rangle = \frac{\langle l \rangle_m}{1 - (\langle l \rangle_m / t) * \cos\theta \tan\Phi} \tag{2.37}$$

where $\langle l \rangle_m$ is the average measured length of the precipitates. The last measurement that needs to be done is the cross section of each precipitate, which is rather straight forward, as the measured value does not need to be corrected. We now have all we need to calculate the volume fraction of precipitates, $\frac{V_p}{V_{tot}}$, given by:

$$\frac{V_p}{V_{tot}} = \langle CS \rangle \langle l \rangle \rho \tag{2.38}$$

where $\langle CS \rangle$ is the average cross section of the precipitates.
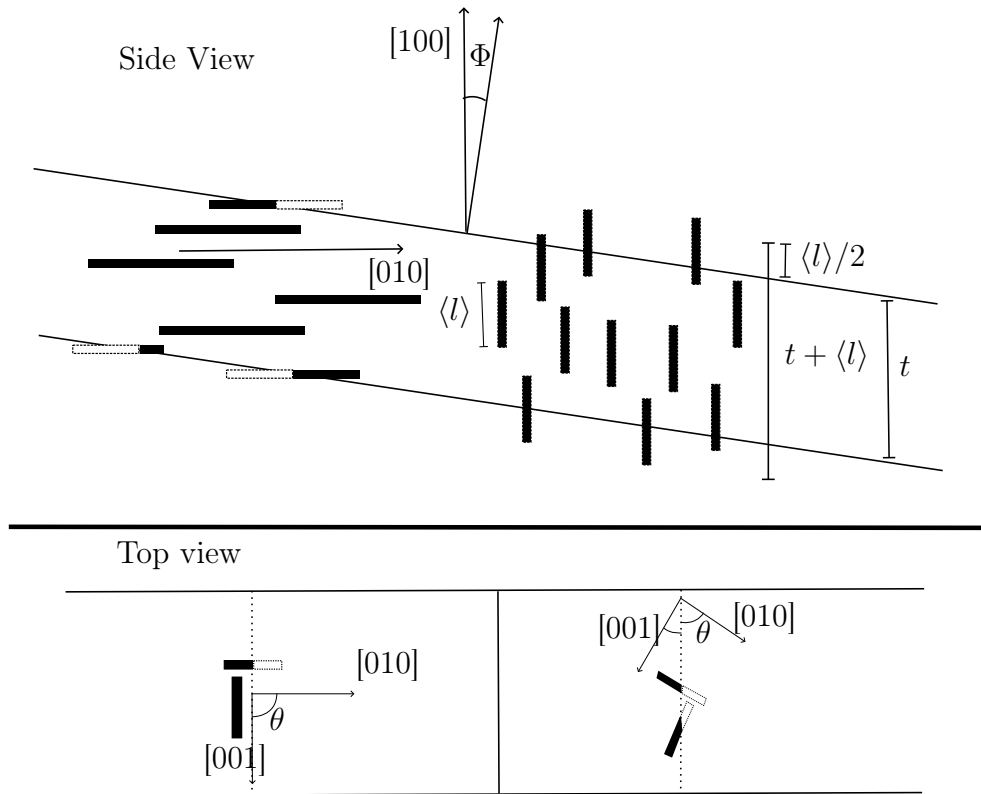
Figure 2.16: Illustration of how geometry will influence the perceived number and length of precipitates when the sample is tilted by an angle Φ. The structures that will be visible in the TEM are coloured black, while the parts of the precipitates that have been removed during sample preparation, and are not visible, are marked with a dotted outline. In the side view it is illustrated that precipitates oriented along the optical axis are visible are visible as long as they were centered within $\langle l \rangle / 2$ distance of the sample surface before sample preparation. While the parts of in-plane precipitates that extended past the sample surface before sample preparation are not visible. In the top view the illustrated precipitates are in the same $(1\,0\,0)$ plane, with a tilt Φ relative to the surface of the sample, the dotted line represents the intersection between the $(1\,0\,0)$ plane and the sample surface. θ is the angle between the $[0\,1\,0]$ direction and this intersection. If $\theta = 0$ or $\pi/2$ precipitate shortening is only possible in 1 direction.

MATERIAL AND EXPERIMENTAL METHOD

3.1   The material

An Al-Mg-Si-Cu alloy consisting of 4 mm thick and 50 mm wide extruded profiles was used in this experiment, and was provided by Neuman aluminium [39]. This alloy will from here on be referred to as the M-alloy. A detailed chemical composition of the M-alloy is given in Table 3.1. The alloy was heat treated to the T6 condition using the temperature profile described in Figure 3.1.
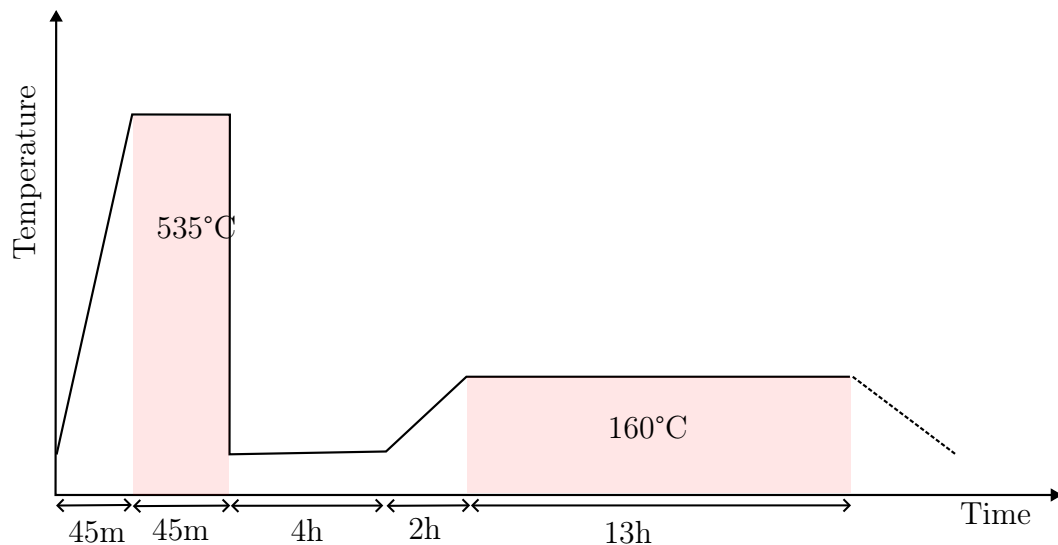
Figure 3.1: Heat treatment of the M-alloy to the T6 condition prior to welding, as provided by Neuman. Solution heat treatment performed by 45 minutes heating to 535°Cand held at 535°Cfor another 45 minutes. Followed by quenching in water and natural aging at room temperature for 4 hours. Then artificial ageing by heating to 160°Cover 2 hours and aged at that temperature for 13 hours.

Two 4 mm thick plates of M-alloy was HYB-welded together using a AA6082 alloy in the T4 condition as filler wire, the wire was 1.4 mm in diameter and the composition of the material is given in Table 3.1. The surfaces of the two plates that were to be welded together were prepared by polishing with a 80 mesh sandpaper and cleaned with acetone. The plates were separated by a 2 mm groove, with the 7 mm diameter bobbin pin of the welding head placed in the

Table 3.1: Elemental composition of the M-alloy and the filler wire used for the HYB-weld

Element	Si	Fe	Cu	Mn	Mg	Zn	Cr	Ti	Al
w% M-alloy	0.677	0.360	0.200	0.267	0.768	0.134	0.01	0.04	97.50
w% filler-wire	1.11	0.20	0.002	0.51	0.61	-	0.14	0.43	97.25
a% M-alloy	0.654	0.175	0.085	0.132	0.857	0.056	0.005	0.023	98.014
a% filler wire	1.070	0.097	0.001	0.251	0.679	-	0.073	0.243	97.59

groove between the plates, with a slight displacement towards the AS to remove surface oxides present during welding. The welding speed was 18 mm/s, with a wire feed rate of 125 mm/s. The gross heat output of the weld was 0.15 kJ/s. The welding process was performed by Hybond.

The heat output from the welding process causes a spike in temperature in the materials, the exact temperature reached during the welding process is unknown, but is dependent on the distance from the weld. Figure 3.2 Shows a sketch of the temperature profile of the material with the heat output from the welding process included.
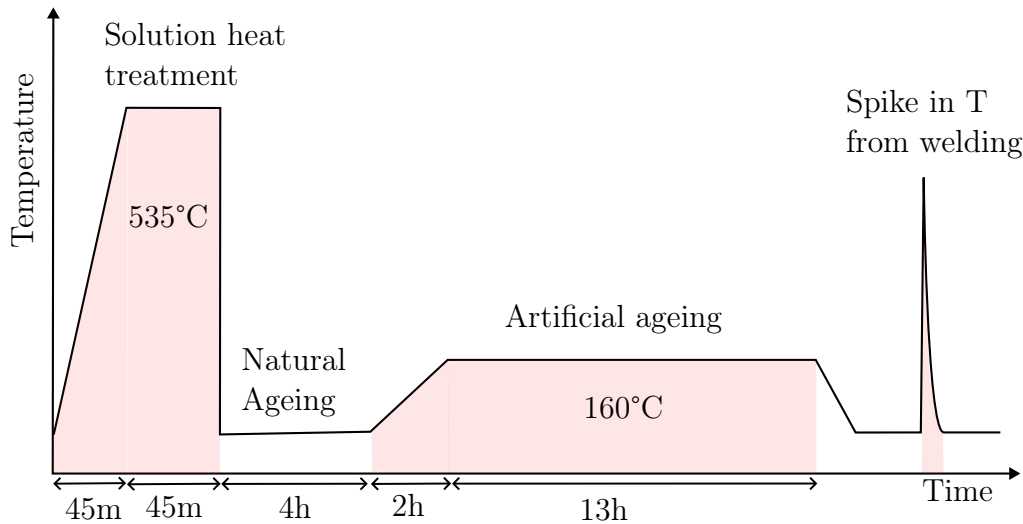
Figure 3.2: Heat treatment of M-alloy to achieve T6 condition with the heat influx of HYB-welding included. The temperature profile sketches a region close to the EZ/HAZ interface, where the spike in temperature during welding is high. The exact temperature peak during HYB-welding is unknown and decreases with distance from the EZ/HAZ. After welding the temperature decreases back to room temperature within a couple of minutes.

After welding, the sample was stored away for a significant time, such that the maximal effect of post-welding natural ageing was reached. Hardness measurements were performed through the weld and the HAZ, these measurements were performed by researchers at SINTEF. From these measurements the HAZ was identified, which was used to determine which regions would be investigated with TEM.

The temperature profile has been simulated by Jørgen Sørhaug [40], based upon the Ph.D thesis by Øyvind Frigaard [41]. The method solves Rosenthals

equation for temperature distribution during welding of thin plates. The temperature profiles are then used as input in the model described by Myhr & Grong [42]. This was then used as input in a model that predicts hardness. Relevant parts of this simulation will be presented and discussed in relation to the TEM experiments in this thesis.
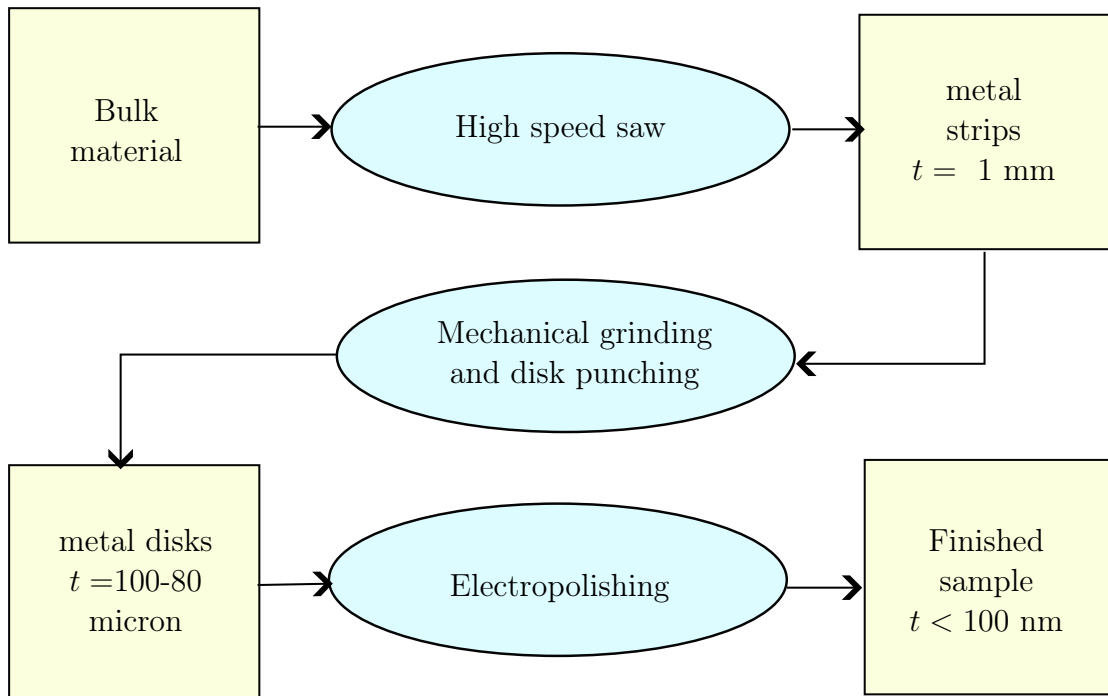
3.2   Sample preparation

Figure 3.3: Flowchart of the steps in the sample preparation method, showing the methods used in blue ovals and the state and thickness of the samples in yellow boxes.

TEM-samples were extracted from the HAZ of the AS of the HYB-welded plates, a total of 4 sample series were made, with each series consisting of 4 samples. Each series corresponded to a given distance from the EZ/HAZ interface, ranging from 1-4 mm. Figure 3.4 shows where the sample series were extracted from in relation to the hardness profile. The samples were prepared using mechanical grinding and electropolishing. A flowchart of the sample preparation process is shown in Figure 3.3

From the bulk welded material 2 metal strips with a thickness of approximately 2 cm were extracted perpendicular to the welding direction using a Struers Secotom High speed saw. From these strips two thinner strips were extracted from the HAZ with a thickness of approximately 1 mm in the plane parallel to the weld, each of these thinner strips represents a single series. From the first large strip the thin strips were cut at a distance of 1 and 3 mm from the weld, from the second large strip the thin strips were extracted from 2 and 4 mm.

The thin strips were then mechanically grinded down to a thickness of approximately $100\,\mu m$ using a Struers rotopol polishing machine with silicon carbide
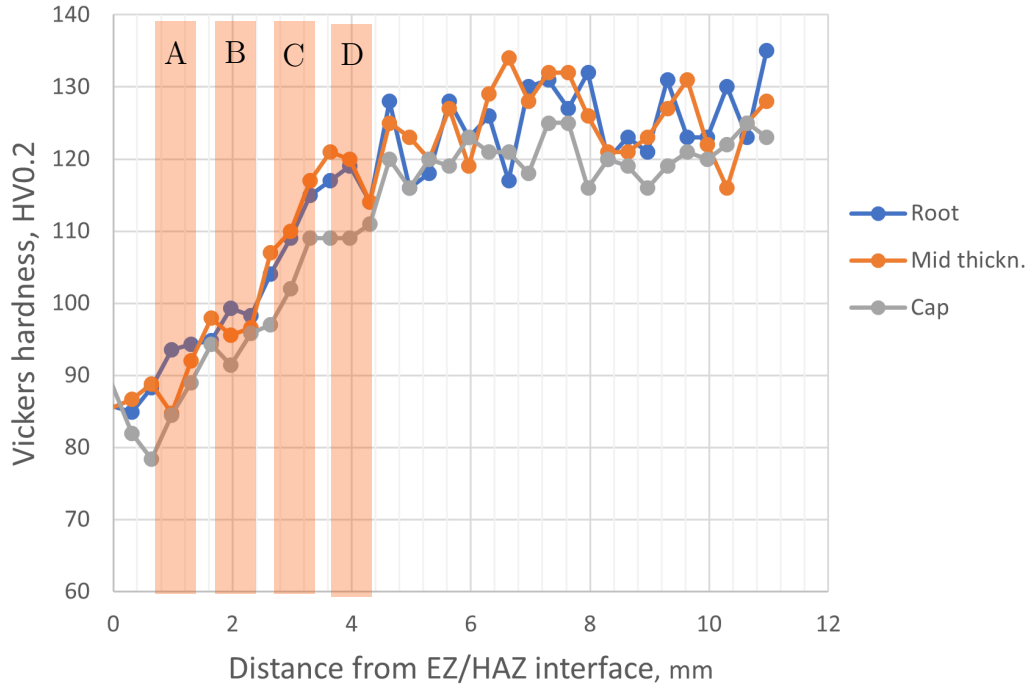
Figure 3.4: Hardness measurements of the HAZ and base material on the AS. The X-axis is centered on the EZ/HAZ interface. The regions marked A, B, C and D illustrates where the TEM sample series were extracted from in relation to the hardness profile.

Table 3.2: Overview of the sample series and their respective distances from the weld

Sample series	distance from weld
A	1 mm
B	2 mm
C	3 mm
D	4 mm
Ref	∞

grinding paper with different grits. The Grits used were P320, P400, P800, P1200, P2500 and P4000, starting with P320 and gradually transitioning to finer grits. A continuous stream of water was applied to the grinding paper to reduce friction and prevent a rise in temperature, for the finest grits, P2500 and P4000, soap was applied to further reduce the friction. When the desired thickness was reached a disk puncher was used to extract samples from each strip.

As a final step each of the samples were electropolished using a Struers Tenupol Electropolishing unit. A solution of 2:1 methanol and concentrated nitric acid was used as electrolyte for the elctropolishing reaction. The solution was held at a temperature between -20 °Cand -30 °Cby the addition of liquid nitrogen. The electropolishing unit was set to a working voltage of 20V with a flow rate 20 and a light stop value of 50. After polishing, the samples were rinsed using methanol followed by ethanol before being inspected in an optical microscope to confirm a satisfactory result.

3.3 Quantitative precipitate investigation

The TEM-investigation of the precipitates is divided into two parts, the first is a quantitative analysis of the number density and size of the precipitates, the second is a phase identification.

For the quantitative analysis each of the samples were investigated using bright field TEM. The BF images were captured using a JEOL-2100 microscope equipped with a JEOL-EM-31680 double tilt sample holder. The operating voltage was set to 200 kV. Each sample was investigated for regions where the sample was sufficiently and uniformly thin, and where the $[1\,0\,0]$ zone axis is reachable within a small tilt angle. At the suitable regions the samples were tilted to align with the $[1\,0\,0]$ aluminium zone axis of the aluminium. BF images were captured using a $150\,\mu m$ condenser aperture and a $50\,\mu m$ objective aperture. After imaging the objective aperture was removed and the condenser aperture was changed to $50\,\mu m$ for CBED imaging. The sample was then tilted to the 2-beam condition following the $(2\,2\,0)$ Kikuchi lines where a two-beam image was captured for thickness estimation.

The images were then analysed using the ImageJ software. From the BF images measurements of the cross-section and length of the precipitates were performed, as well as a count of the number of precipitates. From the CBED images the thickness of the samples were estimated using based on Equation 2.31, using a script based on code provided by Christoph Hell. From these measurements the average size, number density and volume fraction occupied by the precipitates were calculated.

3.4 Phase identification of precipitates

SPED was used to investigate what phases are present at different distances from the EZ/HAZ interface. This was done using a JEOL 2100F microscope at an accelerating voltage of 200 kV, equipped with a Merlin direct electron detector. SPED scans were performed on 3 different samples, B2, C3 and D4, all oriented along the $[1\,0\,0]$ zone axis. All the successful scans, those that were analyzed, was performed by Jørgen Sørhaug. Scan parameters for the different samples are shown in Table 3.3

Table 3.3: SPED scan parameters used for the different scans anlyzed in this thesis

Sample	B2	C3	D4
Spot size (nm)	0.5	0.5	0.5
Convergence angle (deg)	0.5	0.5	0.5
Camera length (cm)	12	12	15
Precession frequency (Hz)	100	100	100
Exposure time (ms)	40	40	30
Scan size	608×160	640×256	512×192
Step width (nm)	1.852	1.852	1.852

The SPED data-sets were processed and analysed using the HyperSpy extension [43] for Python. Each data-set was preprocessed by being calibrated, centered
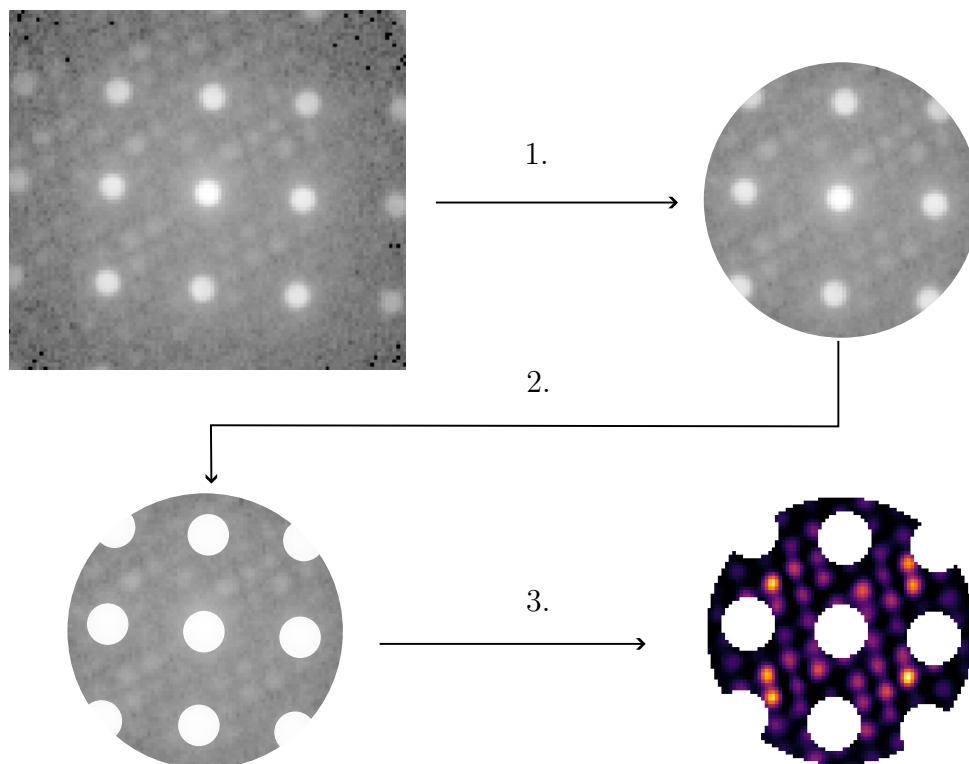
Figure 3.5: Flowchart of the steps taken to analyse the signal-space of the SPED-datasets. The preprocessing steps of centering and binning the signals are not shown. The steps shown are; (1) Removing any signal further from the $(0\,0\,0)$ spot than the $\{0\,2\,2\}$ aluminium spots, (2) masking out the diffraction pattern of aluminium and (3) decomposition into precipitate diffraction patterns.

and binned before analysis. Using NMF the datasets were decomposed into factors and loadings, where the factors correspond to different patterns found in signal space and the loadings correspond to where these patterns are present in navigation space. The decomposition was performed with a mask applied to the signal space, ignoring any signal further from the center than the $\langle 0\,2\,2\rangle$ spots of Al as well as the $[0\,0\,0]$, $\langle 0\,0\,2\rangle$ and $\langle 0\,2\,2\rangle$ aluminium spots, the masks applied are shown in Figure 3.6. The ideal number of components for decomposition were determined by trying different values and finding the highest possible value for K before over-decomposition became a significant problem.

After decomposition each factor was investigated to identify which phase they corresponded to. After identification, the corresponding loadings were used to create a phase map.

(a) B2 mask

(b) C3 mask

(c) D4 mask
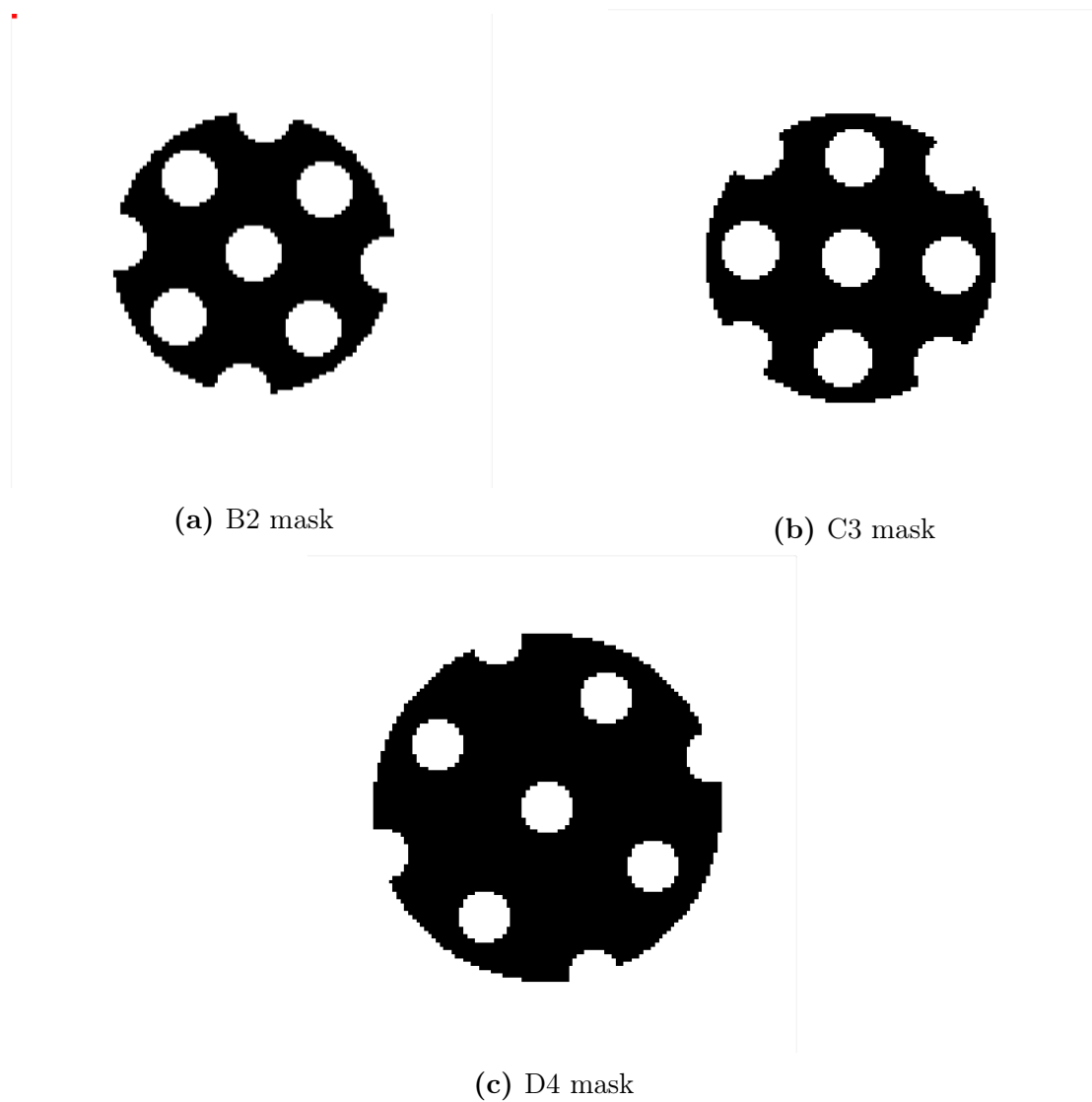
Figure 3.6: Masks applied to the signal space during NMF decomposition of the SPED data-sets. The radius of the masks is set to be equalt to the distance between the $(0\,0\,0)$ central spot and the $\{2\,2\,0\}$ aluminium reflections, such that all regions signal detected further out in reciprocal space is ignored. In addition the $(0\,0\,0)$, $\{2\,0\,0\}$ and $\{2\,2\,0\}$ reflections from aluminium are masked out. The difference in size of the D4 mask and the B2 and C3 masks s a result of the difference in cameralength used.

FOUR

RESULTS

4.1 Hardness measurements and temperature simulations

This first section covers the results from the hardness measurements and temperature simulation. Neither of these experiments were performed as a part of this thesis, however as the results of these experiments are important for the discussion of the results observed with BF-TEM and SPED, they are presented here. The hardness measurements was used to determine which regions of the HYB-weld would be investigated. The temperature simulation provides useful supplemental information, that can be used to better understand the changes observed.

The results from the hardness measurements through the weld is shown in Figure 4.1. From the hardness profile it was determined that the HAZ extended approximately 4-5 mm from the edge of the EZ on the AS, and 6-7 mm on the RS. Based upon this information TEM-samples were extracted from regions that corresponded to 1, 2, 3 and 4 mm distance from the EZ on the AS. Figure 3.4 shows where the TEM-samples were extracted from in relation to the hardness curve.

The temperature simulation gave a temperature profile as a function of time and distance from the weld, based upon trial and error to find a heat-input that yielded a hardness profile similar to what was observed. The temperature evolution over time for the HAZ is shown in Figure 4.2, and the maximum temperature reached in each region is shown in Figure 4.3.

In the simulation, the heat output from the welding source was simulated as a point source, while in reality the heat output is distributed over a finite volume. As a result of this the maximum temperature reached in the regions close to the weld is higher in the simulation than in reality. As distance from the weld increases the accuracy of the simulation is also increasing.
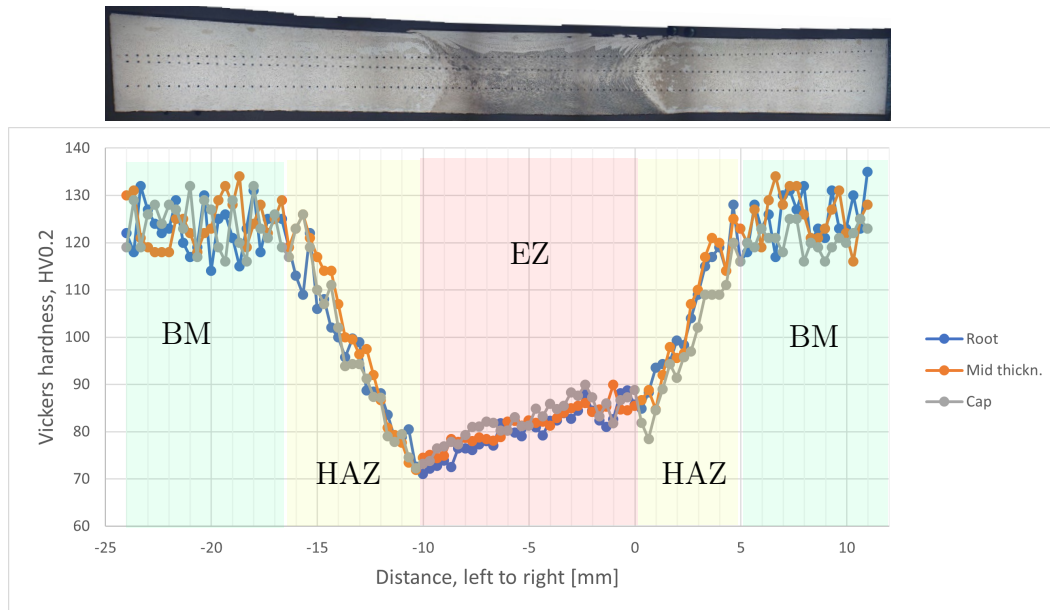
Figure 4.1: Hardness measurements of the cross-section of the welded plates, with the RS on the left and AS on the right. The top image shows an image of the cross section of the welded plate. The x-axis is centered on the EZ/HAZ interface. The three different measurements stem from the bottom(Root), middle and top(Cap) of the plate, with top/bottom defined in relation to the extrusion chamber.
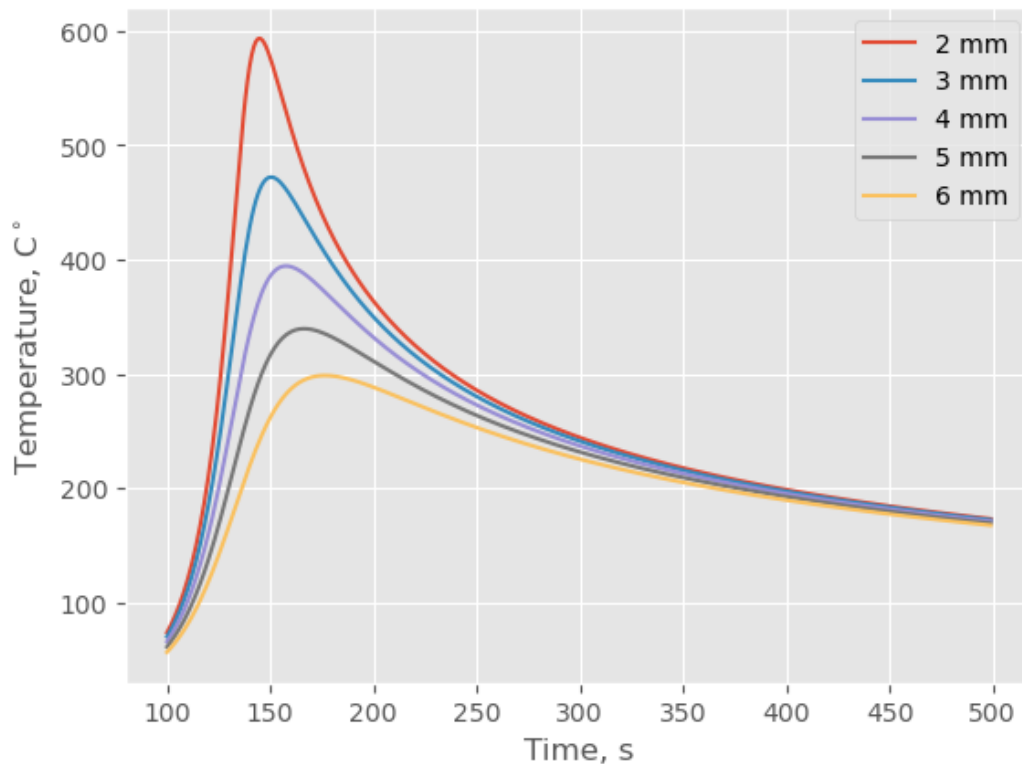
Figure 4.2: Simulated temperature during welding as a function of time at different distances from the EZ/HAZ interface.
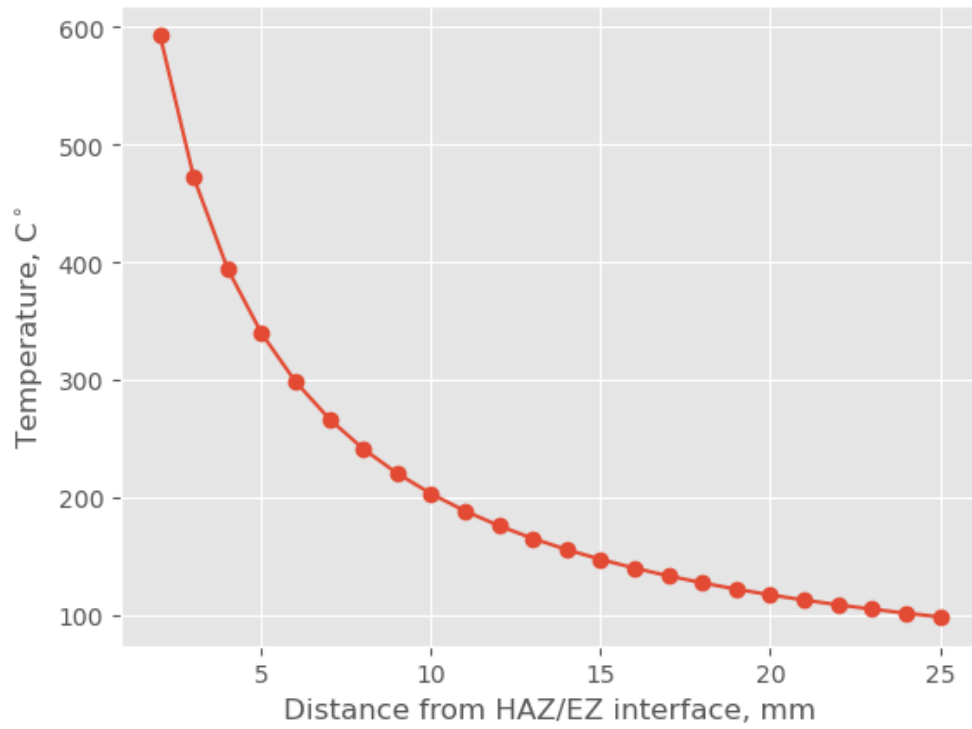
Figure 4.3: Maximum temperature reached during welding as a function of distance from the weld(in mm).
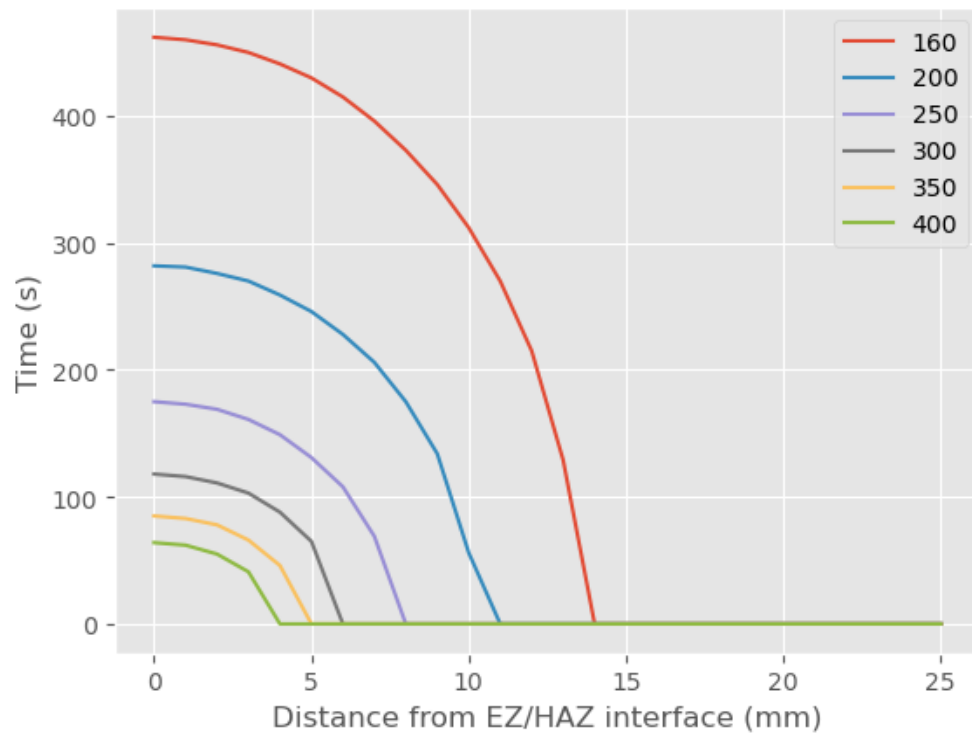
Figure 4.4: The amount of time spent above the given temperatures as a function of distance from the EZ/HAZ interface. The temperatures are given in °C.

4.2   Precipitate statistics

Statistics regarding the size and density of precipitates was collected by inspection of BF images taken of each sample. For the density measurements each image was inspected for suitable regions, defined by an even illumination and clearly visible precipitates. The area covered by this region was then measured and all precipitates oriented along the $[1\,0\,0]$ zone axis was counted. Combined with the corresponding CBED thickness measurement for this region it was possible to calculate the numerical density of precipitates in each inspection region. While counting the precipitates where marked with an oval overlay, covering the cross section of the precipitate. The area covered by these overlays was used to estimate the cross section of the precipitates. The length measurements was performed by measuring the length of all clearly visible precipitates with extension in the $(1\,0\,0)$ plane.

A summary of the results from precipitate measurements is given in Table 4.1, with the total number of measurements performed given in Table 4.2.

Table 4.1: Summary of the results from the statistical investigation of the precipitates.

Series	$\langle l \rangle$ (nm)	$\langle CS \rangle$ (nm^2)	$\langle \rho \rangle$ ($10^3/\mu$m^3)	V_p/V_{tot} (%)
Reference	6.82 ± 3.717	6.297 ± 2.048	188 ± 38	0.806
A	28.52 ± 27.37	-	-	-
B	14.49 ± 9.71	10.44 ± 3.405	47 ± 16	0.712
C	7.39 ± 3.703	6.03 ± 2.635	118 ± 19	0.527
D	5.75 ± 3.48	5.49 ± 1.667	168 ± 32	0.530

FIX

Table 4.2: Overview of the statistical basis for the averages presented in Table 4.1, showing the amount of regions inspected, total number of precipitates counted for density estimation and precipitates measured for length estimation.

Series	Regions	Precipitates counted	Lengths measured
Ref	13	607	123
A	-	-	200
B	24	807	297
C	15	584	125
D	17	1069	225
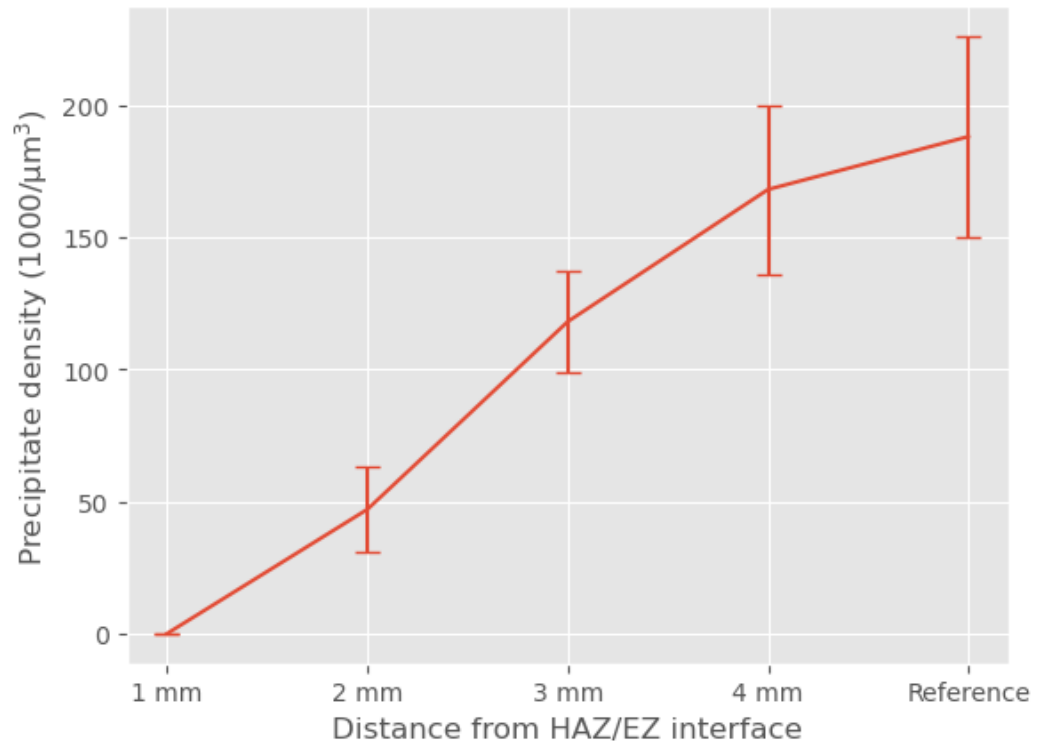
Figure 4.5: Number density of precipitates as a function of distance from the EZ/HAZ interface
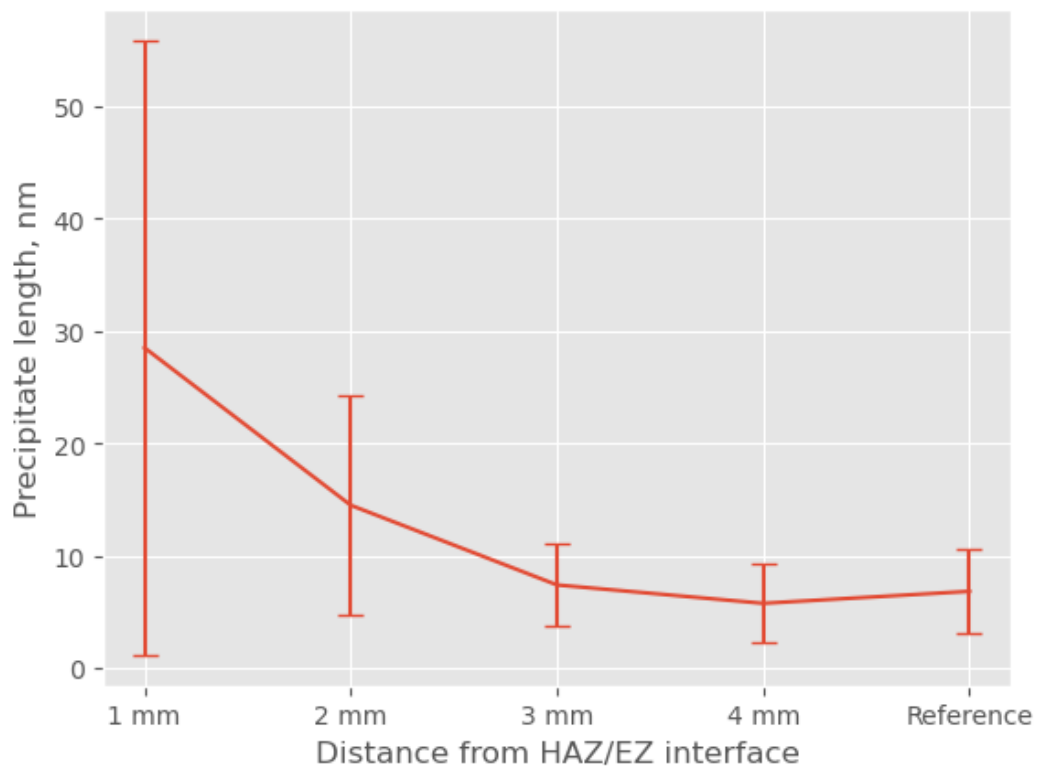
Figure 4.6: Changes in average length of precipitates as a function of distance from the EZ/HAZ interface.

(a) Series A, 1 mm from the EZ

(b) Series B, 2 mm from the EZ

(c) Series C, 3 mm from the EZ

(d) Series A, 4 mm from the EZ
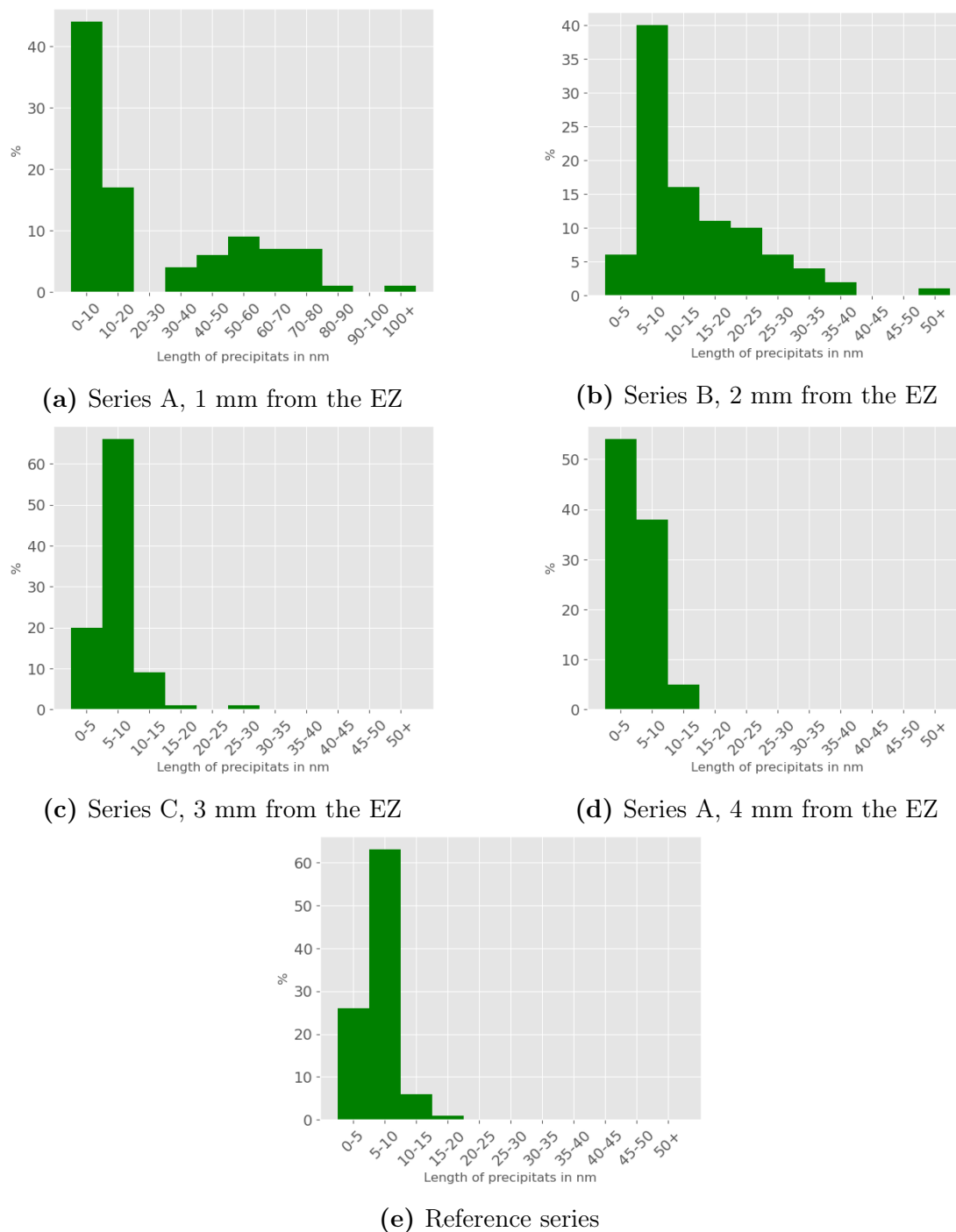
(e) Reference series

Figure 4.7: Distribution of measured precipitate length at different distances from the EZ/HAZ interface. The distribution is shown in a length ranges of 10 nm in (a), while (b-e) has the distribution shown in length ranges of 5 nm.

In the reference series as well as series C and D, the precipitates were found to mostly have needle shapes, and the characteristic double strain contrast observed in β'' precipitates. As the distance to the EZ/HAZ interface decreased, the amount of lath shaped precipitates increased. Examples of lath and needle shaped precipitates are shown in Figure 4.8
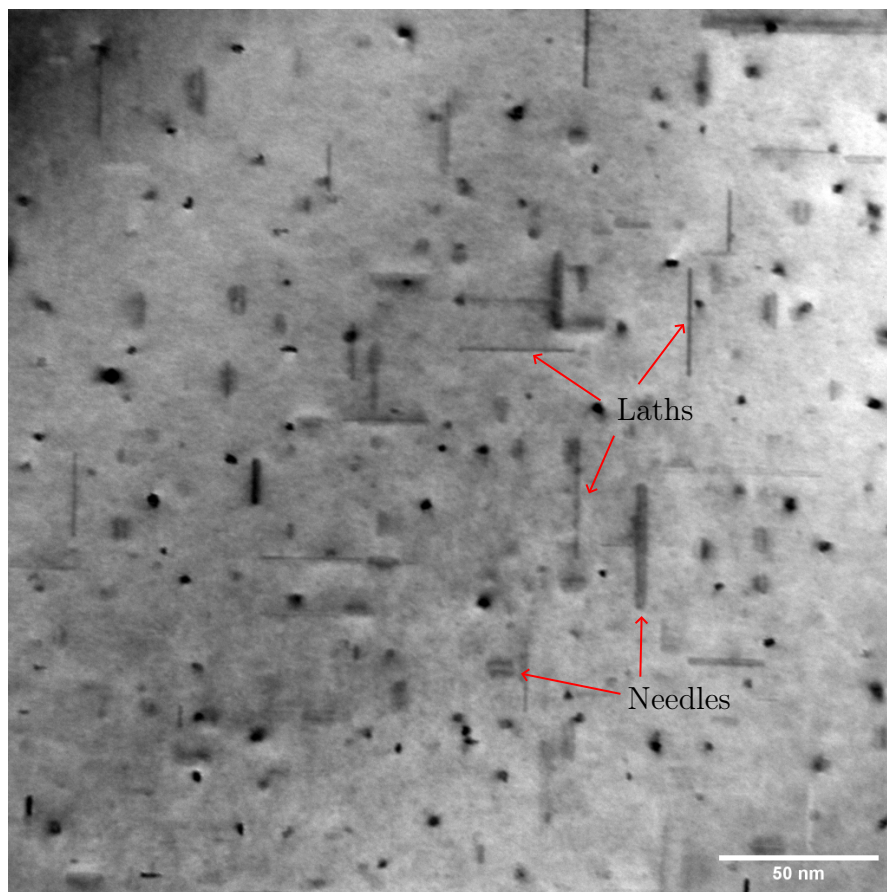
Figure 4.8: TEM image from series B (2 mm from the HAZ/EZ interface) showing examples of lath and needle shaped precipitates.

(a)

(b)

(c)

(d)
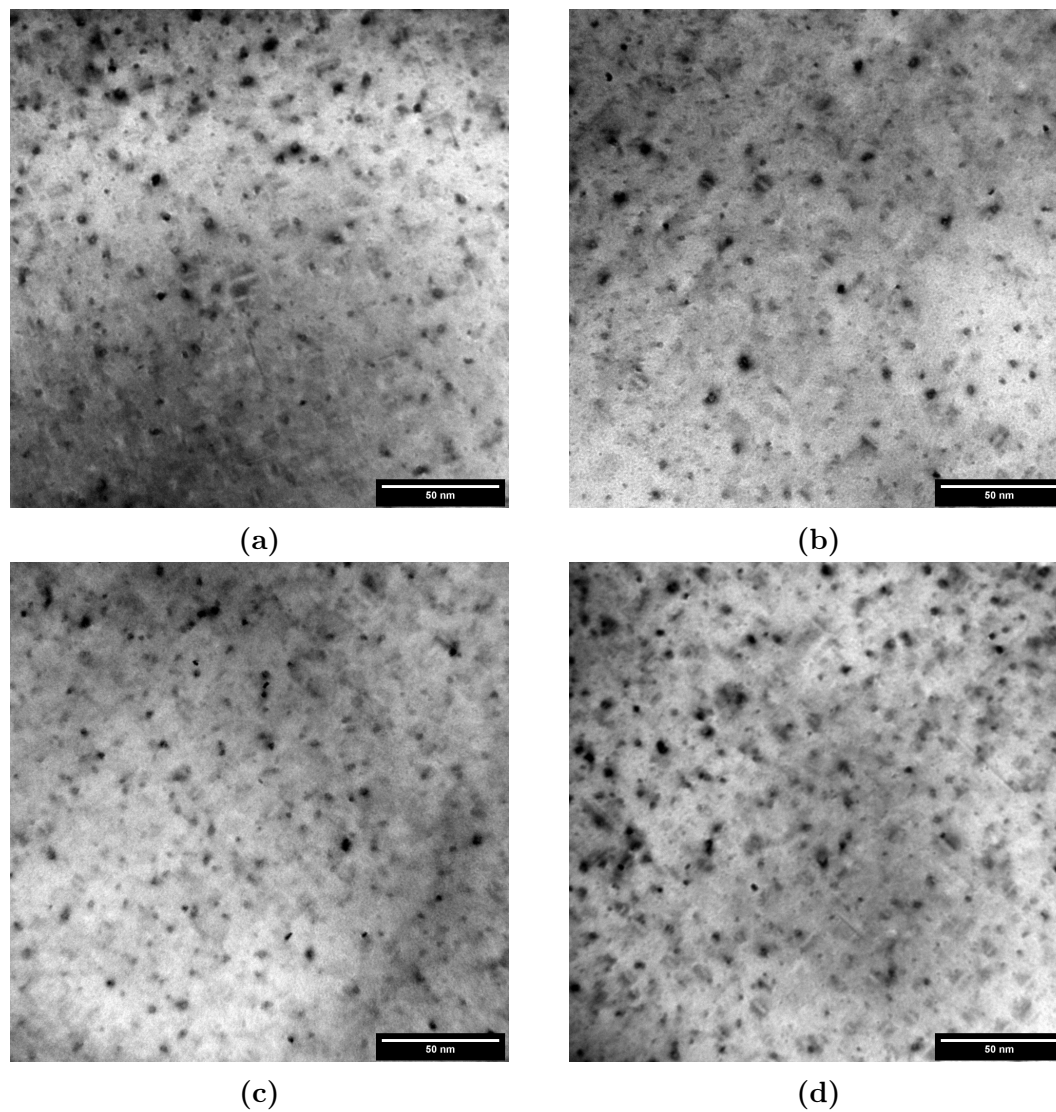
Figure 4.9: TEM images from sample series D, which was extracted at 4 mm distance from the EZ of the HYB-weld. The images shows that there is a large amount of small precipitates distributed in the matrix, at a comparable level to the reference material.
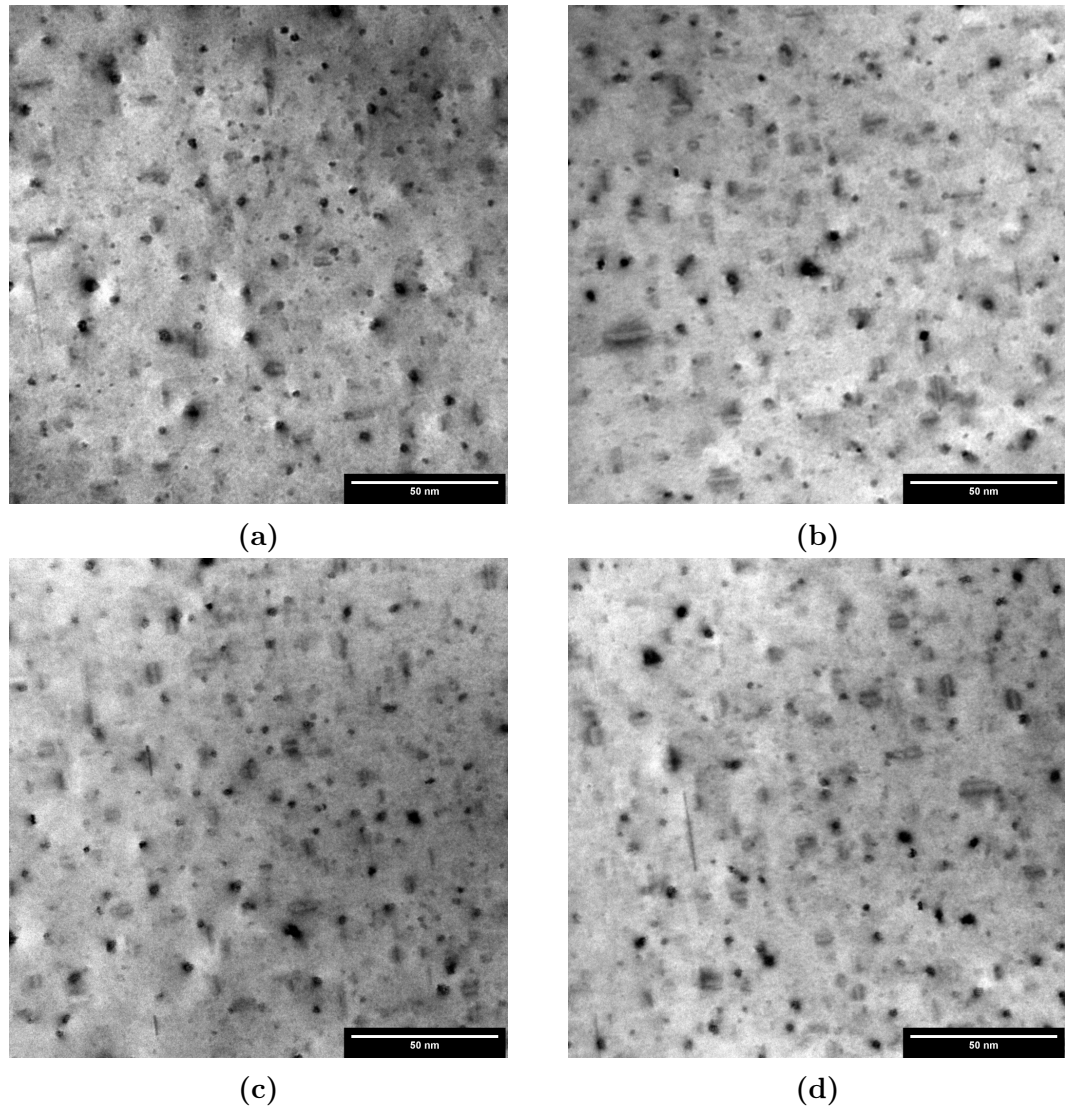
Figure 4.10: TEM images from sample series C, corresponding to a distance of 3 mm from the EZ of the HYB-weld. The images shows a slight increase in precipitate length and decrease in density when compared to the reference material.

(a)

(b)

(c)

(d)
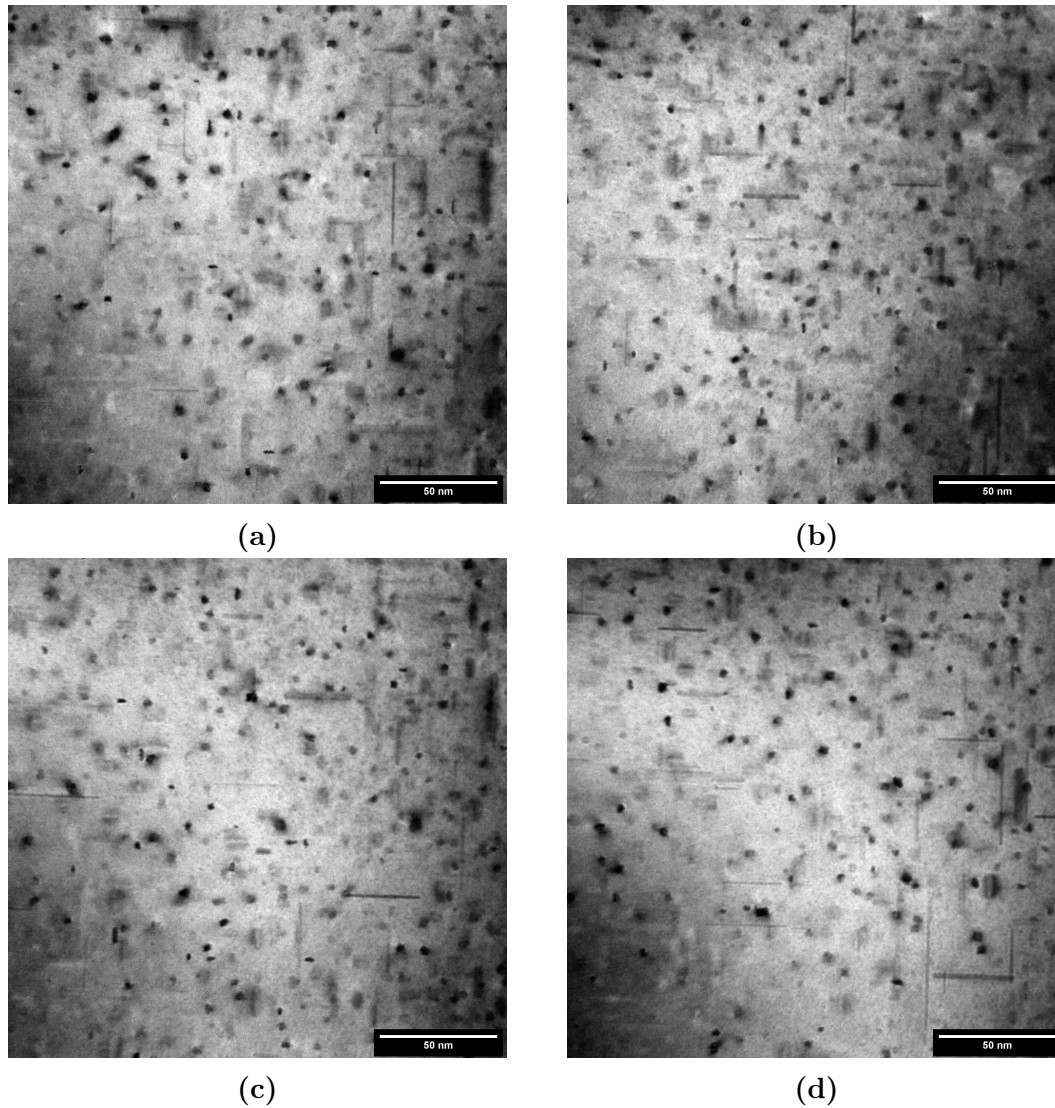
Figure 4.11: TEM images from sample series B, corresponding to a distance of 2 mm from the EZ of the HYB-weld. The images show a significant decrease in precipitate density and increase in precipitate length compared to the reference material.

(a)

(b)

(c)

(d)
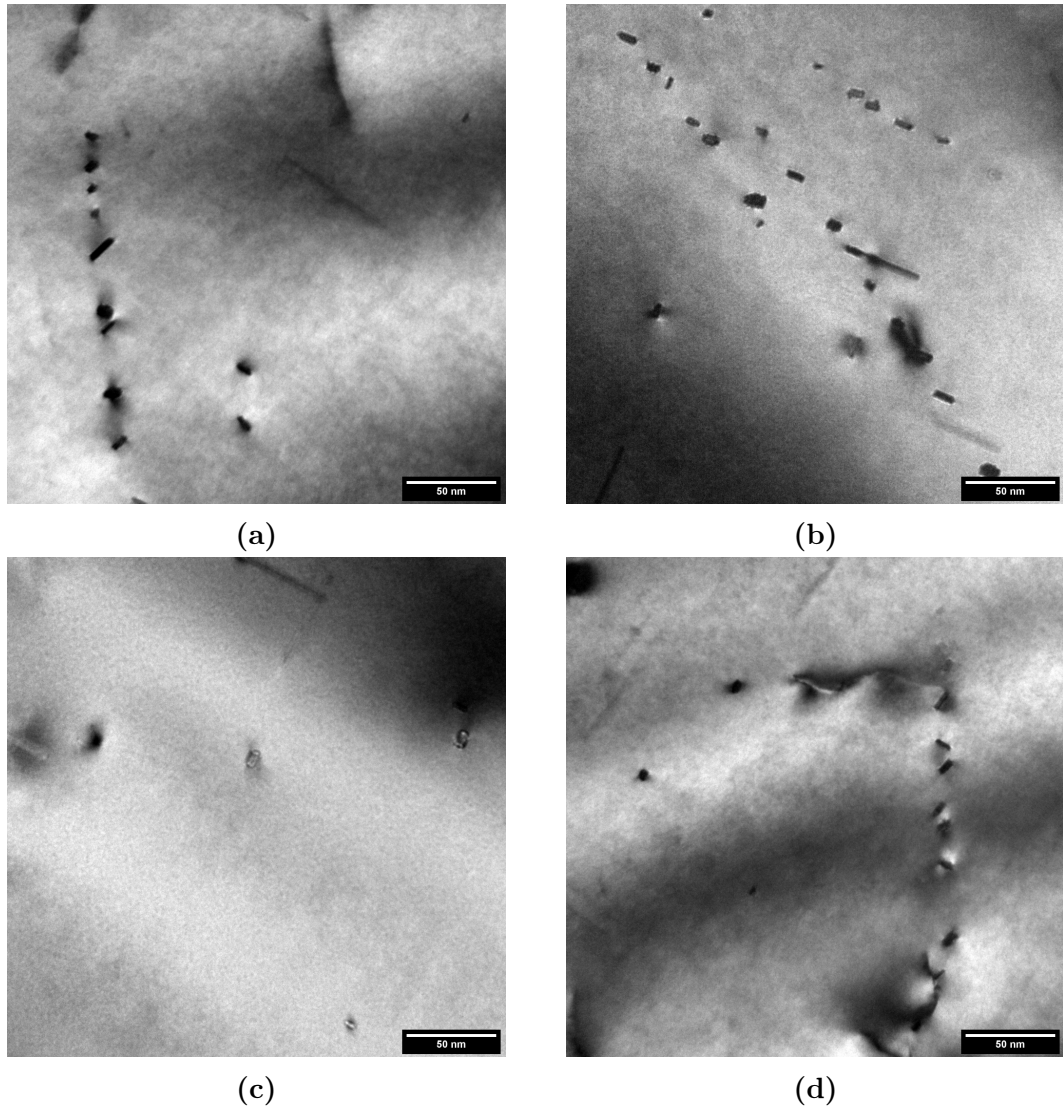
Figure 4.12: TEM images from sample series A, exttracted at a 1 mm distance from the EZ of the HYB-weld. The images show an almost complete dissolution of precipitates into the matrix.

4.3   SPED analysis

SPED scans were successfully preformed on samples B2, C3 and D4 using the scan parameters given in Table 3.3. The SPED data-sets were preprocessed to center the signal space on the $(0\,0\,0)$ spot. Additionally the signal space was binned to reduce the size of the signal space to 128×128 pixels from 256×256, reducing the size of the data-set by a factor of 4, in order to reduce the demand for computer memory during NMF-decomposition.

A range of different values for K was tried for NMF-decomposition, with the intention to find a value of K that yielded all diffraction patterns, without decomposing patterns into multiple factors. For the B2 scan K was set to 25, while for C3 and D4 K was set to 30.

After decomposition each factor was inspected and matched to the theoretical diffraction patterns of known phases. In sample D4, diffraction patterns corresponding to β'' and L phases was identified, while in sample C3 diffraction patterns corresponding to Q' was also found in addition to L and β''. Sample B2 yielded diffraction patterns corresponding to β'', L and β'_{Cu} when decomposing to 25 factors, additionally small amounts of Q' was found when decomposing to 40 factors. Examples of each phase identified is shown in Figure 4.13, a complete overview of the diffraction patterns identified is found in the appendix.
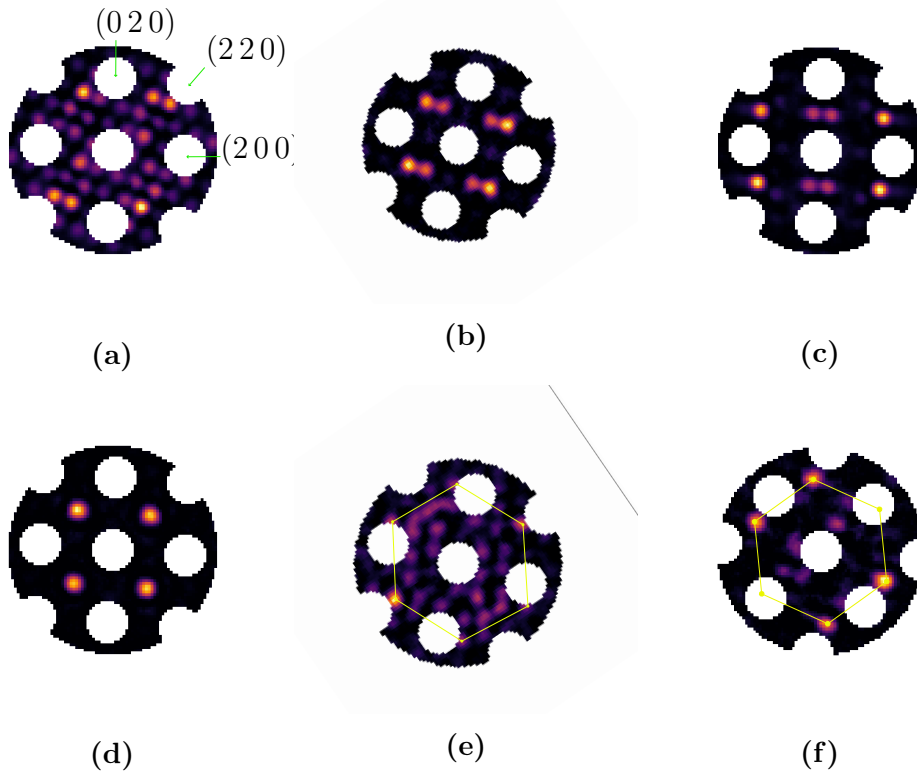
Figure 4.13: Diffraction patterns found from SPED decomposition. a) β'' b) β'' in-plane c) L d) Surface Cu e) β' f) Q'

The corresponding loadings for each phases was then used to make a phase map for each scan. For each identified phase an array of Boolean values was created, with the same size as the navigation space of the scan. For each factor

that was identified to belong to a phase, the corresponding loading was analyzed. If the loading value for a given point was found to be above a set threshold, then the value in the Boolean array with the same coordinates was set to True. The Boolean arrays were then used to create a colour map, which was combined with a virtual DF-image. The phase maps for D4, C3 and B2 is shown Figure 4.14, Figure 4.15 and Figure 4.16 respectively.
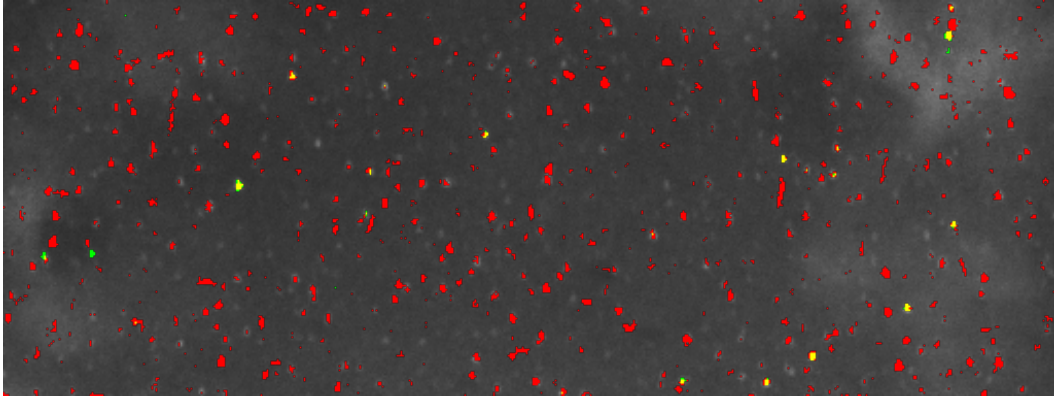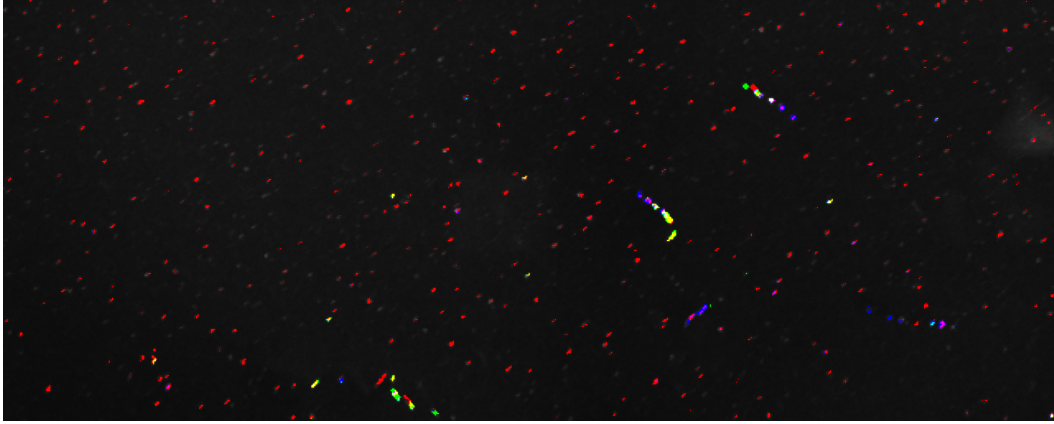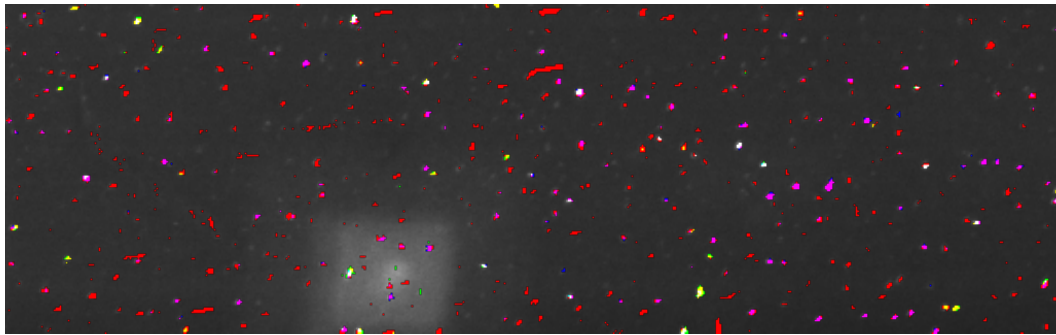

Figure 4.14: Phase map of scan D4, the map is created by combining loading maps generated by NMF-decomposition. These loading maps were filtered to only show signals above a set threshold, and then combined with other loading maps showing the same phase. These loadings were then used to create a rgb-colourmap where each colour was set to correspond to a phase, where red=β'' and green = L. Yellow indicates that both β'' and L was detected. The phase map is placed on top of a virtual DF image of the same area.

In all three scans, β'' was found to be the most abundant precipitate phase, with a smaller amount of L-phase precipitates. In scan C3 Q' was found primarily in areas with defects in the aluminium matrix, the same regions also had larger amounts of L-phase when compared to the rest of the sample, in B2 the small amounts of Q' detected were also found in regions with defects. The regions where β' was detected in B2 also gave signals for β'' in most cases.

There are precipitates in each sample that are visible in the virtual-DF that does not have a loading value above the set threshold for any of the identified phases, meaning that the phase is undetermined for these precipitates.

In Table 4.3 the percentage of each phase in the different scans is shown. The percentages were calculated by counting the number of points in navigation space where the loading for a given phase was above the set threshold and dividing by the number of points where any phase was above the threshold. In other words the percentages represents the are covered by each phase in the phase-maps, and not the numerical percentage of precipitates. Since β'' was the only phase detected in another orientation than along the optical zone axis, the signals from in-plane β'' precipitates are ignored, so that only precipitates extending in the $[1\,0\,0]$ direction are counted.

Figure 4.15: Phase map of scan D4, the map is created by combining loading maps generated by NMF-decomposition. These loading maps were filtered to only show signals above a set threshold, and then combined with other loading maps showing the same phase. These loadings were then used to create a rgb-colourmap where each colour was set to correspond to a phase, where red=β'', green = L and blue = Q'. other colours indicate regions where multiple phases was detected, where the colour is given by the combination of the detected phases' rgb values. The phase map is placed on top of a virtual DF image of the same area..

Table 4.3: Fraction of phases detected in the SPED scans, all numbers are given in percentage. The Q'/β'_{Cu} is to be interpreted as Q' in C3 and β'_{Cu} in B2, the small amount of Q' detected in B2 is not included.

Phases	B2	C3	D4
β''	67.93	79.48	95.93
Q'/β'_{Cu}	2.88	4.58	-
L	2.616	4.87	1.21
β'' + Q'/β'_{Cu}	17.95	2.97	-
β'' + L	4.47	6.18	2.86
L + Q'/β'_{Cu}	0.14	0.83	-
β'' + L + Q'/β'_{Cu}	4.01	1.07	-

Figure 4.16: Phase map of scan D4, the map is created by combining loading maps generated by NMF-decomposition. These loading maps were filtered to only show signals above a set threshold, and then combined with other loading maps showing the same phase. These loadings were then used to create a rgb-colourmap where each colour was set to correspond to a phase, where red=β'', green = L and blue = β'. other colours indicate regions where multiple phases was detected, where the colour is given by the combination of the detected phases' rgb values. The phase map is placed on top of a virtual DF image of the same area. The small amounts of Q' detected is not shown.

FIVE

DISCUSSION

5.1 Accuracy in sample preparation

As seen in the previous chapter, the mechanical properties and microstructure changes significantly over short distances in the HAZ. This is especially true in the regions close to the EZ interface, as seen in the difference in precipitate structure from 1 mm to 2 mm distance from the EZ/HAZ. As such it is important to have a high degree of accuracy when extracting the samples from the bulk material. Prior to electropolishing the samples had a thickness of around $100\,\mu m$, the edge of the hole produced by electropolishing will usually be close to the center, but may vary within this thickness. As such the lower limit for accuracy of distance from the EZ/HAZ interface will be determined by the thickness of the sample prior to electropolishing. The real accuracy will however be determined by the steps before electropolishing. In particular the inaccuracy resulting from the use of the high speed saw will be high unless carefully executed.

The strategy utilized to maximize accuracy was to first saw off pieces such that the edge of the sample was as close to the region of interest as possible without cutting into it. The outer edge was then marked with a waterproof marker to keep track of orientation of the sample later. Another cut was then made on the other side of the region of interest, overshooting by a significant amount. When the sample strip was later thinned down by mechanical grinding, the majority of the thinning was done on the inner edge of the strip, while the outer edge was polished by the minimum required to achieve a smooth surface. With this strategy it was possible to extract the samples with an estimated accuracy of a couple hundred microns.

Each sample series was extracted from a single sawed and polished strip, meaning that the error in distance from the EZ is the same for every sample for a given series.

5.2 Hardness and temperature

As mentioned in the last chapter, the width of the HAZ on the AS is about 4-5 mm. Looking at the temperature profiles in Figure 4.2 and the maximum temperatures reached in Figure 4.3, it seems that a reduction in hardness starts to occur above

some critical temperature somewhere in the range of 300-400°C. Suggesting that some reaction becomes significant above this temperature. It has been shown by Sunde et al. [19] that significant changes in precipitate structure can occur in the M-alloy at temperatures significantly lower than this, with a large amount of precipitates dissolving at temperatures around 200°C. However, in the study by Sunde the elevated temperature was held for a significantly longer time than that of the samples in the HAZ, and it is known that the time the temperature is kept at an elevated level is an important factor[24]. This suggests that changes in the precipitate structure might take place below the critical temperature, but that the reaction rate is too slow to cause any significant changes in mechanical properties before the temperature decreases back to room temperature.

One possible estimation for the critical temperature threshold observed is the solvus temperature of β''-precipitates, where the solubility of Mg and Si in the material will be greater than what is present in the alloy at large. Above the solvus temperature it is possible for all β''-precipitates to dissolve without the need for any secondary mechanisms such as phase-transitions or solute migration to grain-boundaries. In a study by Vasilyev et al. from 2011 [44] a formula for the solvus temperature of β'' ($T_{s,\beta''}$) as a function of total alloy concentration of Mg (C_{Mg}) and Si (C_{Si}) was found to be:

$$T_{s,\beta''} = \frac{Q}{S - ln(C_{Mg}C_{Si})}(K) \tag{5.1}$$

Where Q and S are empirical parameters, which in the same study was found to be $S = 5.777$ and $Q(x) = -1525.17x^2 + 51.43x + 3847.47$, where $x = C_{Mg} - C_{Si}$. Figure 5.2 shows a calculated solvus line of β'', assuming a constant ratio of Mg and Si. Inserting the Mg and Si concentration of the M-alloy into Equation 5.1 yields a $T_{s,\beta''}$ of 324°C. This model does however not take the effect of Cu additions into consideration, which could have an effect on the solvus temperature. The temperature outside of the HAZ never goes above the calculated solvus line, as seen in Figure 5.1

According to the temperature simulations, the temperature reached in the HAZ is well above the calculated β'' solvus temperature at its maximum. Which would suggest that all β'' precipitates would dissolve if equilibrium[1] is reached. The temperature in the HAZ is shown to have a sharp increase during the welding process, followed by a gradual decrease in temperature, causing the equilibrium solubility of Mg and Si to change throughout the entire temperature cycle. As the temperature increases the β''-precipitates will begin to dissolve, releasing Mg and Si into the aluminium matrix. It should be noted that other reactions, such as phase transitions may occur simultaneously. As concentration of Mg and Si around the β'' precipitate increases, the reverse reaction where Mg and Si solutes contributes to growth on the β'' particle may also occur.

$$\mathrm{Mg_5Si_6(s)} \rightleftharpoons 5\,\mathrm{Mg(sln)} + 6\,\mathrm{Si(sln)} \tag{5.2}$$
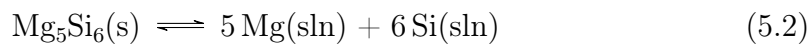
As a result of this two-way reaction the local concentration of Mg and Si along the precipitate-matrix interface may not on average exceed the equilibrium solubility for a given temperature, although some local deviations will occur. Therefore

---

[1] Equilibrium condition for the dissolution of β'', phase transitions to more thermally stable phases may also occur.
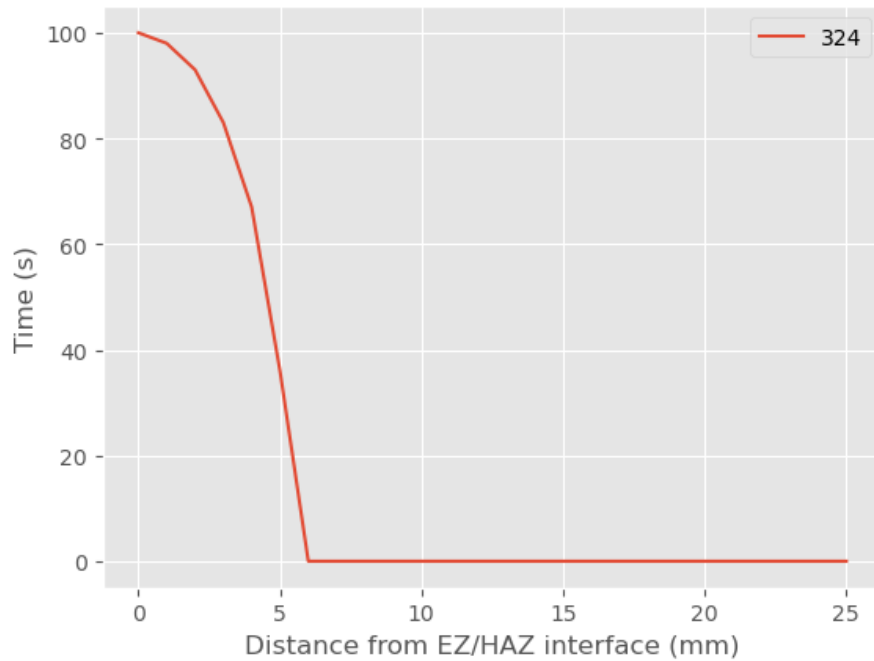
Figure 5.1: Graph of the time spent above the calculated solvus temperature of β'' (324°C) as a function of distance from the EZ/HAZ interface. The temperature never goes above the solvus temperature at distances past 5 mm, which coincides with the extent of the HAZ.
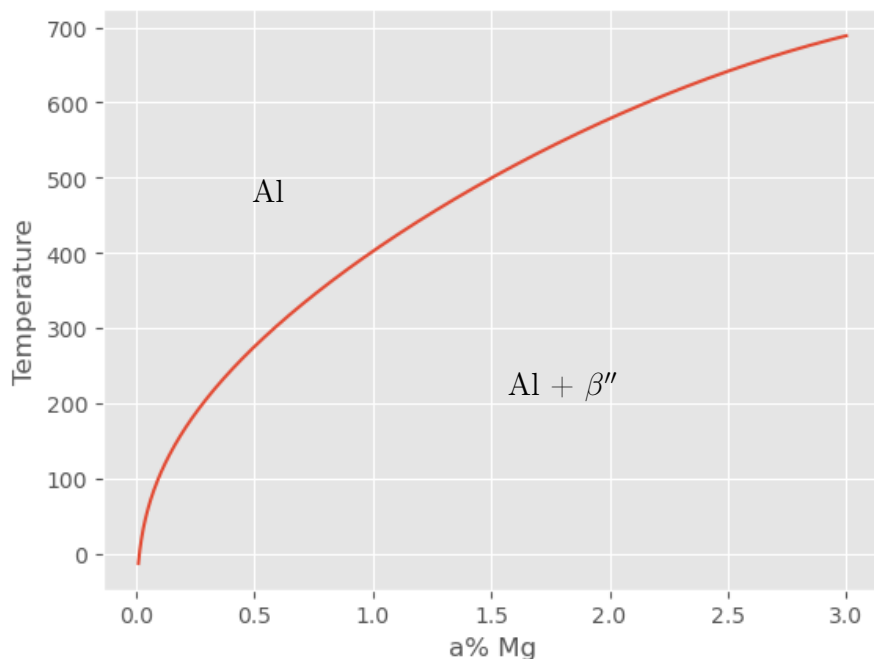

Figure 5.2: Simplified phase diagram showing the solvus line for the β''-phase, calculated using Equation 5.1. The ratio between Mg and Si has been set to a constant 5:6. Other reactions such as possible phase transformations are not included in the phase diagram.

the dissolved Si and Mg atoms must diffuse away from the precipitates to allow
further dissolution of the β''-precipitates, an illustration of the solute concentration
around the precipitates a short time after the temperature is increased is
shown in Figure 5.3. This results in the left to right reaction rate in Equation 5.2
to be limited by the rate Si and Mg are able to diffuse away into the aluminium
matrix, which is determined by Fick's second law. The diffusion rate of Mg and
Si in aluminium will increase with temperature, since the diffusion constant D
in Fick's law is dependant on temperature. Assuming the Arrhenius relation is
valid for Mg and Si in aluminium, and inserting this relation for the diffusion con-
stant D in Fick's second law gives the following differential equation describing
the diffusion:

$$\frac{\partial \phi}{\partial t} = D_0 \exp\left(\frac{-\Delta H}{k_b T(t)}\right)\nabla^2 \phi \tag{5.3}$$

With the large changes in temperature observed, this differential equation not
possible to solve analytically, and quite daunting to solve numerically. As such no
efforts were put into trying to calculate a complete diffusion process. Estimating
some of the parameters that govern the diffusion process is however a much simpler
task. Namely the diffusion constant D, and the boundary condition $\phi(0,t)$, which
is given by the surface concentration of the precipitates.

Using the Arrhenius relation it is possible to estimate the difference in the
diffusion coefficient as a function of time at different regions of the HAZ. The
value of ΔH can be estimated using a method described by Korablev [45]. For the
purpose of comparison of D at different distances form the EZ/HAZ interface, it
would be sufficient to calculate the relation D/D_0. This can be done by inserting
the calculated temperature profiles into:

$$\frac{D}{D_0} = \exp\left(\frac{-\Delta H}{k_b T(t)}\right) \tag{5.4}$$

The result of this calculation is shown in Figure 5.4.

Using Equation 5.1, the surface concentration in the precipitate-matrix inter-
face can be calculated. Assuming the ratio between Mg and Si at the surface
is 5:6, similar to the suggested composition of β'' (Mg_5Si_6), and that the surface
concentration is always equal to the solubility limit for a given temperature, the
surface concentration at the precipitates through the thermal cycle can be found.
The results of this calculation within the HAZ is shown in Figure 5.5.

As the temperature is gradually reduced the solubility of the Mg and Si in the
matrix is also reduced. If the solubility drops faster than the atoms are able to
diffuse away, the local concentration of solutes around the precipitate will reach
supersaturation. This will cause the right to left reaction in Equation 5.2 to
become dominant, and the precipitates will act as a net drain of Mg and Si solutes
instead of a net-source.

The diffusion rate of Si and Mg is therefore reduced in two ways as temperature
is reduced. The first is a reduction in the diffusion constant D, which reduces
the diffusion rate for a given concentration gradient. And a reduction in solute
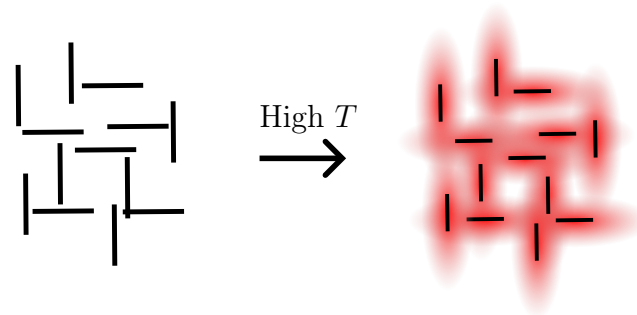concentration around the precipitate, reducing the boundary condition $\phi(0,t)$.

Figure 5.3: 2D-illustration of the concentration gradient of solutes around precipitates. (left) β''-precipitates in aluminium at room temperature. (right) Partially dissolved β''-precipitates shortly after raising the temperature. As the dissolved Mg and Si atoms have not had time to diffuse to an even distribution in the aluminium matrix, a concentration gradient with its maximum at the interfaces between the precipitates is created. This gradient is illustrated with a colour gradient where red areas have a higher concentration of Mg and Si.
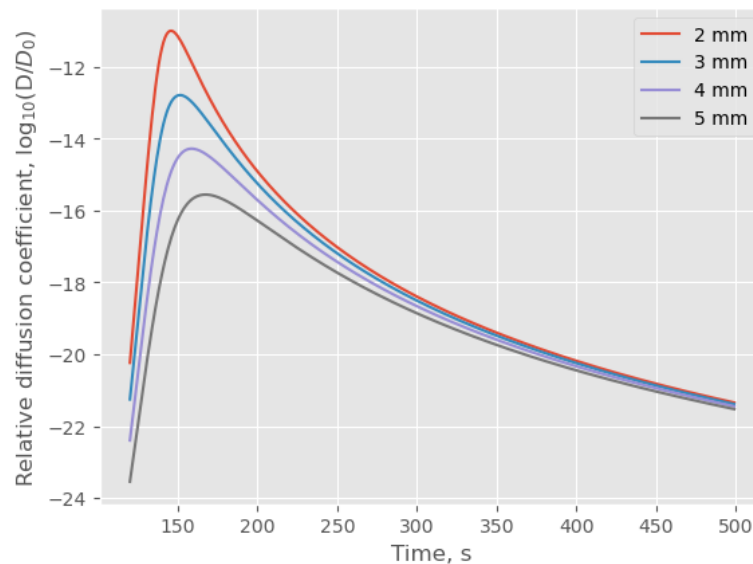
Figure 5.4: Calculated relative diffusion coefficient D/D_0 for Mg in Al as a function of time at different distances from the EZ/HAZ interface, shown on a logarithmic scale. The value for D/D_0 is calculated with the assumption that the Arrhenius relation is valid for Mg in Al.
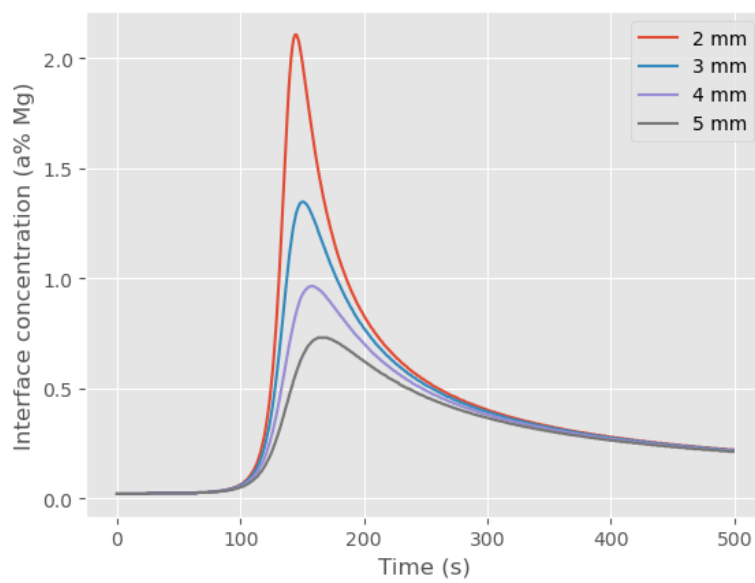
Figure 5.5: Calculated surface concentration of Mg around precipitates as a function of time at different distances from the weld, which corresponds to the boundary condition $\phi(0, t)$ in Equation 5.3. The concentration of Mg is found by assuming a 5:6 ratio of Mg to Si.

5.3 Precipitate statistics

5.3.1 Regarding the statistic method

The measurements of length and cross-section, as well as the counting of precipitates for numerical density calculation was done manually through human inspection and the ImageJ software. Utilizing human inspection have both its advantages and its drawbacks compared to using computer based approaches. During manual counting each precipitate is individually evaluated for orientation and size, which results in every feature in the image being evaluated as to whether it shows a precipitate, or if the feature comes from a defect, GP-zone or some other artifact in the image. It does however introduce a systematic error from the biases the interpreter exercises when evaluating the features in the image. The results may therefore vary based upon who interprets the images, in particular with regards to precipitate density since every feature in a given region must be evaluated as to whether it shows a precipitate, whereas for length and cross section measurements dubious or unclear features can be ignored. If all the measurements are performed in a similar way, and by the same interpreter, the bias exercised will be similar for all samples, and makes it possible to evaluate trends in the statistics. It does however make it difficult to compare the results to those gathered by a different interpreter. Manual inspection can also be quite time-consuming, especially if the density of precipitates is high, which puts a soft limitation on the amount of data-points that can be gathered if time usage is a factor.

A computer based approach for counting and measuring precipitates would have eliminated the bias from human interpretation of the images, and would have made the evaluation of each feature more consistent, and independent of the user. The process of developing a program that is able to accurately evaluate features in a TEM image could however be quite time-consuming, but would make it much faster to analyze images once developed, and allow for the collection of a large statistical basis in a short time. There is still some human bias involved in this process, as the parameters used by the program must be set by the programmer. Due to the uncertainty in the time needed to develop a satisfying application for precipitate analysis, it was determined that a computer based approach would not be pursued.

In order to get accurate statistics it is important that the TEM images have a sufficiently high resolution, so that the smallest features in the images can be properly evaluated. For the most part a high enough resolution was achieved to be able to evaluate all features in the BF images. There was however some suboptimal images used for the analysis of the reference series, as there was a lack of good images of this series. This was mostly due to inexperience on the hand of the operator (the author), as most of these images were captured and analyzed at an early stage. In hindsight these samples should have been reinspected.

As mentioned in the theory section it may be necessary to adjust the measured average length according to geometrical consideration, however it is not always the case. The adjustment as given in Equation 2.37 will be dependent on the ratio between the precipitate length and sample thickness (l_m/t), and the total sample tilt Θ. The relative adjustment of length will be greater the longer the precipitates are in relation to the thickness, and the higher the sample tilt is. For

all the measurements performed the total tilt was always less than 15°, and with the exception of sample series A, the length to thickness ratio was around 1:10 or less. Inserting these values into Equation 2.37 yields a relative adjustment of just a few percent.

The BF images used for precipitate statistics had a digital resolution of 2048×2048 pixels, which corresponded to areas between 212×212 and 169×169 nm[22]. Which corresponds to a distance of 0.1 nm between each pixel, which is around the same amount the precipitate lengths in sample series B, C and D would have to be adjusted by. Meaning that the adjustment would be around the same size as the limitations of accuracy given by the data-set, ignoring any other limitations in accuracy of the measurements such as the real space resolution achieved or the uncertainty from the interpreters definition of the precipitates extent. Because of this it was determined that a geometrical adjustment of the length would only contribute a negligible amount, and was therefore not performed on sample series B, C and D.

In sample series A, extracted at a 1 mm distance from the weld, there were found very few precipitates compared to the other series. In series B, C and D, all regions had a large amount of precipitates, making any image captured from regions with the right orientation and thickness suitable for statistical analysis. While in series A it was difficult to obtain images that showed more than a couple precipitates, with some regions having close to zero precipitates. As a result the images captured from the A samples have a strong bias towards showing regions with a relatively high amount of precipitates. As such any estimation of numerical density in these sample would be heavily influenced by this bias, and would not yield an accurate result. It is however clear that the density of precipitates is much lower in this region compared to regions further from the weld, and was set close to zero in the graph in Figure 4.6.

5.3.2   Changes in precipitate size and density

As shown in Table 4.1, there are two clear trends that come from the statistical investigation of the different regions of the HAZ. The first being that precipitates in regions close to the EZ are on average longer and have a larger cross-section, compared to those in regions further away. The second is that the density of precipitates are greatly reduced in the regions close to the weld when compared to regions further away.

The reduction in density close to the EZ could be explained by the increase in the interface concentration of solutes around the precipitates and the exponential increase of the diffusivity constant as the temperature increases. It has been shown in Figure 4.3 that the maximum temperature reached is above the calculated solvus temperature for β'' through the entire HAZ. However, while the maximum temperature reached is high enough to cause complete dissolution of β'' precipitates, the time spent above this temperature is less than 100 seconds at all points in the HAZ, as is shown in Figure 5.1. Meaning that there is very limited time for the precipitates to dissolve, and will only dissolve completely if the reaction rate of dissolution is sufficiently high.

---

[2] The BF images were taken using different levels of magnification, and as such there are some variations in the area covered by each image.

With the assumption that the dissolution-reaction has a diffusion-limited reaction rate, the parameters D and $\phi(0,t)$ will be what determines the reaction rate. As is illustrated in Figure 5.5 and Figure 5.4 these parameters vary a great amount within the HAZ. From 5 mm to 3 mm the maximum value of $\phi(0,t)$ is almost doubled. While the diffusion constant D follows a exponential relationship with temperature, and is calculated to vary with some orders of magnitude within the HAZ, increasing by approximately $1000\times$ at its maximum from 5 mm distance to 3 mm. Which suggests that the dissolution reaction rate also varies with some orders of magnitude within the HAZ.

As is evident by the large amount of β'' precipitates still present in series B, C and D, there is not sufficient time with their respective reaction rates to achieve a complete dissolution of all precipitates at distances further from the EZ than 2 mm. The reaction rate is however fast enough to allow a portion of the precipitates to dissolve, explaining the reduction in precipitate density.

The increase in length of precipitates close to the EZ could be explained by a couple of different mechanisms, which are all related to the dissolution of precipitates described above. The mechanisms are also not mutually exclusive, hence a combination of the mechanisms might occur.

The first explanation is that the precipitates are lengthened through reprecipitation after dissolution. As the temperature decreases amount of Mg and Si dissolved will reach a supersaturated level since the solubility decreases with temperature, and the solutes will reprecipitate if possible. Since there is an energy barrier associated with forming a precipitate, as described by Equation 2.4, it is energetically favourable for the solutes to instead contribute to growth of existing precipitates. However, since some of the precipitates are completely dissolved, and assuming the amount of solutes in the matrix is comparable before and after the welding, then the average amount of solutes reprecipitating onto a surviving precipitate is greater than the amount that was initially dissolved from this precipitate. Hence the average length is increased. This mechanism is illustrated in Figure 5.6

The increase in length could also be explained by a survivor bias of longer precipitates. Longer precipitates have more Mg and Si that need to dissolve, and therefore more solutes that have to diffuse away from the precipitate. This results in a longer reaction time for a complete dissolution. Since the β'' precipitates primarily grow along the $\langle 1\,0\,0 \rangle$ directions in aluminium, it can also be expected that primary interface for dissolution will be the corresponding $\{1\,0\,0\}$-planes. If this is the case then the expected time for a complete dissolution of a precipitate will be a function of the precipitates initial length.

It has so far been assumed that the interface concentration is the same for all precipitates. It is however known that smaller particles in general have a higher solubility than larger particles, due to the Gibbs-Thompson effect [7]. This would also apply to the precipitate particles in the aluminium matrix, which would suggest that the interface concentration will be greater for smaller precipitates. And when setting the boundary condition $\phi(0,t)$ equal to the interface concentration this results in a steeper concentration gradient surrounding the smaller precipitates.

Additionally it is possible with a survivor bias of precipitates of other phases than β''. Both L and post-β'' phases like Q' and β' exhibit a higher resistance to
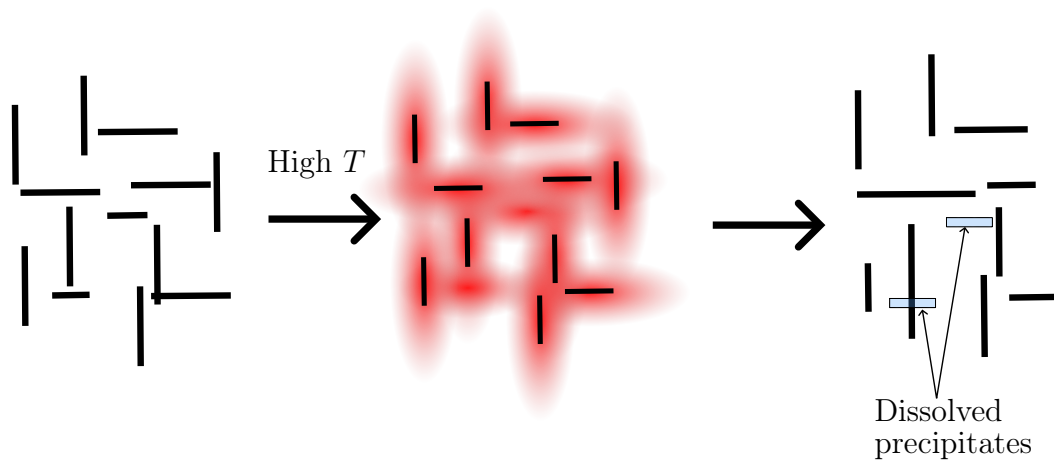
Figure 5.6: Illustration of precipitates dissolving and reprecipitating due to an increase in temperature, followed by a gradual decrease back to room temperature. Some of the precipitates dissolve completely when exposed to high temperatures, while others dissolve only partially. As temperature decreases the solutes reach a supersaturated level and reprecipitates onto the surviving precipitates, causing a lengthening in the surviving precipitates.

temperature increases than β''. If the initial length of the other phases were longer than that of β'', then a reduction of β'' precipitates would increase the average length.

As mentioned, the suggested mechanisms for precipitate lengthening are not mutually exclusive, and it seems likely that the reality is some combined reaction. It is for example not difficult to imagine that the short precipitates are the first to dissolve, and that solutes from these reprecipitates onto the surviving long precipitates. During reprecipitation it should also be possible for the solutes to reprecipitate onto a precipitate with a different phase than its origin.

5.3.3   Observations on the microstructure close to the HAZ

The average length of precipitates in sample series A was found to be 28.52 nm, however the length distribution shown in Figure 4.7a show that very few precipitates have a length close to the average. The distribution show a peak of precipitates with length of less than 10 nm, followed by a gap in the range 20-30 nm, and a second peak in the distribution centered in the range 50-60 nm. This two peak distribution would suggest that there are precipitates of at least two types in these samples. One possible explanation is that the two peaks represent different phases, which have reacted differently to the temperature increase in the HAZ. Since SPED was not performed on this series it was not possible to conclude whether or not this is the case, there are however some indications from the BF TEM images that could suggest that this is the case based on the morphology of the precipitates, as shown in Figure 5.7.

Another possible explanation is given by the positioning of the precipitates in these samples. As shown in some of the images in Figure 4.12, the shorter precipitates in series A have a tendency to line up instead of being randomly dis-
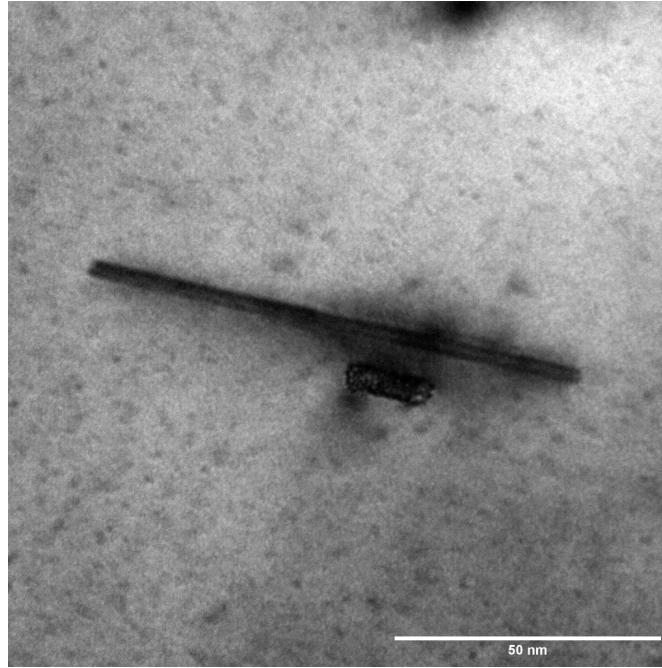
Figure 5.7: BF TEM from sample A2, showing two precipitates with different lengths in sample A2. The top precipitate has a length of 93 nm and shows the characteristic double strain associated with β'' phase. The bottom precipitate has a length of 15 nm and does not show a double strain, which could indicate that the precipitate is of some other phase than β''.

tributed throughout the material, possibly along dislocation lines. At dislocation lines the rate of diffusion of solutes and the nucleation rate of precipitates are greatly increased [46], it could therefore be possible that new precipitates are able to form at the dislocation lines. This explains the two peak distribution as a size difference between the pre-existing precipitates that have grown by reprecipitation of solutes, and the new precipitates that have nucleated and grown along the dislocation lines.

It is important to note that these two explanations are not mutually exclusive, and a combination of both processes may have occured. In a study by Teichmann et al.[47] it was shown the introduction of deformation prior to artificial ageing results in precipitation being restricted primarily to the deformation lines, and that these precipitates largely will be of post β'' phases. It is therefore expected that any pre-existing precipitates along deformation lines should be of a different phase than β'', which is the primary phase of precipitates in non-deformed bulk.

The dislocation line precipitate phenomenon was also observed in one BF image from the reference series, the image is shown in Figure 5.8. Isolating the short precipitates in series A yields an average length of these precipitates of 9.01 nm, which is slightly longer than the dislocation line precipitates seen in the image from the reference series, which was 6.48 nm. Which could indicate that these precipitates also have grown in size as a result of the heat treatment. However, as the average from the reference series is taken from just a single image, the statistical background is not solid enough to make any definite conclusions.

In series A it is evident from the lack of precipitates that the majority of β'' precipitates have been dissolved while the material was subjected to high tem-
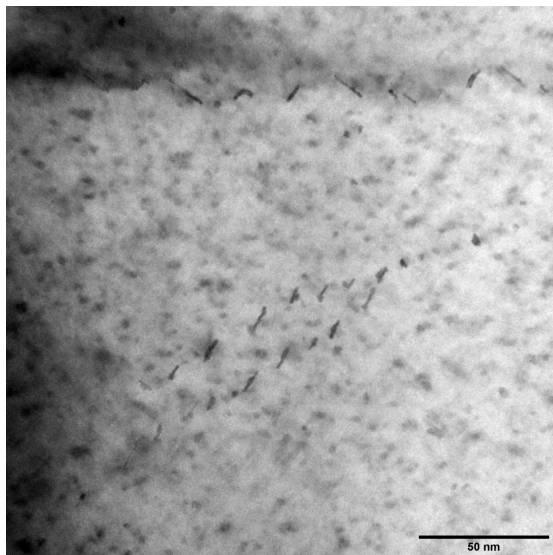
Figure 5.8: BF image of a reference sample with high contrast precipitates along deformation lines. The difference in contrast could suggest that the precipitates along the deformation line is of another phase than the precipitates in the matrix.

perature. As the temperature drops the amount of Mg and Si dissolved in the aluminium matrix will reach a supersaturated level, and reprecipitation onto surviving precipitates may occur. However, since most of the precipitates are no longer present, the dissolved Mg and Si are not able to reprecipitate onto existing precipitates, which leaves the aluminium in a supersaturated state. Due to natural ageing the supersaturated state is eventually resolved, as solutes eventually precipitates out as GP-zones. These GP zones are visible in the TEM images at high magnification, as is shown in Figure 5.9.
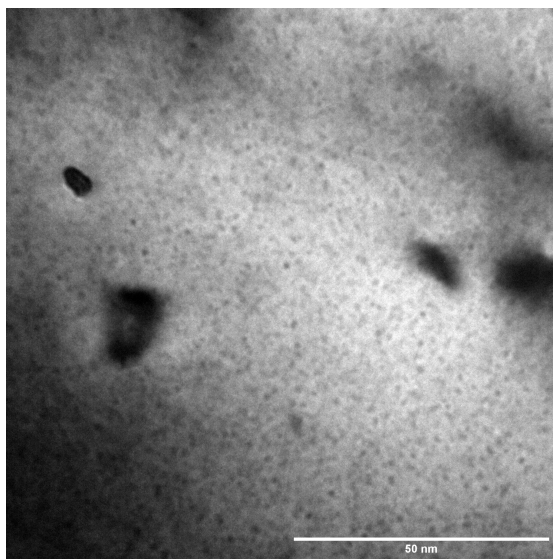
Figure 5.9: BF TEM image from sample A2, showing a large amount of GP zones within the aluminum matrix.

5.4   Phase analysis using SPED

5.4.1   Decomposition and masking

Selecting the ideal number of components for NMF decomposition of the SPED data-sets is not necessarily trivial. Selecting too high a number will result in a over-decomposition of the signals, making it difficult to evaluate what phase a given factor corresponds to. If the number of components are too low there is a risk of the NMF algorithm not being able to pick up certain weak and/or uncommon signals. Unfortunately it is not always the case that it is possible to find a value for K that avoids both of these problems, which was the case for sample B2. The selected value for K here was 25, at which point the factors already showed signs of over-decomposition, as is shown in Figure 5.10. During decomposition 5 factors was identified as β'' extending in the $[1\,0\,0]$ direction of aluminium, while a perfect decomposition would only yield 4. Despite of this the Q'-phase was not revealed when decomposing into 25 components, and a decomposition into 40 components was necessary to reveal this phase, decomposing into this many phases did however make it difficult to interpret other signals due to over-decomposition. Over-decomposing scan D4 also revealed the presence of Q' in 1 single precipitate
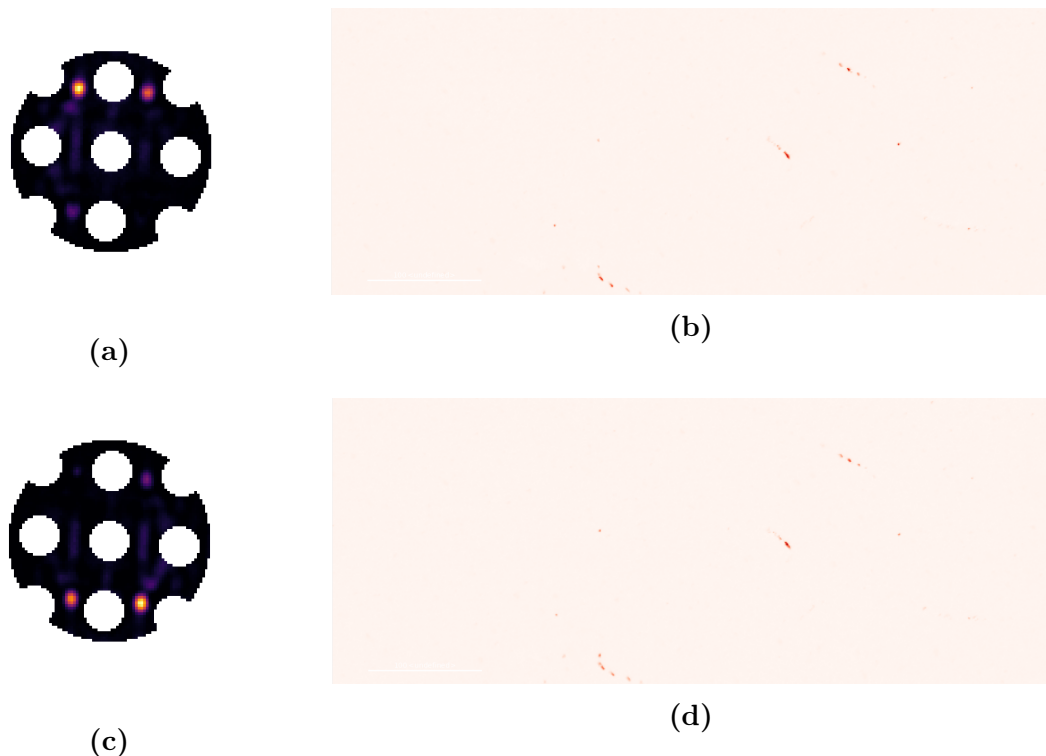
Figure 5.10: Example of over-decomposed signal from scan C3, (a) and (c) are two halves of the same signal that together constitute a L-phase diffraction pattern. (b) and (d) are the corresponding loading maps of the signals, and are as expected similar to one another

The diffraction pattern from the aluminium matrix gives a much stronger signal than that of the precipitate phases, which is one of the reasons it is necessary to mask out these signals before decomposition. Another reason is that the diffraction

pattern from aluminium is in this case of no interest other than as a reference to orientation, as it provides no new information about the nanostructure. The masking does however come with some drawbacks as it is necessary to extend the mask over each reflection by significant amount to fully mask the Al spots for all signals. if this is not done, then a large portion of the factors from NMF-decomposition will only show noise surrounding aluminium reflections. Masking out a large area will make the algorithm focus more on the diffraction patterns from precipitates. Making the masks large may however also mask out reflections from the precipitates, and make it harder to identify phases.

During decomposition the mask used for data-set D4 masked out a smaller percentage of the area within the $[0\,2\,2]$ radius compared to those used for B2 and C3. The main difference between these two data-sets and D4 was that D4 used a camera length of 16 cm, compared to 12 cm for B2 and C3. This also had the benefit that the reciprocal space showed in each signal was smaller and more focused on the region of interest. Which suggests that using a camera length of 16 cm was likely a slightly better option with the masking strategy used, although using a camera-length of 12 cm did not cause any major issues.
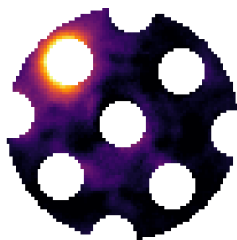
Figure 5.11: Decomposition factor showing a large amount of noise around the masked out $[0\,2\,0]$ reflection.

5.4.2 Setting thresholds for loading maps

In an ideal decomposition the loading maps for a given precipitate phase would show a loading value of zero in all points where there is no precipitate in the sample of this phase. However, due to background noise in the signal recorded, most points will wrongfully interpret the signal as if it contains a weak contribution from every factor, including precipitate phases that are not present. Hence in order to construct a meaningful phase-map it is necessary to find a suitable threshold value that separates the strong signals from precipitates and the weak signals that stem from a wrongful interpretation of background noise.

Setting this threshold would be simple if there was a clear difference in the signal strength of the precipitate diffraction patterns and the background noise. This is however not always the case, as is seen in Figure 5.12 where two diffraction patterns are shown, one of which is too weak to have been picked up at the threshold set during phase-map creation. In these cases it is unfortunately not

possible to pick up all precipitates while simultaneously avoiding noise signals, and some signal loss must be expected.
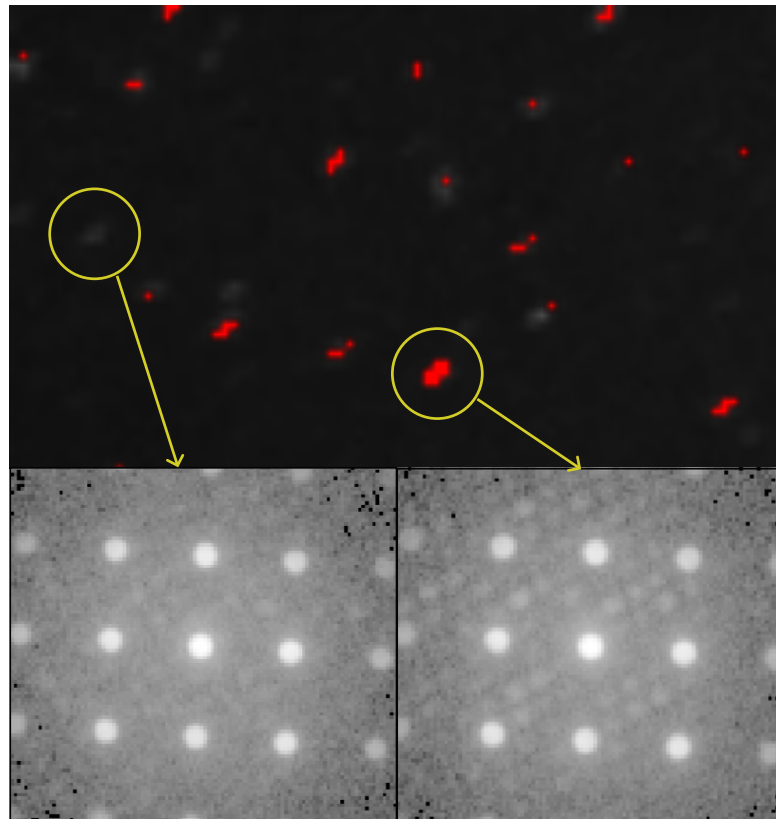
Figure 5.12: Focused image of a small section of phase map C3, highlighting two precipitates visible in the virtual DF, where one is identified as a β'' precipitate (right) and the other is not identified (left). The bottom images shows the signal detected in reciprocal space at the two position. The bottom right image shows a strong signal from a β'' precipitate, while the signal in the left image shows a weak signal signal from an unknown precipitate that is barely distinguishable from the background noise.

The thresholds in the phase maps were set to be a percentage of the maximum values present in each loading. In Figure 5.13 the distribution of loading values as a percentage of the maximum value in each loading map is shown, it can be seen as the threshold increases the number of signals above the threshold decreases rapidly in the begining before flattening out. One method that was tried to optimize the threshold, was to set the threshold to the minimal distance between the origin and the curve, this method did however still pick up a lot of noise. At this point the curve is still still in the process of flattening out, and it was found that a slight increase to where the curve has flattened out removed the remaining noise. It was observed that the origin minimization gave a threshold of around 6-10% for precipitates with orientation along the optical axis, and around 15-20% for in-plane precipitates. The thresholds were therefore set at 15% β'', L, Q' and β'_{cu} signals, and 25% for in-plane β'' signals.
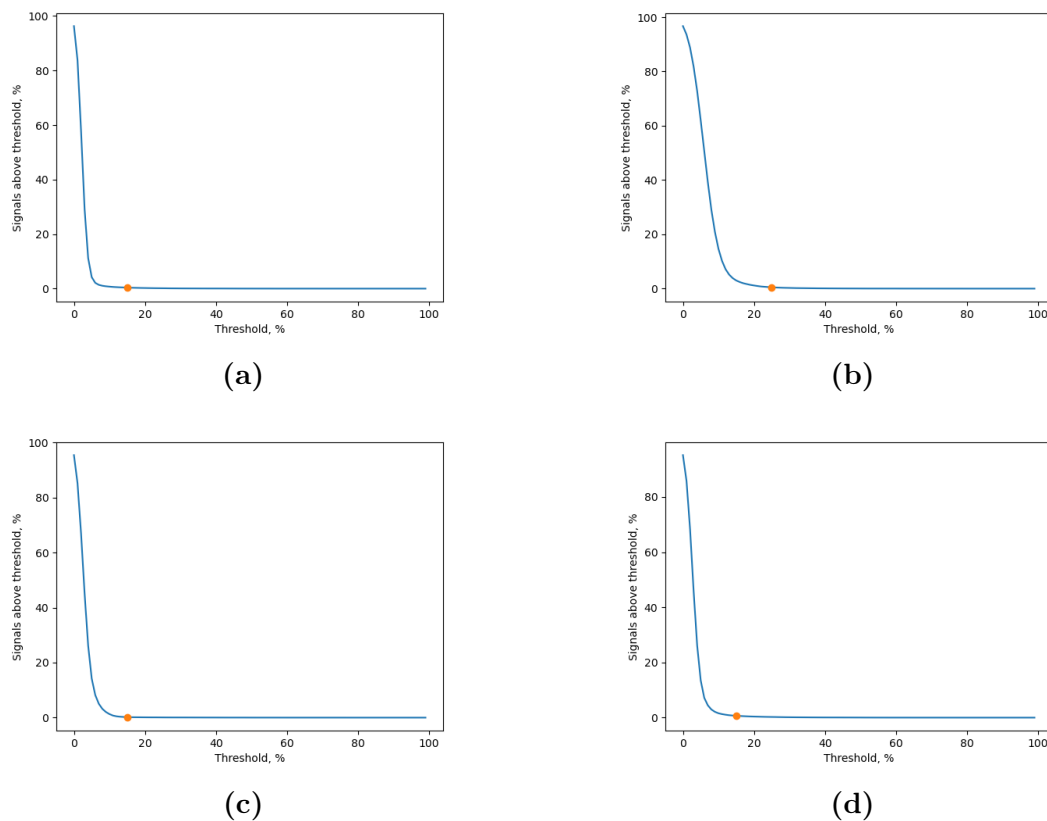
Figure 5.13: Graphs showing the reverse cumulative value distribution in some selected loading maps from scan B2. The values on the y-axis is the percentage of pixels in the loading map that has a loading value above a threshold given by the x-axis, which shows percentage of the maximum value present in the loading map. The orange dots shows where the thresholds were set for phase map creation. The phases the distributions are taken from are (a) β'', (b) in-plane β'', (c) L and (d) β'_{Cu}

5.4.3   Changes in phase composition

In a previous study by Sunde [36] the phase fractions of the M-alloy at peak-hardness was found to be around 70% β'' and 10% each for L, β' and U2. When the alloy was further aged to an overaged condition, the fraction of β'' and U2 was reduced, while the fraction of β' and L increased, and Q' was introduced to the composition. The M-alloy used by Sunde had a slightly different ageing profile to reach T6-condition compared to the one used in this thesis, as it was artificially aged at 180°Cfor 3 hours, compared to 160°Cfor 6 hours. Additionally the method of finding phase fractions is different than what was used in this thesis. As a result the numbers found by Sunde is not directly comparable to the numbers given in Table 4.3, the trends in the changes observed can however be useful. Using this study as a reference as to what to expect, it can be expected that the amount of β'' will decrease as the distance from the HAZ/EZ interface is decreased, while the fraction of L, β' and Q' will increase.

In D4 the primary phase found was $beta''$, which constituted 95.9% of all signals detected, which is significantly higher than what was found in the peak-aged M-

alloy by Sunde. Since U2 and β' was not detected in this scan, it is expected that the fraction of β'' would be higher than what was found by Sunde. However, the ratio of L to β'' is still lower than what is expected, as the relative amount of L is expected to increase with temperature, while here it is lower than what was found in the T6 condition. As mentioned this could be due to differences in the method and age-hardening treatment. It could also be an indication that the fraction of L found is lower than the real fraction present in the material. If this is the case, then it might be expected that a similar under-representation of the L phase will be the case in all scans.

In C3 Q' was introduced to the phase composition, which was primarily found along the deformation lines. Due to the location of these signals it is difficult to assess whether these precipitates formed during welding or if they were present at the T6 condition. It is known that heterogeneous nucleation sites like deformation lines favour the formation of post β'' phases such as Q' [48]. It was also observed that precipitates along dislocation lines in the reference sample appeared to be of another phase than β'' (Figure 5.8). The phase does however also appear in some locations that does not correspond to a dislocation line, which suggests that some of it may have formed during welding. The amount of Q' signals that appears in the same point as a β'' is almost equal to the amount of Q' signals that appears alone. This suggests that there is a significant amount of precipitates that contain unit-cells of both Q' and β'', which is an indication that a phase transformation has occurred. Looking at the phase map, Figure 4.15, it can be seen that the pure Q' signals primarily appear at the deformation lines, while the hybrid signals are more evenly distributed. It seems likely that the Q' precipitates may have formed prior to welding at the dislocation lines, while the hybrid Q'/β'' precipitates have formed during welding.

The B2 scan shows a large amount of β', which was not detected at all in the other scans. The phase primarily shows up in the same regions as β'', similar to Q' outside of dislocations in C3. The fraction of hybrid β'/β'' signals is however larger than what was observed for Q'/β'' in C3, with around 25% of β'' signal locations also showing β' signals, compared to around 5% in C3. Additionally there is a significant amount signals that show only β', without the presence of dislocations, suggesting that some precipitates are able to fully transform from β''. The increase in temperature from 3 mm to 2 mm distance would increase the reaction rate for the phase transformation in B2, explaining why a larger amount of hybrid precipitates are found. It can also explain why β' forms instead of Q', since Q' requires Cu in its structure. It is possible that the reaction rate for the phase transition is faster than the rate of which Cu is able to diffuse to the reaction, causing a transformation to the non Cu containing β' phase instead.

The primary phase detected in all 3 scans was β'', although it constituted smaller fraction the closer the scan was to the EZ/HAZ interface, especially when looking at the amount of β'' that appeared alone. Simultaneously the density of precipitates is reduced when the EZ/HAZ interface is approached. Which might suggest that β'' is the primary phase that is dissolved, while other phases survive the temperature increase to a greater amount. One way to test this hypothesis is to use the phase fraction of L that was detected in scan D4 and predict what would be expected in C3 and B2, then compare it to the actual measured fractions in C3 and B2. For this calculation any signal containing L will be used, which is 4.1%

of all signals in D4. If the amount of β'' is reduced by a factor of 118/168 in C3 and (47/168) in B2, then the expected fractions of detected L would be 5.7% and 13.17% respectively. The real fractions detected was 12.95% for C3 and 11.2% in B2, which is not a good match for C3, but reasonably close for B2. The amount of L detected in C3 is however influenced by the increased amount of L-phase at the dislocations, and as such the fraction in C3 is not comparable to D4. The result does indicate that the L-phase precipitates did to a larger degree survive the welding compared to β''.

The diffusion constant D applies to solutes in the medium, and will therefore be the same regardless of what phase the solutes dissolve and diffuse from. As such the slower kinetics in dissolution from L-phase precipitates likely is the result of a lower interface concentration compared to β'' at high temperatures.

Since the L-phase to greater degree survived the welding it can be expected that an alloy primarily strengthened by L-phase precipitates could have a lower reduction of hardness in the HAZ. Furthermore it could be expected that the extent of the HAZ would be shorter in such an alloy.

5.4.4   Surface Cu signal

An unexpected signal, shown in Figure 4.13d, was observed in the C3 and D4 scans that does not correspond to any precipitate phase. The signal shows reflections at the same regions where the forbidden $\{0\,1\,1\}$ aluminium spots would have been. According to Wenner et al. [49] this diffraction pattern can be expected when electropolishing aluminium alloys containing Cu, and is the result of layer of θ'-Al$_2$Cu between the aluminium matrix and surface aluminium oxide, or alternatively a Cu-enriched aluminium region underneath this phase. A map of the corresponding loading values to this diffraction pattern in C3 is shown in Figure 5.14.
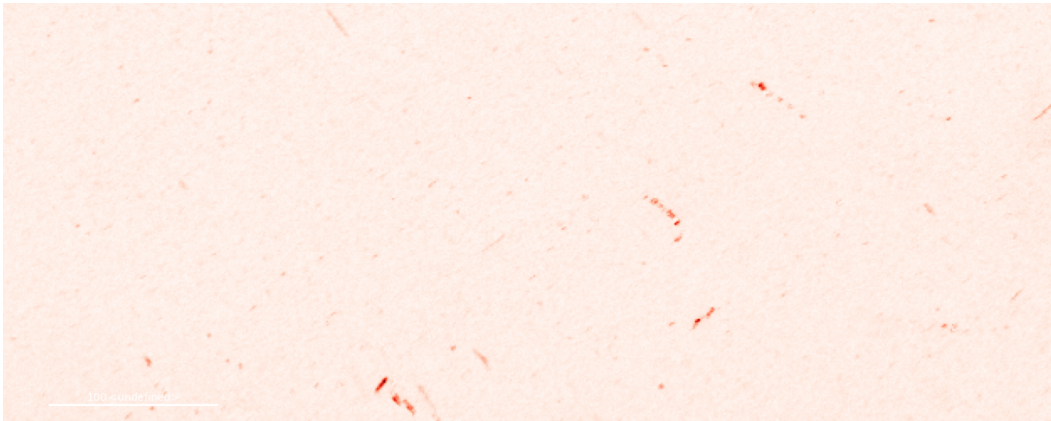
Figure 5.14: Loading map corresponding to the θ'-Al$_2$Cu diffraction pattern shown in Figure 4.13d, the intensity of the signal is proportional to the red intensity. The signal is strongest along the dislocations, which have a lot of Cu containing phases, but it also has an increased presence at other precipitate sites.

From the loading map of θ' it is seen that the signal is strongest in the deformed regions, these regions also showed strong signals of the Cu containing L and Q' phases. There is also weaker, but still noticeable signal coming from what

seems to be precipitates, both in-plane and along the optical axis. The reason for this is not entirely clear, it could be that the Cu in θ'-Al$_2$Cu comes from the aluminium sample itself, and has favourable conditions to form at dislocation due to the precipitates present there contain a higher amount of Cu. This explanation suggests that there are a lot more Cu rich precipitates in the sample than what is identified. Another explanation is that the Cu comes from the electrolyte solution, and that the formation of θ'-Al$_2$Cu has more favourable conditions to form at the interface of precipitates and deformations. According to Wenner the alloy itself does not need to contain Cu for the θ'-Al$_2$Cu layer to form, as long as the electrolyte used contains Cu.

It would be beneficial to know if Cu from the Cu containing precipitates contribute to the θ'-Al$_2$Cu layer, as it would make it possible to use the loading map of this diffraction pattern to evaluate if the phase maps created show an accurate result. In Figure 5.15 an alternate phase map is created using the θ'-Al$_2$Cu loading instead of the L and Q' loadings. The phase map is strikingly similar to the phase map created with L and Q', and the relative amount of θ'-Al$_2$Cu to β'' signals is comparable to the relative amount of combined Q' and L to β'' in the original phase map, the phase composition for the two methods are given in Table 5.1. Since the Cu is hypothesised to come from any Cu containing precipitates, the θ'-Al$_2$Cu may come from precipitates in any orientation. As such the percentages given in the θ'-Al$_2$Cu columns in Table 5.1 also include in-plane β'', which were ignored in the Q'+L columns since the Q' and L signals only appear when orientated along the $[1\,0\,0]$ zone axis.

Table 5.1: Comparison of the phase fractions found by looking at the combined amount of Cu containing phases Q' and L, and θ'-Al$_2$Cu. All numbers are given in percentages of the total amount of signals detected.

Scan	C3		D4	
Method	Q'+L	θ'-Al$_2$Cu	Q'+L	θ'-Al$_2$Cu
β''	79.5	77.7	95.9	96.6
Cu phases	10.3	10.8	1.2	1.2
Combined	10.2	11.5	2.9	2.2

So far the $\{1\,1\,0\}$ diffraction spots has been assumed to come from θ'-Al$_2$Cu, but as is described by Wenner, it may also come from Cu enriched regions in the aluminium matrix. Assuming a partial dissolution of the Cu containing precipitates have occurred during welding, it would be expected that the aluminium matrix surrounding these precipitates would have an increased amount of Cu solutes compared to the matrix as a whole. This could explain why the location and percentage of L and Q' phases detected closely match the regions with strong $\{1\,1\,0\}$ signals.
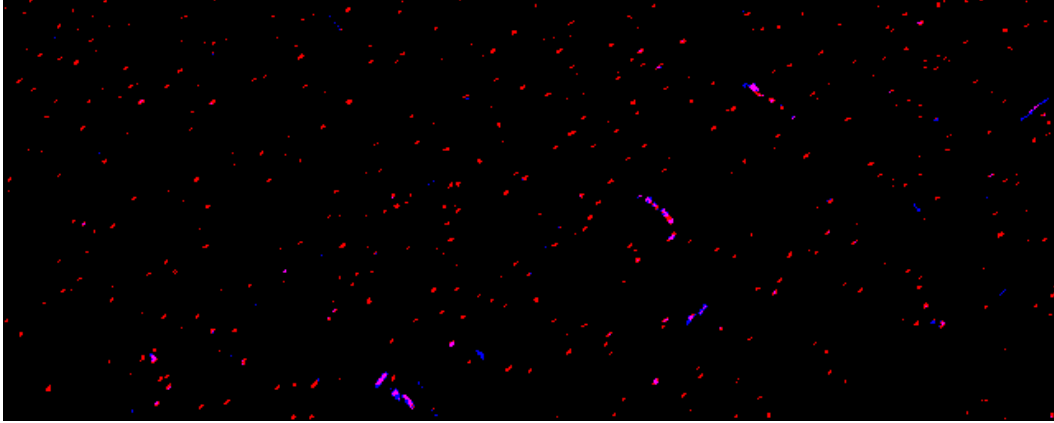
Figure 5.15: Phase map of C3 made using the loading of θ'-Al$_2$Cu instead of the Cu containing precipitates L and Q'. The map is made as an rgb-image, where the value of red or blue is set to the max possible value at the pixels where the β'' and θ'-Al$_2$Cu signals respectively are above a set threshold.

5.5   Summary of mechanisms

The process that occurs at the microscale due to the rapid increase in temperature during welding is complex and characterized by multiple simultaneous reactions, that all have constantly changing parameters. Some of the possible reactions discussed in this thesis is summarized in Figure 5.16. The alloy in the T6 condition has a microstructure mainly consisting of β'' precipitates. As temperature increases these precipitates will start to dissolve and release Mg and Si into the aluminium matrix. As temperature decreases the solubility of Mg and Si will decrease, facilitating growth of the precipitates instead of further dissolution.

The β'' precipitates may also undergo phase transformations to Q' and β'. If the reaction rate of the phase transition is slow the transformations will largely be $\beta'' \rightarrow$ Q' while faster transformations seems to favour $\beta'' \rightarrow \beta'$.

Dissolution may also have occurred from the Q', β' and L precipitates, but due to a lower surface concentration the dissolution rate is slower than for β''.

Close to the HAZ a near complete dissolution of all precipitates occur during the welding. Without the presence of any precipitates the solutes are unable to reprecipitate, leaving the alloy in a super saturated state, which during natural ageing after the welding will see the nucleation of GP-zones.
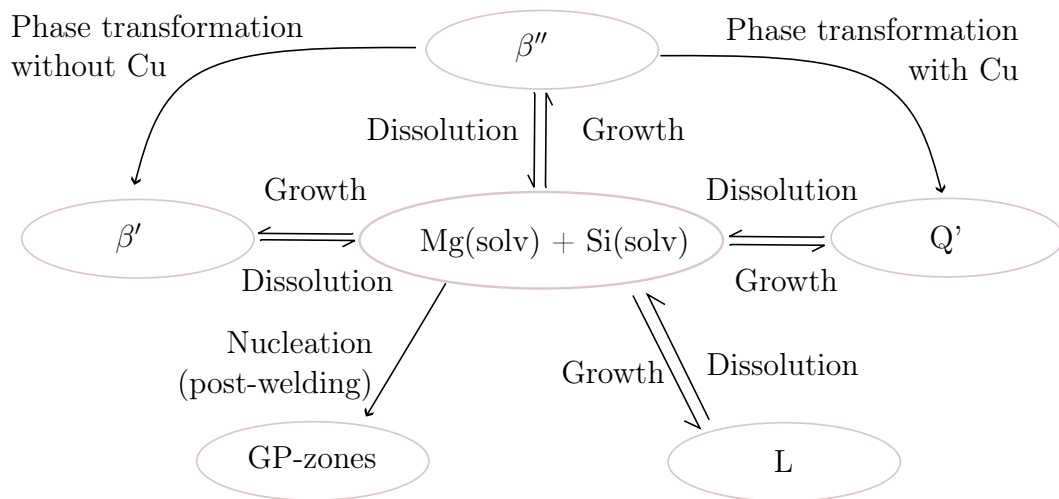
Figure 5.16: Diagram of the possible reactions discussed in this thesis. The alloy in the T6 conditions contain primarily β'' precipitates. As temperature increases the precipitates start to dissolve, increasing the amount of Mg and Si in the aluminum matrix. The dissolution rate of β'' will be dependent on size, causing smaller precipitates to dissolve at a higher rate. The L, Q' and β' phases have a lower interface concentration than β'', and therefore dissolve at a slower rate. The β'' precipitates may also undergo a phase transition to Q', or alternatively to β' if there is not sufficient Cu present. As the temperature decreases after welding, the interface concentration of the precipitates is reduced, and the rate of growth through reprecipitation will become greater than the rate of dissolution. If complete dissolution of nearly all precipitates are achieved, then the Mg and Si solutes are left in a supersaturated state and will nucleate into GP-zones during natural ageing.

CONCLUSIONS

In the presented work the HAZ of the AS of a HYB weld between two plates of an Al-Mg-Si-Cu alloy was investigated using BF and DF TEM imaging, in addition to phase analysis SPED. The results has been discussed in relation to provided hardness measurements and temperature simulations.

From the hardness measurements it was seen that a reduction in hardness occurs at regions within a 5 mm distance from the EZ/HAZ interface. TEM images revealed that the number density of precipitates is decreases as the distance to the EZ/HAZ interface is reduced, with a near complete dissolution of precipitates being observed in the region closest to the EZ/HAZ interface. Simultaneously it was found that the average size of precipitates increases as the distance to the EZ/HAZ interface is reduced.

From SPED phase analysis it was observed that β'' was the most abundant phase in the base material, with a smaller amount of L-phase precipitates also detected. At regions closer to the EZ/HAZ interface β'' was still the primary phase observed, but as distance to the HAZ/EZ interface was reduced the relative amount of β'' decreased. At a 3mm distance from the HAZ/EZ interface, signs of partial phase transitions from β'' to Q' was observed. At a 2 mm distance the amount of observed phase transitions increased, but was shown to primarily be β'' to β'. The suggested reason for this is that the phase transitions at 2 mm are not able to properly integrate Cu into the precipitates due to increased kinetics of the reaction.

The amount of L-detected in the different regions suggests that the L-phase in large part did not dissolve during welding. It is therefore suspected that the reduction in number density of precipitates in large part is a result of dissolution of β'', driven by a significant increase in the dissolution reaction parameters in regions close to the HAZ/EZ interface. This reduction of β'' precipitates is suspected to be the main mechanism behind the loss of hardness in the HAZ.

Due to the increased thermal stability of the L-phase, it is proposed that an alloy primarily strengthened by L-phase precipitates would have a lower reduction of hardness in the HAZ, and that the HAZ would have a shorter extent.

6.1   Future Work

In the presented work the phases present at region closest to the EZ/HAZ interface was not studied. Further studies of this region would be useful to determine if the thermal stability of the L-phase is high enough to prevent dissolution and phase transitions in this region as well. Due to the low density of precipitates in this region it might be better to analyze this region with HAADF-STEM instead of using SPED, although SPED should also be a viable option.

It was proposed that alloys primarily strengthened by L-phase precipitates may have a higher resistance to the temperature increase from welding, and as such have smaller and less affected HAZ. Future studies of HYB-welds of such alloys would therefore be of interest.

REFERENCES

[1] C. D. Marioara et al. "The effect of Cu on precipitation in Al–Mg–Si alloys". In: *Philosophical Magazine* 87.23 (2007), pp. 3385–3413.

[2] Calin D. Marioara et al. "Improving Thermal Stability in Cu-Containing Al-Mg-Si Alloys by Precipitate Optimization". eng. In: *Metallurgical and materials transactions. A, Physical metallurgy and materials science* 45.7 (2014), pp. 2938–2949. ISSN: 1073-5623.

[3] D. B. Williams and C. B. Carter. *Transmission Electron Microscopy, A Textbook for Materials Science*. Springer, 2009.

[4] B Fultz and J Howe. *Transmission Electron Microscope and Diffractometry of Materials, Fourth Edition*. Springer, 2013.

[5] C. Kittel. *An introduction to solid state physics, 8th edition*. Wiley, 2005.

[6] R. J. D. Tilley. *Understanding Solids: The science of Materials (third edition)*. Wiley, 2005.

[7] David A Porter. *Phase transformations in metals and alloys*. eng. London, 1992.

[8] Ian J. Polmear. *Light Alloys*. eng. 2005. ISBN: 9780750663717.

[9] J. R. Davis. *Alloying: Understanding the Basics*. ASM international, 2001.

[10] S. Bandyopadhyay. *Fabrication and Applications of Nanomaterials*. McGraw-Hill Education, 2019.

[11] M.Z. Butt and P. Feltham. "Solid-solution hardening". eng. In: *Journal of materials science* 28.10 (1993), pp. 2557–2576. ISSN: 0022-2461.

[12] Takahiro Hatano. "Dynamics of a dislocation bypassing an impenetrable precipitate: the Hirsch mechanism revisited". eng. In: *arXiv.org* (2006). ISSN: 2331-8422.

[13] O.R Myhr, Ø Grong, and S.J Andersen. "Modelling of the age hardening behaviour of Al–Mg–Si alloys". eng. In: *Acta materialia* 49.1 (2001), pp. 65–75.

[14] Paul G Shewmon. *Diffusion in Solids*. eng. Cham, 2016.

[15] "Dependence of Diffusion on Temperature and Pressure". In: *Diffusion in Solids: Fundamentals, Methods, Materials, Diffusion-Controlled Processes*. Berlin, Heidelberg: Springer Berlin Heidelberg, 2007, pp. 127–149. ISBN: 978-3-540-71488-0. DOI: 10.1007/978-3-540-71488-0_8.

[16] Materials Project. *Mg2Si*. URL: https://materialsproject.org/materials/mp-1367 (visited on 12/13/2022).

[17] C. D. Marioara et al. "Directionality and Column Arrangement Principles of Precipitates in Al-Mg-Si-(Cu) and Al-Mg-Cu Linked to Line Defect in Al". eng. In: *Materials Science Forum* 877 (2016), pp. 461–470. ISSN: 0255-5476.

[18] C.D. Marioara et al. "Post-beta" phases and their influence on microstructure and hardness in 6xxx Al-Mg-Si alloys". eng. In: *Journal of materials science* 41.2 (2006), pp. 471–478. ISSN: 0022-2461.

[19] Jonas Kristoffer Sunde, Sigurd Wenner, and Randi Holmestad. "In situ heating TEM observations of evolving nanoscale Al–Mg–Si–Cu precipitates". eng. In: *Journal of microscopy (Oxford)* 279.3 (2020), pp. 143–147. ISSN: 0022-2720.

[20] G.A. Edwards et al. "The precipitation sequence in Al–Mg–Si alloys". eng. In: *Acta materialia* 46.11 (1998), pp. 3893–3904. ISSN: 1359-6454.

[21] L. Ding et al. "The structural and compositional evolution of precipitates in Al-Mg-Si-Cu alloy". In: *Acta Materialia* 145 (2018), pp. 437–450.

[22] J. K. Sunde. "The effect of Elevated Temperatures on Precipitation in Aluminium Alloys". In: (2020).

[23] Sigmund J. Andersen et al. "Precipitates in aluminium alloys". In: *Advances in Physics: X* 3.1 (2018), p. 1479984. DOI: 10.1080/23746149.2018.1479984.

[24] D. Maisonnette et al. "Effects of heat treatments on the microstructure and mechanical properties of a 6061 aluminium alloy". In: *Materials Science and Engineering: A* 528.6 (2011), pp. 2718–2724.

[25] Mohammad Kazem Besharati Givi. *Advances in friction- stir welding*. eng. Cambridge, England, 2014.

[26] Mr Kailas et al. "Analysis of Tensile Strength, Ultimate Tensile Strength and Micro Hardness for TIG Welding on Material AISI 304 Stainless Steel". In: (Jan. 2016), pp. 2321–0613.

[27] Rajiv S Mishra and Mageshwari Komarasamy. *Friction Stir Welding of High Strength 7XXX Aluminum Alloys*. eng. Oxford, 2016. ISBN: 9780128094655.

[28] Nicolas J. Peter et al. "Atomic level bonding mechanism in steel/aluminum joints produced by cold pressure welding". eng. In: *Materialia* 7 (2019), p. 100396. ISSN: 2589-1529.

[29] Ø. Grong, L. Sandnes, and F. Berto. "A status report on the hybrid metal extrusion & bonding (HYB) process and its applications". In: *Material Design & Processing Communications* 1.2 (2019). e41 MDPC-2019-005, e41.

[30] S. Jannet, P.K. Mathews, and R. Raja. "Comparative investigation of friction stir welding and fusion welding of 6061 T6 – 5083 O aluminum alloy based on mechanical properties and microstructure". eng. In: *Bulletin of the Polish Academy of Sciences. Technical sciences* 62.4 (2014), pp. 791–795. ISSN: 0239-7528.

[31] L. Sandnes et al. "Qualification of the hybrid metal extrusion & bonding (HYB) process for welding of aluminium offshore structures". eng. In: *Material design & processing communications* 3.5 (2021), n/a. ISSN: 2577-6576.

[32] L. Sandnes et al. "Fatigue properties of AA6060-T6 butt welds made by hybrid metal extrusion & bonding". eng. In: *Fatigue and fracture of engineering materials and structures* 43.10 (2020), pp. 2349–2358. ISSN: 8756-758X.

[33] Wenchao Yang et al. "The diffraction patterns from beta" precipitates in 12 orientations in Al–Mg–Si alloy". eng. In: *Scripta materialia* 62.9 (2010), pp. 705–708. ISSN: 1359-6462.

[34] Shang Zhu et al. "Transformation behavior of precipitates during artificial aging at 170 °C in Al–Mg–Si–Cu alloys with and without Zn addition". eng. In: *Rare metals* 40.7 (2021), pp. 1907–1914. ISSN: 1001-0521.

[35] J.K. Sunde et al. "The evolution of precipitate crystal structures in an Al-Mg-Si(-Cu) alloy studied by a combined HAADF-STEM and SPED approach". In: *Materials Characterization* 142 (2018), pp. 458–469. ISSN: 1044-5803. DOI: https://doi.org/10.1016/j.matchar.2018.05.031.

[36] Jonas K. Sunde, Calin D. Marioara, and Randi Holmestad. "The effect of low Cu additions on precipitate crystal structures in overaged Al-Mg-Si(-Cu) alloys". eng. In: *Materials characterization* 160 (2020), p. 110087.

[37] P. M. Kelly et al. "The determination of foil thickness by scanning transmission electron microscopy". In: *physica status solidi (a)* 31.2 (1975), pp. 771–780.

[38] D Delille, R Pantel, and E Van Cappellen. "Crystal thickness and extinction distance determination using energy filtered CBED pattern intensity measurement and dynamical diffraction theory fitting". In: *Ultramicroscopy* 87.1 (2001), pp. 5–18. DOI: https://doi.org/10.1016/S0304-3991(00)00067-X.

[39] Alexander Wimmer. *Neuman Alumnium, Austria.*

[40] Jørgen Sørhaug. *Unpublished work.*

[41] Øyvind Frigaard. *A process model for friction stir welding of age hardening aluminium alloys.* eng. Trondheim, 1999.

[42] O.R. Myhr and Ø. Grong. "Process modelling applied to 6082-T6 aluminium weldments—I. Reaction kinetics". eng. In: *Acta metallurgica et materialia* 39.11 (1991), pp. 2693–2702.

[43] The HyperSpy development team. *Hyperspy Documentation.* URL: https://hyperspy.org/hyperspy-doc/current/index.html (visited on 05/30/2023).

[44] Alexander Vasilyev, Alexander Gruzdev, and N. Kuz'min. "Calculation of the Solvus Temperature of Metastable Phases in the Al-Mg-Si Alloys". In: *Physics of The Solid State - PHYS SOLID STATE* 53 (Sept. 2011), pp. 1902–1908. DOI: 10.1134/S1063783411090320.

[45] G. Korablev. "Calculation of activation energy of diffusion and self-diffusion". eng. In: *European chemical bulletin* 7.1 (2018), pp. 23–29. ISSN: 2063-5346.

[46]   J. D. Robson. "Deformation Enhanced Diffusion in Aluminium Alloys: Physical Metallurgical and Materials Science". In: *Metallurgical and Materials Transactions* 51.10 (Oct. 2020), pp. 5401–5413. DOI: `DOI:10.1007/s11661-020-05960-5`.

[47]   K. Teichmann et al. "HRTEM study of the effect of deformation on the early precipitation behaviour in an AA6060 Al–Mg–Si alloy". In: *Philosophical Magazine* 91.28 (2011), pp. 3744–3754. DOI: `10.1080/14786435.2011.593577`.

[48]   Takeshi Saito et al. "The Effects of Low Cu Additions and Predeformation on the Precipitation in a 6060 Al-Mg-Si Alloy". eng. In: *Metallurgical and materials transactions. A, Physical metallurgy and materials science* 44.9 (2013), pp. 4124–4135.

[49]   Sigurd Wenner et al. "Copper enrichment on aluminium surfaces after electropolishing and its effect on electron imaging and diffraction". In: *Materials Characterization* 172 (2021), p. 110846. DOI: `https://doi.org/10.1016/j.matchar.2020.110846`.

APPENDICES
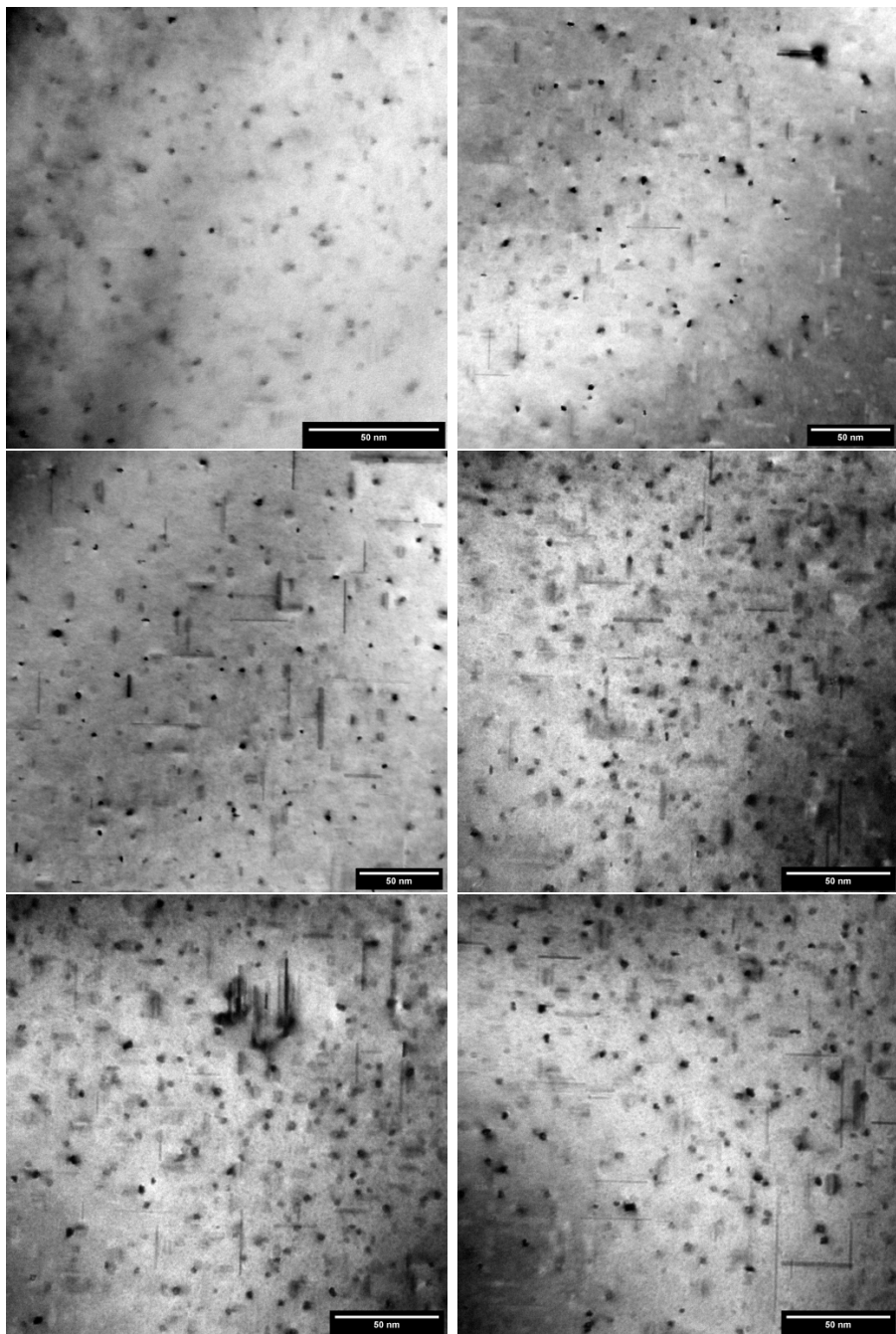
A - TEM IMAGES

Figure .1: TEM images from series B
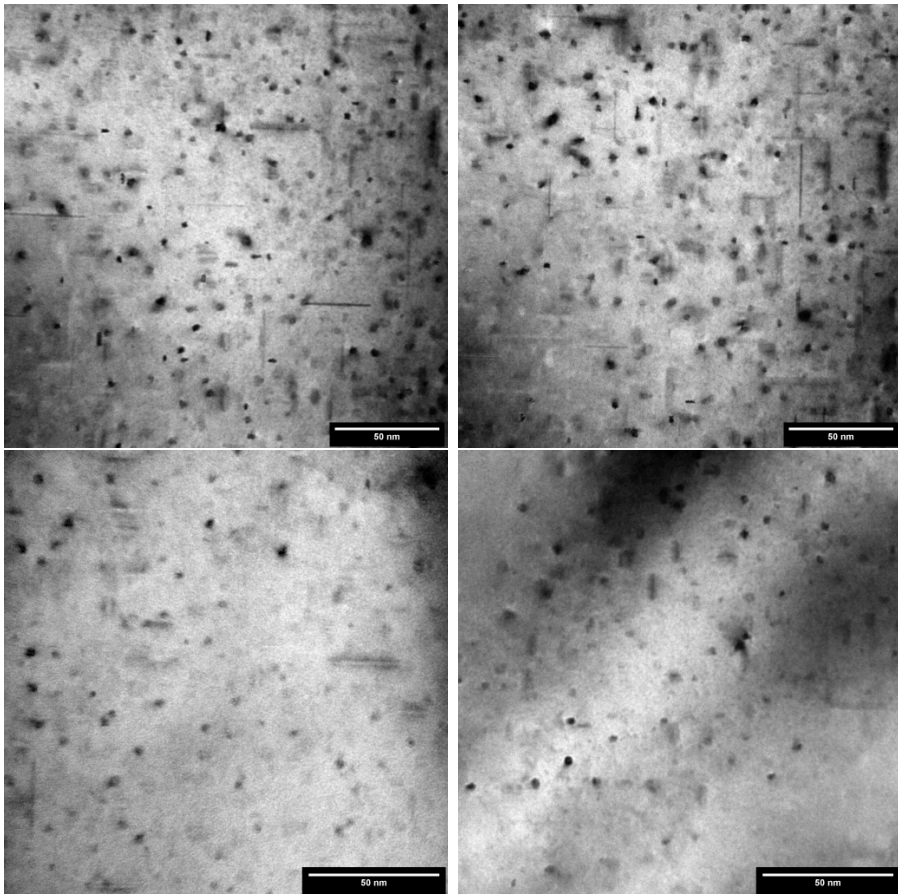
Figure .2: TEM images from series B
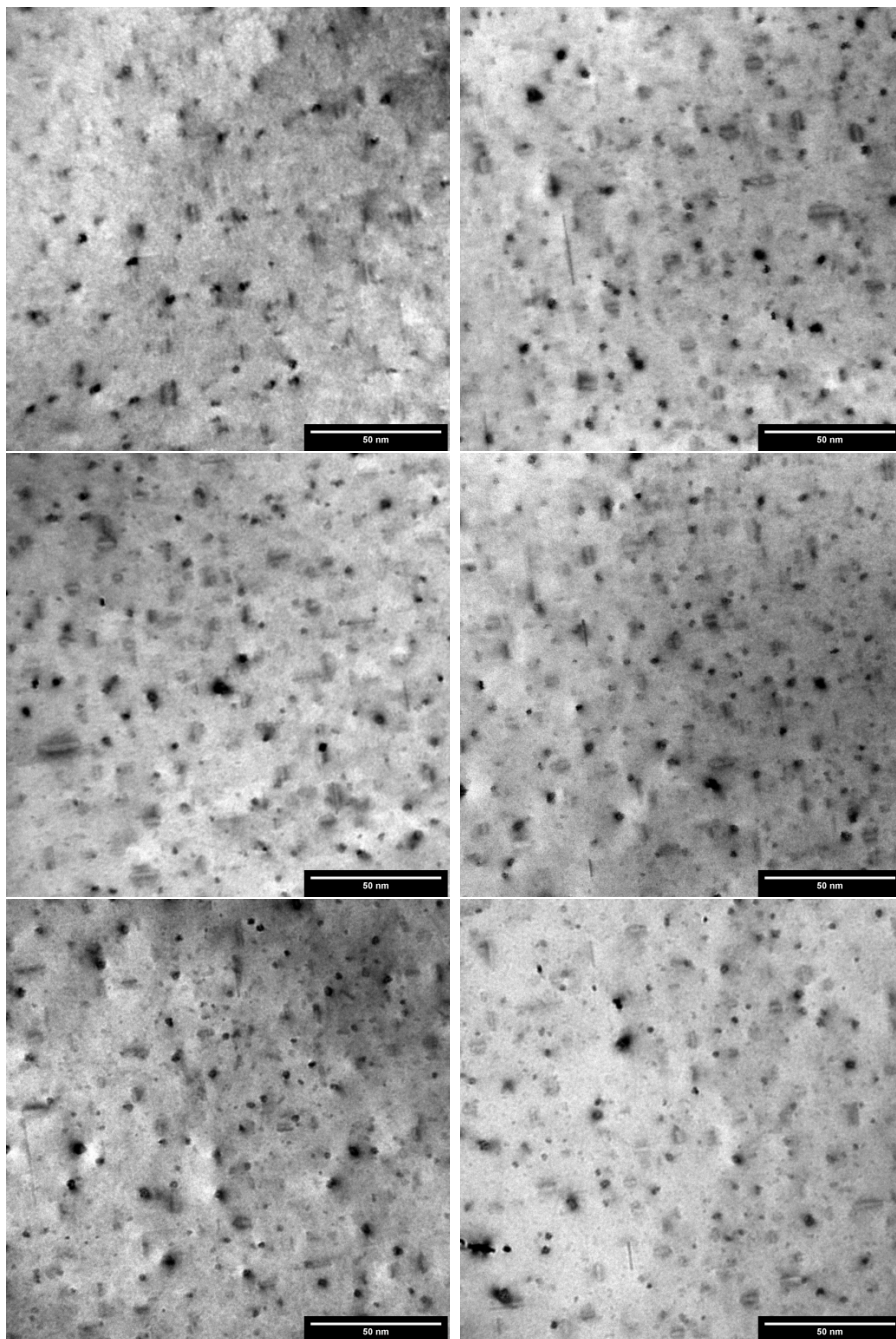
Figure .3: TEM images from series C
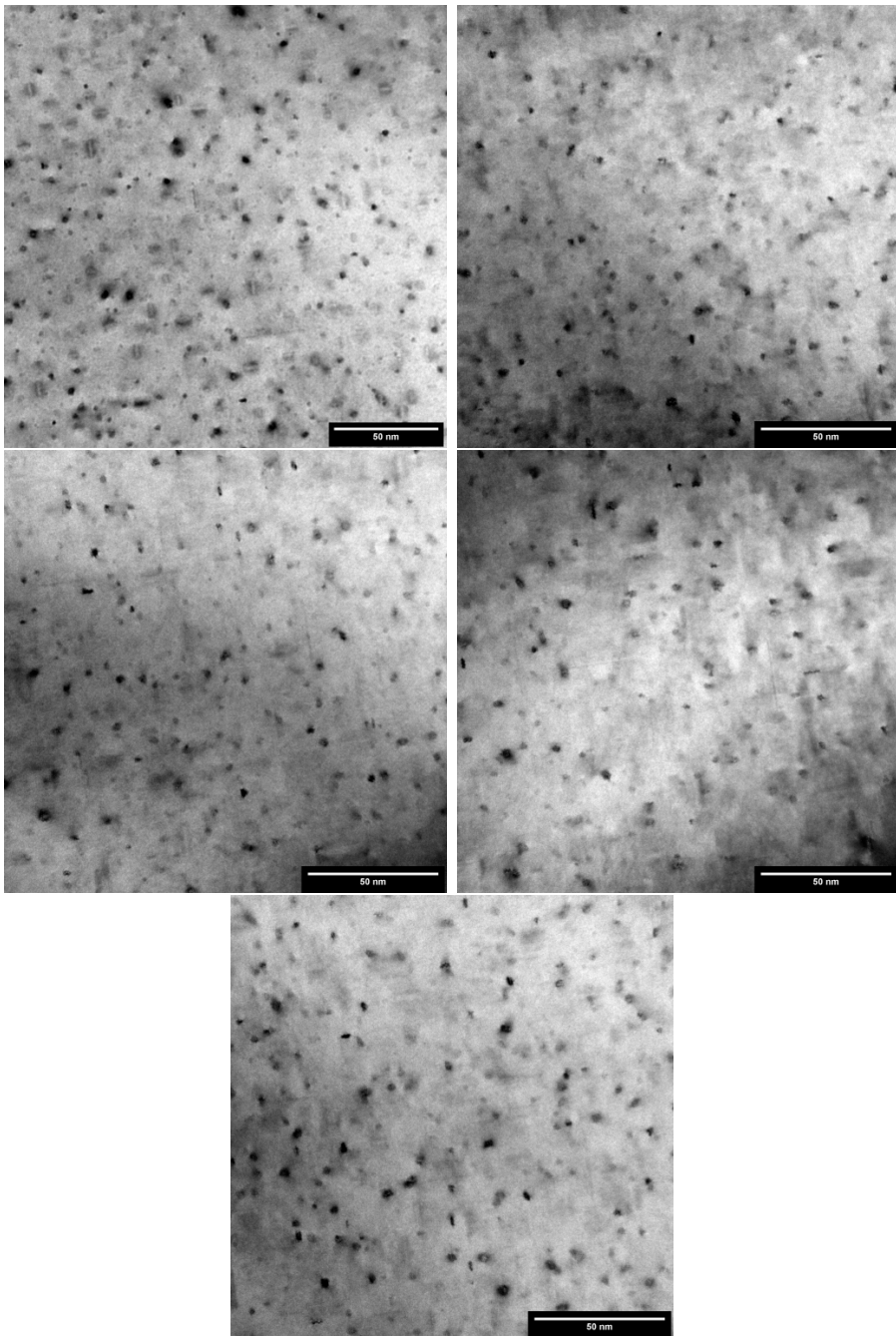
Figure .4: TEM images from series C
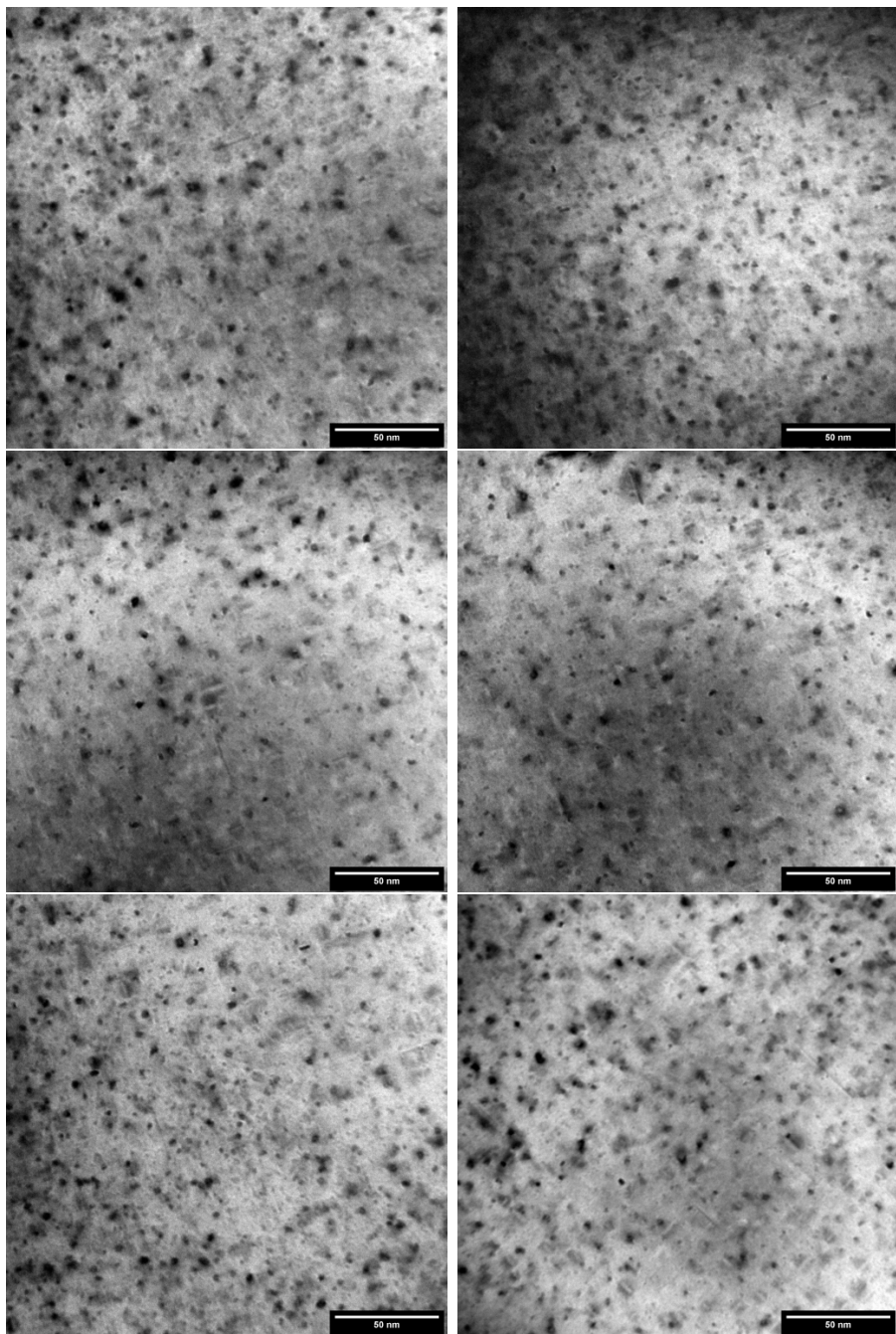
Figure .5: TEM images from series D
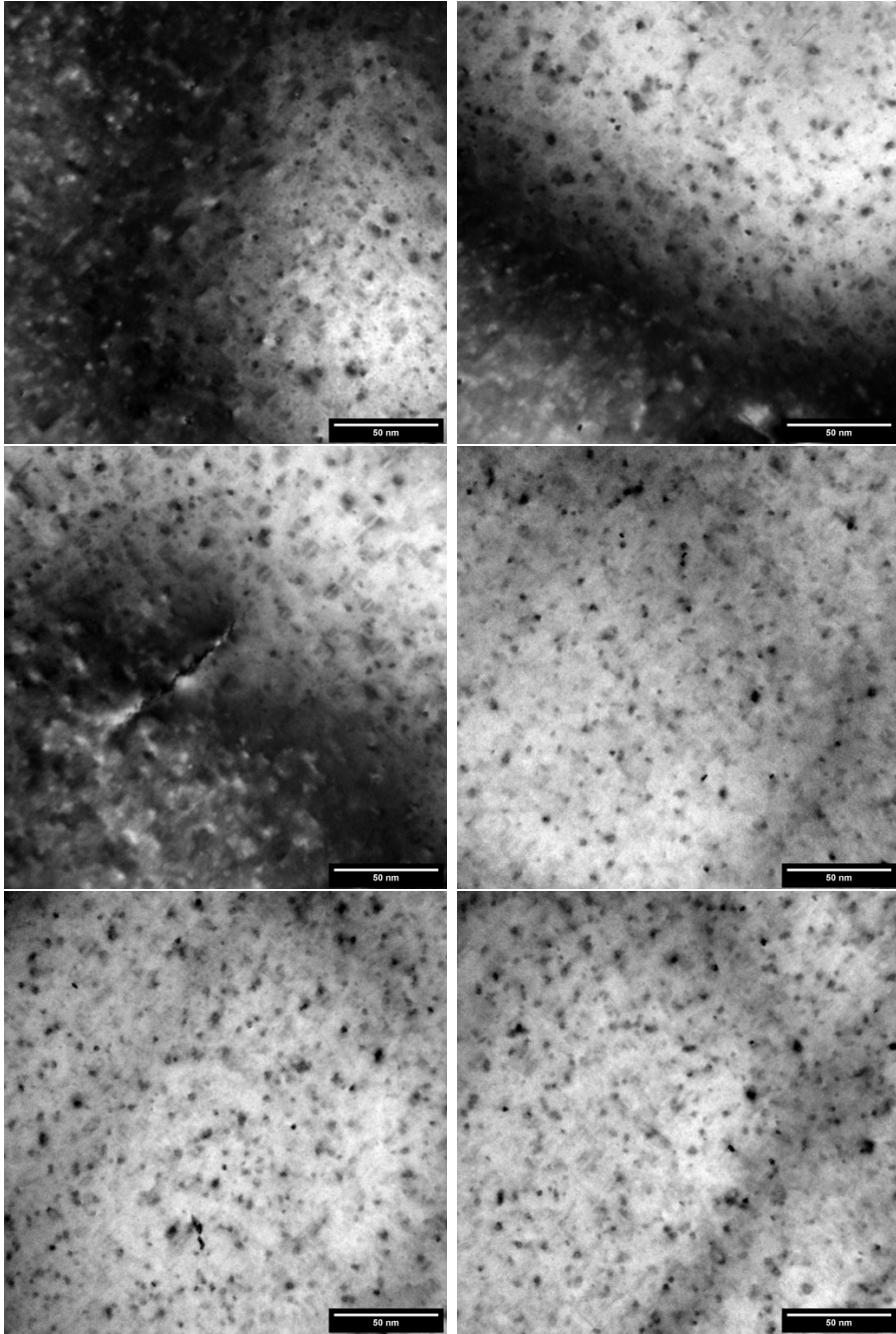
Figure .6: TEM images from series D

B - PHASE MAP CREATION CODE

Decomposition of signal

Before this notebook is used, the signal should be preprocessed by centering the signal and cropping the navigation field

```python
%matplotlib
%config IPCompleter.use_jedi=False
import hyperspy.api as hs
import pyxem as pxm
import numpy as np
import matplotlib.pyplot as plt
from matplotlib.colors import SymLogNorm
from pathlib import Path
from hyperspy.signals import Signal2D
from PIL import Image
```

```python
#load datapath
datapath = Path('C:/Users/hakon/Documents/Skole/master/TEMdata/SPED/SPED_C3/defa
signal = Signal2D(hs.load(datapath, lazy = True))
signal.change_dtype('float32')
```

```python
signal.plot(norm = 'symlog')
```

Need to generate a mask that masks out Al spots and direct beam. The mask consists of a 2D boolean array with the same size as the unmasked signal space. When decompositioning, only the points marked False will be considered(True = ignore this area) Step 1 is to limit signal mesh to only be false within the (2,2,0) radius

```python
s = signal.inav[signal.axes_manager.indices]
s.plot(norm='symlog')
roi = hs.roi.CircleROI(signal.axes_manager.signal_shape[0]/2, signal.axes_manage
roi.add_widget(s)
```

```python
#using roi
radius = int(roi.r)+1
mesh = np.zeros(signal.axes_manager.signal_shape, dtype = bool)
#print(signal.axes_manager.signal_shape)
for x in range(signal.axes_manager.signal_shape[0]):
    for y in range(signal.axes_manager.signal_shape[1]):
        if ((roi.cx-x)**2+(roi.cy-y)**2 < roi.r**2):
            mesh[y,x] = False
        else:
            mesh[y,x] = True
```

Step 2 is to remove the (220), (200) and (000) spots, the second code snippets need to be repeated untill all spots are covered (9 times).

```python
#s.plot(norm='symlog')
roi_spot = hs.roi.CircleROI(64, 64, 10)
roi_spot.add_widget(s)
```

```python
radius = int(roi_spot.r)+1
for x in range(int(roi_spot.cx)-radius, int(roi_spot.cx)+radius):
```

```
        for y in range(int(roi_spot.cy)-radius, int(roi_spot.cy)+radius):
            if ((roi_spot.cx-x)**2+(roi_spot.cy-y)**2 < roi_spot.r**2):
                mesh[y,x] = True
```

Visualized the mask

In [ ]:
```
diffraction_mask = hs.signals.Signal2D(mesh).T
diffraction_mask.plot()
```

In [ ]:
```
#save mask as numpy array to reuse later
np.save('C:/Users/hakon/Documents/Skole/master/TEMdata/SPED/SPED_B2/mesh.npy', m
```

In [ ]:
```
#loading a previously made mask
mesh = np.load('C:/Users/hakon/Documents/Skole/master/TEMdata/SPED/SPED_D4/mesh.
```

In [ ]:
```
diffraction_mask.save(datapath.with_name(f'{datapath.stem}_mask30.hspy'), overwr
```

Decompose the signal into factors and loadings, visualize the data.

In [ ]:
```
signal.decomposition(algorithm='NMF', output_dimension=40, signal_mask = mesh, r
```

In [ ]:
```
factors = signal.get_decomposition_factors()
loadings = signal.get_decomposition_loadings()
factors.plot(cmap = 'inferno')
loadings.plot(cmap = 'Reds')
```

Save the factors and loading data

In [ ]:
```
factors.save(datapath.with_name(f'{datapath.stem}_factor40.hspy'), overwrite=Tru
loadings.save(datapath.with_name(f'{datapath.stem}_loadings40.hspy'), overwrite=
```

Loading previously decomposed files:

In [ ]:
```
loadings_datapath = Path('c://Users/hakon/Documents/Skole/master/TEMdata/SPED/SP
factors_datapath = Path('c://Users/hakon/Documents/Skole/master/TEMdata/SPED/SPE
loaded_loadings = Signal2D(hs.load(loadings_datapath, lazy=True))
loaded_factors = Signal2D(hs.load(factors_datapath, lazy=True))
```

In [ ]:
```
loaded_loadings.plot(cmap = 'Reds')
loaded_factors.plot(cmap = 'inferno')
```

In [ ]:
```
#D4
phase_key = {
    'Al': [],
    'beta``': [6, 7, 9, 12, 14, 20],
    'L': [13, 19],
    'beta``(in-plane)': [15, 17],
    'Q': [],
    'Cu': [28],
    'Not indexed': [1, 2, 3, 4, 5, 8, 10, 11, 16, 18, 21, 22, 23, 24, 25, 26, 27
}
```

In [ ]:
```
#C3
phase_key = {
    'Al': [],
```

```
        'beta``': [2, 16, 19, 29],
        'L': [4, 10, 18],
        'beta``(in-plane)': [13, 14],
        'Q': [17, 20, 22, 27],
        'Cu': [21],
        'Not indexed': [0, 1, 3, 5, 6, 7, 8, 9, 11, 12, 15, 23, 24, 25, 26, 28]
    }
```

In [ ]:
```python
#B2
phase_key = {
    'Al': [],
    'beta``': [2, 6, 13, 19, 20, 21],
    'L': [10, 12, 24],
    'beta``(in-plane)': [15, 16],
    'Q': [8, 24],
    'Not indexed': [0, 1, 3, 4, 5, 7, 9, 11, 14, 17, 18, 22, 23]
}
```

In [ ]:
```python
x = len(loaded_loadings.inav[0].data)
y = len(loaded_loadings.inav[0].data[0])
```

In [ ]:
```python
r = np.zeros((x, y), dtype=bool)
g = np.zeros((x, y), dtype=bool)
b = np.zeros((x, y), dtype=bool)

threshold = 0.15
for i in phase_key['beta``']:
    dataArray = np.array(loaded_loadings.inav[i].data)
    maximumValue = dataArray.max()
    for j in range(x):
        for k in range(y):
            if dataArray[j][k] > maximumValue*threshold:
                r[j][k] = True
"""threshold = 0.25        #add for phase map creation, remove for phase fracti
for i in phase_key['beta``(in-plane)']:
    dataArray = np.array(loaded_loadings.inav[i].data)
    maximumValue = dataArray.max()
    for j in range(x):
        for k in range(y):
            if dataArray[j][k] > maximumValue*threshold:
                r[j][k] = True"""
threshold = 0.15
for i in phase_key['L']:
    dataArray = np.array(loaded_loadings.inav[i].data)
    maximumValue = dataArray.max()
    for j in range(x):
        for k in range(y):
            if dataArray[j][k] > maximumValue*threshold:
                g[j][k] = True
threshold = 0.15
for i in phase_key['Q']:
    dataArray = np.array(loaded_loadings.inav[i].data)
    maximumValue = dataArray.max()
    for j in range(x):
        for k in range(y):
            if dataArray[j][k] > maximumValue*threshold:
                b[j][k] = True
```

```python
#Plotting reverse cumulative distribution of loadings

percentages = np.zeros(100)
thresholds = np.zeros(100)
dataArray = np.array(loaded_loadings.inav[10].data)

totalpixels = x*y
maximumValue = dataArray.max()
for i in range(100):
    threshold = i/100
    thresholds[i] = i
    counts = 0
    realthreshold = maximumValue*threshold
    for j in range(x):
        for k in range(y):
            if dataArray[j][k] > realthreshold:
                counts += 1
    percentages[i] = counts*100/totalpixels

plt.plot(thresholds, np.log(percentages))
plt.plot(thresholds[15], np.log(percentages[15]), 'o')
plt.xlabel('Threshold, %')
plt.ylabel('Signals above threshold, %')
```

```python
betacount = 0
Lcount = 0
Qcount = 0
betaQcount = 0
betaLcount = 0
LQcount = 0
betaLQcount = 0

for i in range(x):
    for j in range(y):
        if r[i][j] and not b[i][j] and not g[i][j]:
            betacount += 1
        if r[i][j] and b[i][j] and not g[i][j]:
            betaQcount += 1
        if r[i][j] and g[i][j] and not b[i][j]:
            betaLcount += 1
        if b[i][j] and not r[i][j] and not g[i][j]:
            Qcount += 1
        if b[i][j] and not r[i][j] and g[i][j]:
            LQcount += 1
        if g[i][j] and not b[i][j] and not r[i][j]:
            Lcount += 1
        if r[i][j] and b[i][j] and g[i][j]:
            betaLQcount += 1

totalcount = betacount + betaQcount + Qcount + Lcount + betaLcount + LQcount + b

betafrac = betacount/totalcount
betaqfrac = betaQcount/totalcount
qfrac = Qcount/totalcount
lfrac = Lcount/totalcount
betaLQfrac = betaLQcount/totalcount
lqfrac = LQcount/totalcount
betaLfrac = betaLcount/totalcount
```

```python
print(betafrac * 100, betaqfrac * 100, qfrac*100, lfrac * 100, betaLfrac *100, l
```

```python
#rgb = np.dstack(image1, image2, image3)
rgbArray = np.zeros((x,y,3), 'uint8')
rgbArray[..., 0] = r*255 #Red = beta''
rgbArray[..., 1] = g*255 #green = L
rgbArray[..., 2] = b*255 #blue = Q
img = Image.fromarray(rgbArray)
img.save('C:/Users/hakon/Documents/Skole/master/figurer/rgb_maptest.png')
```

```python
#rgb = np.dstack(image1, image2, image3)
rgbArray = np.zeros((x,y,3), 'uint8')
rgbArray[..., 0] = r*255 #Red = beta''
rgbArray[..., 1] = g*255 #green = L
rgbArray[..., 2] = b*255 #blue = Q
img = Image.fromarray(rgbArray)
```

C - SPED DECOMPOSITION FACTORS AND LOADINGS

This chapter presents all the diffraction patterns and their corresponding loading maps used to create the Phase maps in Figure 4.14, Figure 4.15 and Figure 4.16.

B2 scan

(a)

(b)

(c)

(d)

(e)

(f)
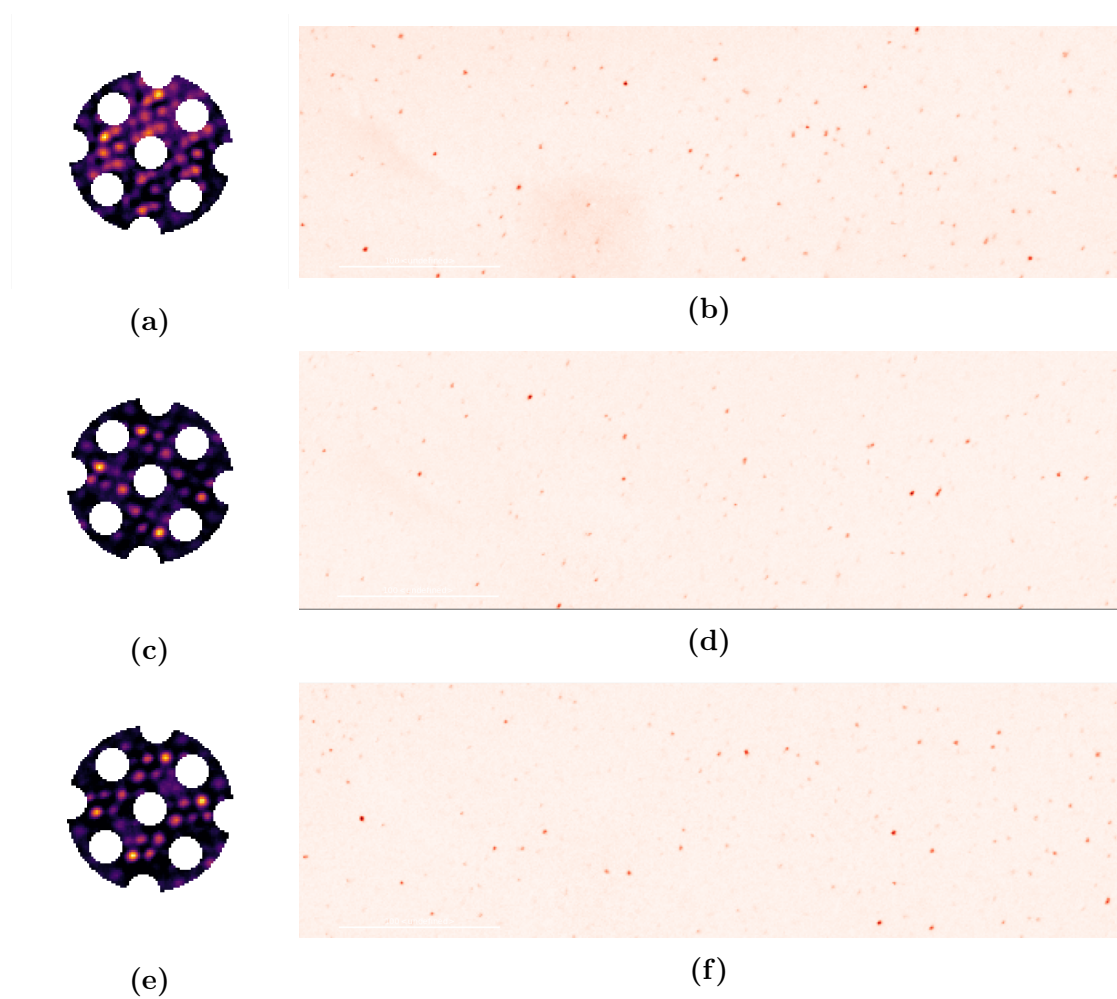
Figure C.1: β'' signals
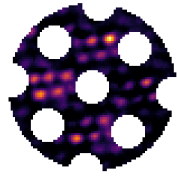
(a)
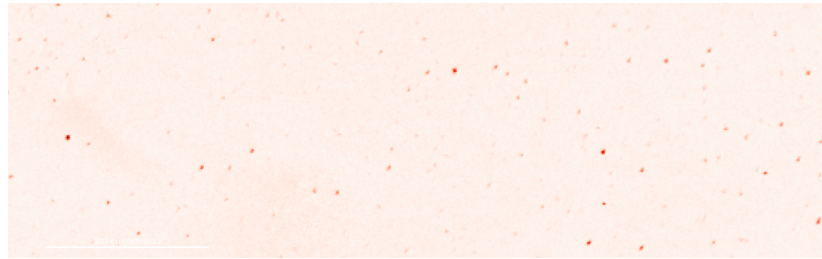
(b)
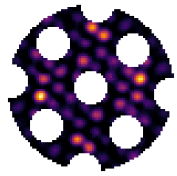
(c)
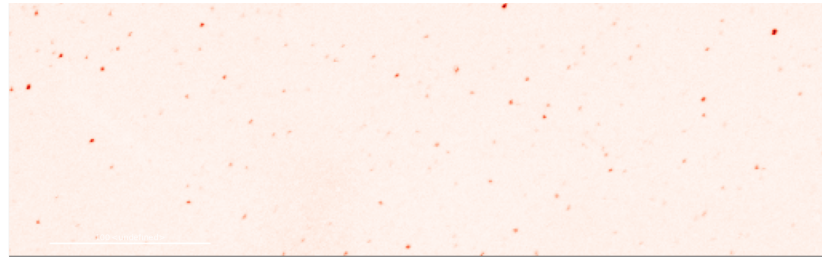
(d)
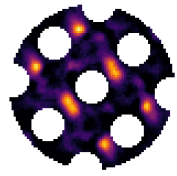
(e)
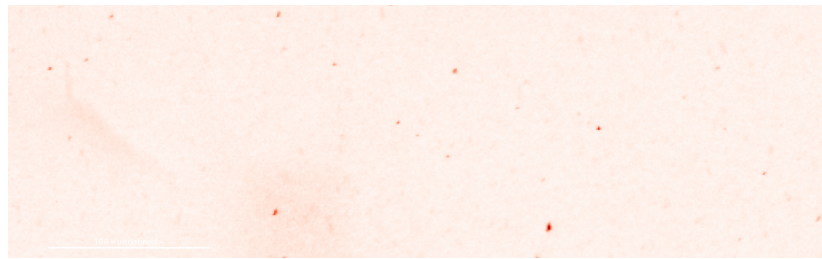
(f)

(g)

(h)

Figure C.2: (a) and (c) β'', (e) and (g) L

(a)

(b)

(c)

(d)

(e)

(f)
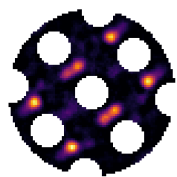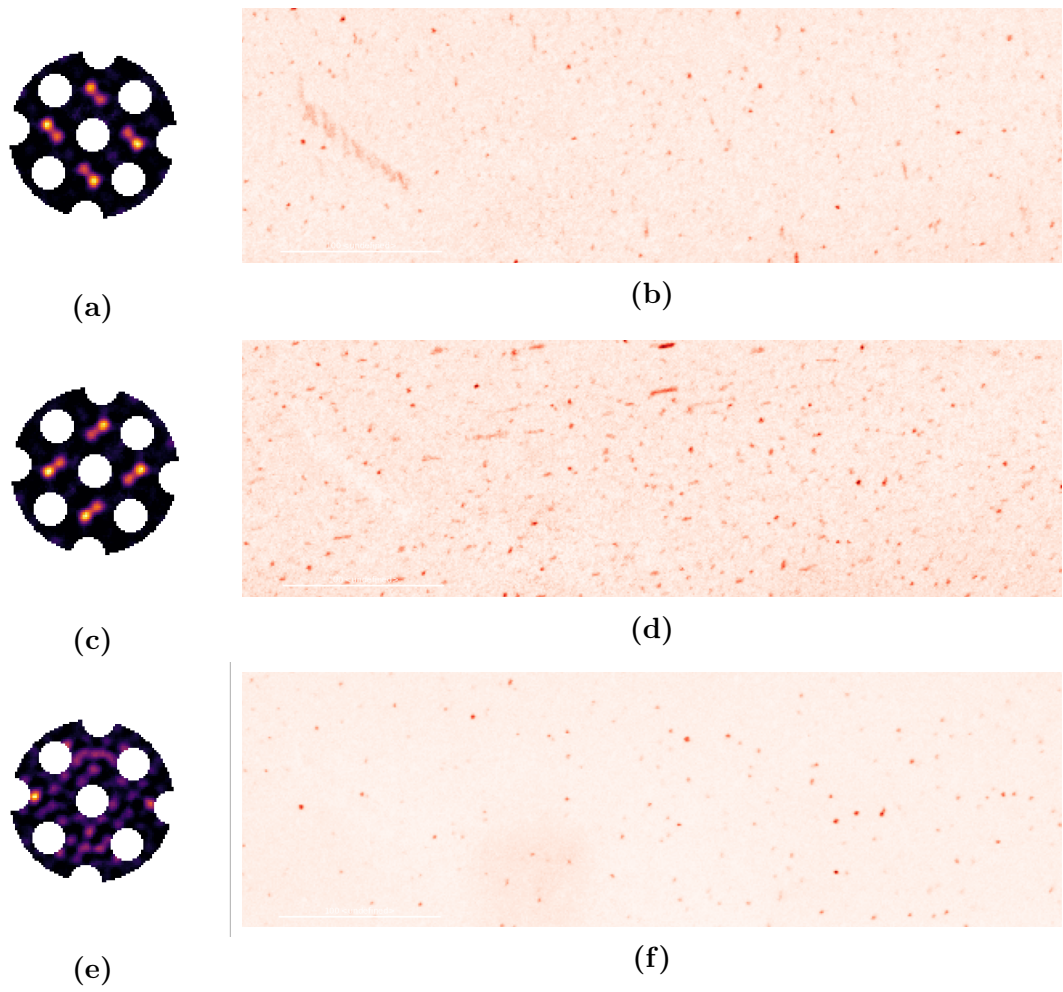
Figure C.3: (a) and (c) β'' in-plane, (e) β'

C3 scan
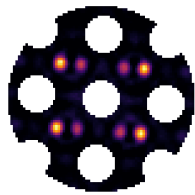
(a)

(b)

(c)

(d)

(e)

(f)
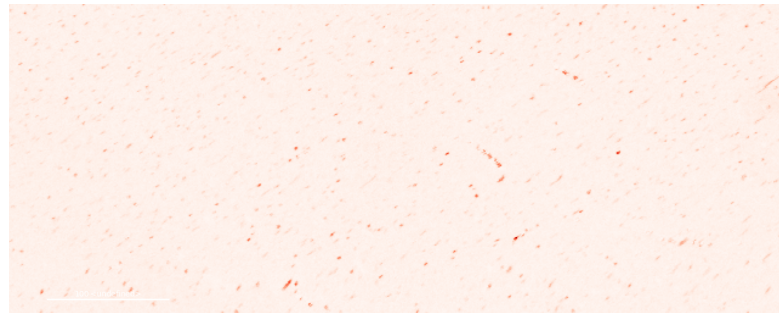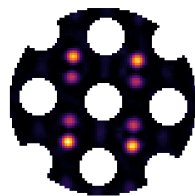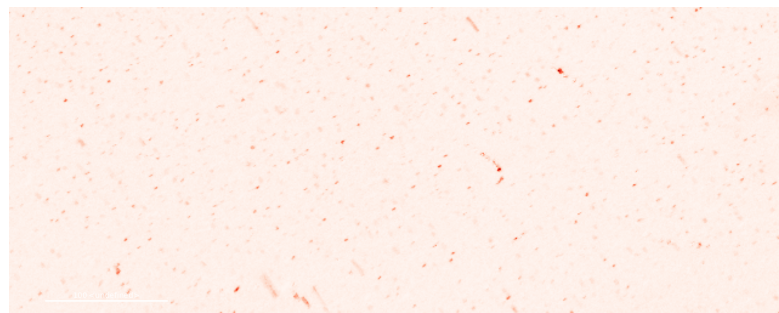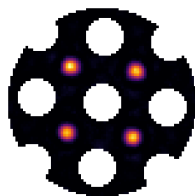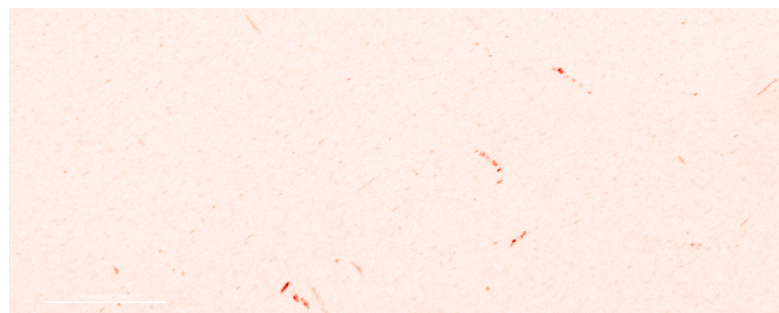
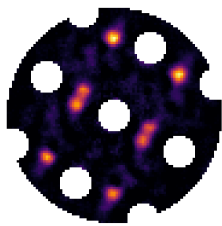**Figure C.4:** (a)(c) β'', (e) Cu
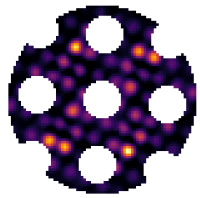
(a)

(b)

(c)

(d)

(e)

(f)

(g)

(h)
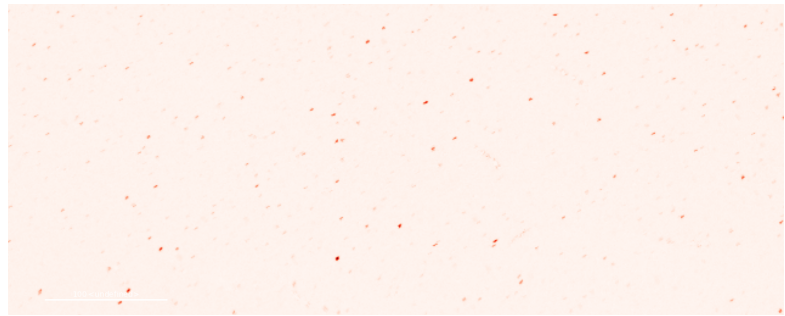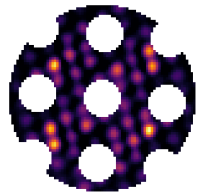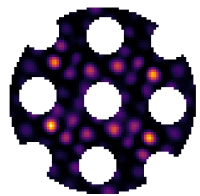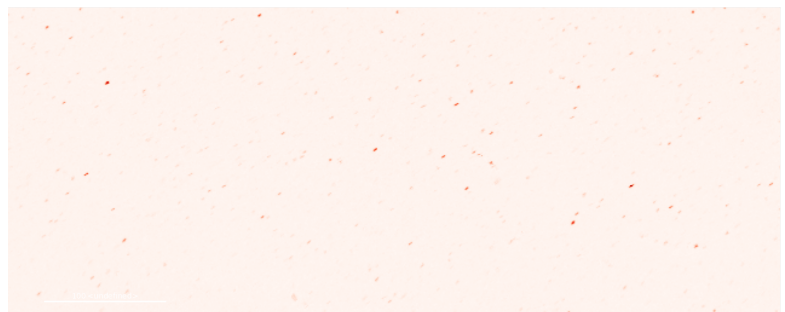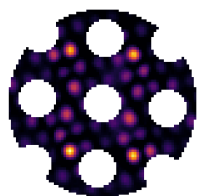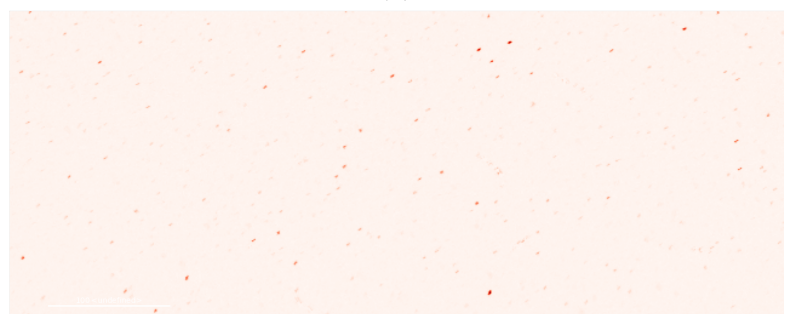
Figure C.5: β''
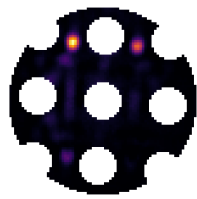
(a)

(b)
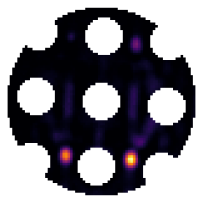
(c)

(d)
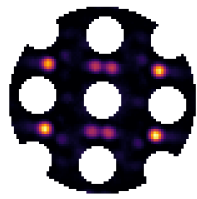
(e)

(f)

Figure C.6: L phase, (a) and (c) are over-decomposed factors from the same diffraction pattern
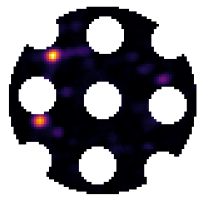
(a)

(b)
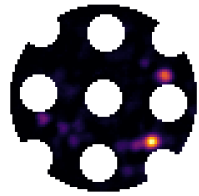
(c)
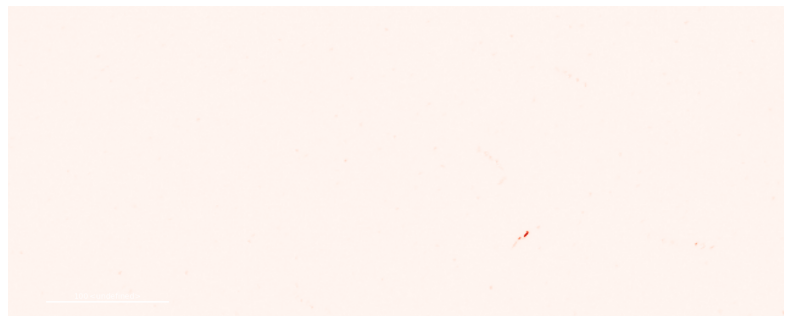
(d)
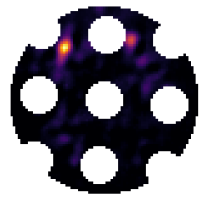
(e)

(f)
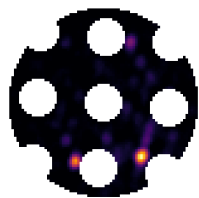
(g)
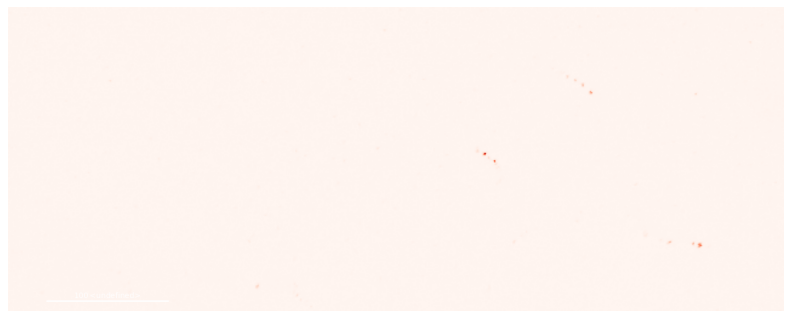
(h)

Figure C.7: Q', over-decomposed.

D4 scan
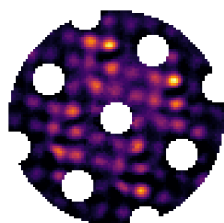
(a)

(b)

(c)

(d)

(e)

(f)

(g)

(h)

Figure C.8: β''

(a)

(b)

(c)

(d)

(e)

(f)

(g)

(h)
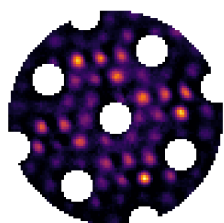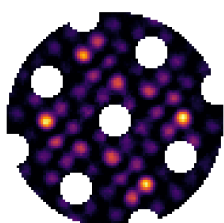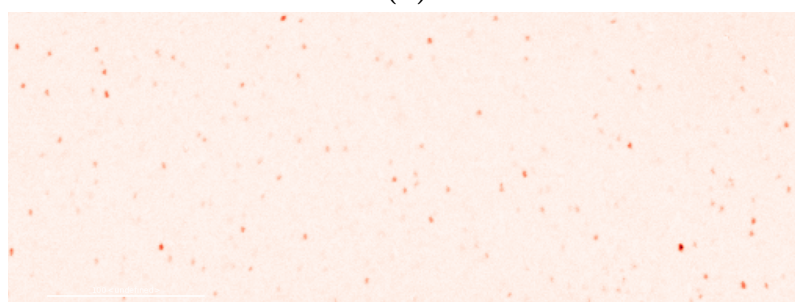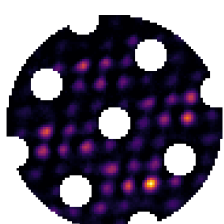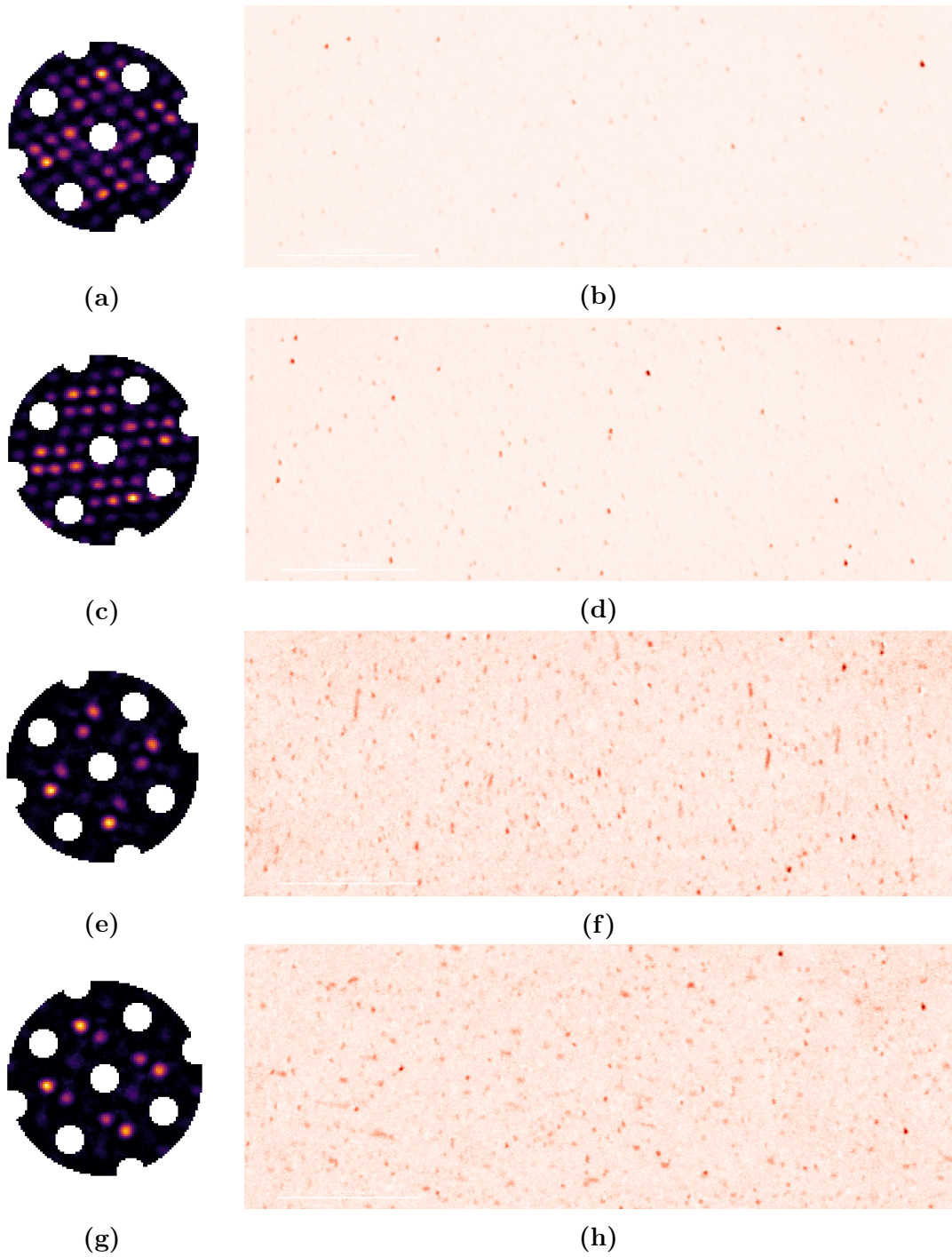
Figure C.9: (a)(c) β'', (e)(g) β'' in-plane

(a)

(b)

(c)
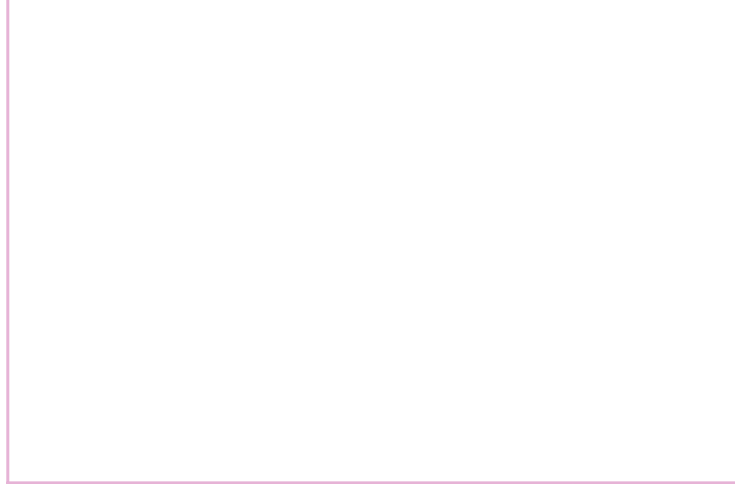

(d)

(e)

(f)

Figure C.10: (a)(c) L, (e) Cu